Modeling of sound propagation in forests using the transmission line matrix method : study of multiple scattering and ground effects related to forests

Pierre Chobeau

Modeling of sound propagation in forests using the transmission line matrix method

Study of multiple scattering and ground effects related to forests

Pierre Chobeau

Thèse de doctorat en acoustique
Ifsttar - Cerema, France
Université du Maine, Le Mans, France, 2014

Université du Maine, Académie de Nantes
Doctoral School of Science Engineering, Geoscience and Architecture

Doctoral Thesis in Acoustics

MODELING OF SOUND PROPAGATION IN FORESTS USING THE TRANSMISSION LINE MATRIX METHOD

Study of multiple scattering and ground effects related to forests

Pierre Chobeau

Defended on 6th November 2014 in front of the examining committee:

Ulf KRISTIANSEN	Professor (NTNU Trondheim)	Reviewer
Philippe JEAN	Dr-Ing. (CSTB Grenoble)	Reviewer
Kurt HEUTSCHI	Senior Scientist (ETH Zürich)	Examiner
Vincent PAGNEUX	Directeur de Recherche CNRS (Université du Maine)	Examiner
Judicaël PICAUT	Directeur de Recherche (Ifsttar Nantes)	Thesis director
David ECOTIÈRE	Dr-Ing. des Travaux Publics de l'État (Cerema)	Advisor
Guillaume DUTILLEUX	Dr-Ing. des Travaux Publics de l'État (Cerema)	Advisor
Sylvain CHEINET	Chercheur (ISL)	Guest
Fabrice JUNKER	Ingénieur Chercheur Expert (EDF R&D)	Guest

Résumé

Prévoir l'impact d'une forêt sur les niveaux acoustiques reste actuellement un enjeu majeur pour la communauté de l'acoustique environnementale. Les méthodes d'ingénierie en place, notamment utilisées pour la cartographie acoustique, ne permettent pas actuellement de prévoir les niveaux propagés au travers d'espaces végétalisés tels qu'une forêt. Ces espaces sont pourtant souvent garants d'une certaine biodiversité, et ils peuvent également prétendre au statut de zone calme telle que défini par la directive européenne 2002/49/EC.

Les trois principaux phénomènes acoustiques propres au milieu forestier sont l'absorption due à la présence d'un sol multi-couche typique en forêt (litière et humus) ; la diffusion multiple due à la présence d'obstacles tels que les troncs, branches ou feuilles ; et les effets micro-météorologiques rattachés aux variations des gradients de vitesse de vent et de température en présence de forêt. Parmi les méthodes numériques de référence, la méthode des lignes de transmission (TLM) est une méthode temporelle déjà éprouvée dans le cadre de simulations de propagation acoustique sur de grandes distances. De plus, le principe de la méthode TLM pour l'étude de la propagation acoustique en présence de forêt semble particulièrement adapté, notamment pour la modélisation de phénomènes acoustiques tels que la diffusion.

La première nécessité pour l'adaptation de la méthode TLM aux simulations acoustiques sur de grandes distances est la définition de couches absorbantes permettant de tronquer efficacement le domaine d'étude sans introduire de réflexions parasites. Les couches absorbantes existantes sont basées sur une approche empirique visant à atténuer progressivement l'onde sortante entre chaque nud du maillage TLM jusqu'à extinction de l'onde. Cette solution reste numériquement coûteuse car elle requiert des épaisseurs de couche significatives. À partir de l'étude théorique des couches absorbantes parfaitement adaptées (PML), deux formulations approchées ont été proposées. La formulation retenue est rigoureusement équivalente à l'équation de propagation des ondes amorties, et se traduit dans la méthode TLM par l'introduction et l'optimisation d'un terme de dissipation. Il est montré qu'après optimisation la formulation proposée est plus performante que la meilleure des solutions actuelles sur une large gamme d'angles d'incidences.

L'étape suivante consiste à vérifier la capacité de la méthode TLM à modéliser les phénomènes de diffusion. L'observation de la diffusion simple par un obstacle circulaire en 2D, puis par un cylindre placé perpendiculairement à un sol impédant (3D) montre que la méthode TLM est en bon accord à la fois avec les solutions analytiques et des mesures réalisées sur maquette. La diffusion multiple est également validée en 2D par comparaison avec les solutions analytiques, puis par comparaison avec des mesures effectuées sur maquette pour le cas 3D. Dans l'ensemble les résultats confirment la capacité de la méthode TLM à modéliser les phénomènes de diffusion. Par ailleurs, l'une des originalités introduite dans cette thèse réside dans le placement des éléments diffuseurs, à partir de lois de distribution aléatoire et de Gibbs, permettant ainsi de définir des répartitions proches de celles rencontrées en forêt.

Dans un premier temps, l'étude paramétrique de la propagation d'ondes acoustiques à travers plusieurs distributions de cylindres a permis d'étudier l'influence de la densité des arbres, de la longueur de la forêt, de la répartition des cylindres et de

l'absorption du sol sur la propagation acoustique. Il est ainsi montré que les répartitions aléatoire et en grappe (agrégats de diffuseur sur longueur déterminée) donnent des atténuations globales supérieures (2.5 à 3.0 dB supplémentaires) à celles obtenues avec des répartitions périodiques. Comme attendu, une augmentation de la densité ou de la longueur de la forêt tend à augmenter l'atténuation globale. Par ailleurs, l'absorption due à l'effet de sol (introduite à partir des coefficients de réflexion) permet d'obtenir un gain d'atténuation d'environ 2 dB. Une étude de sensibilité des paramètres étudiés permettrait à l'avenir d'identifier clairement les paramètres morphologiques d'une forêt déterminants pour l'atténuation acoustique.

Remerciements

Je remercie Judicaël Picaut d'avoir accepté de diriger cette thèse. Merci pour ces échanges, ces conseils et l'ensemble des remarques constructives apportées tout au long de ce travail. Je remercie Gwenaël Guillaume de m'avoir inculqué quelques précieuses notions de calcul numérique, ainsi que l'ensemble de l'équipe du LAE pour m'avoir aidé à mener à bien cette campagne de mesure. Merci à David Ecotière et Guillaume Dutilleux de m'avoir accueilli au Cerema et fourni le matériel utile à la réalisation technique de ce travail. Je remercie Fabrice Junker et Sylvain Cheinet d'avoir participé au suivi de ce travail.

Je souhaite particulièrement remercier Cédric Foy pour son écoute et son soutien constant tout au long de ces trois années passées au laboratoire de Strasbourg. Je remercie également Charlotte Curé pour son dynamisme et ces discussions avisées. Merci à Christophe, Mélodie et Bertrand pour ces pauses déjeuner animées.

Pour leur soutien sans faille durant ces années d'études, je remercie mes parents et l'ensemble de ma famille. Merci à mes colocataires de la place d'Austerlitz d'avoir supporté mes sarcasmes et d'avoir su adoucir ces longues soirées d'hiver avec la généreuse cuisine alsacienne. Enfin, merci à toi Clara, pour ta patience, ton soutien sans limite et tes encouragements quotidiens.

Contents

List of Symbols

α_∞	tortuosity
δl	spatial step in a regular TLM network
δt	time step
δx	spatial step following x-axis
δy	spatial step following y-axis
η	TLM heterogeneity term
$\jmath$	imaginary unit
λ	signal wavelength
$\mathrm{AML}_{\eta,\zeta}$	Absorbing Matched Layer relative to the TLM heterogeneity and dissipation terms
AML_{ζ}	Absorbing Matched Layer relative to the TLM dissipation term
Ω	porosity
ω	angular frequency
ρ_0	medium density
σ	PML attenuation factor
σ_g	mean flow resistivity
σ_x	PML attenuation factor following x-axis
σ_y	PML attenuation factor following y-axis
σ_{max}	maximum value of the PML attenuation factor
θ	angle of incidence
ζ	TLM dissipation term

${}_t\mathbf{S}$	scattered pulses
${}_t\mathbf{D}$	scattering matrix
${}_t\mathbf{I}$	incident pulses
${}_tp_{(i,j)}$	discretized acoustic pressure
a	radius of the scatterers
c	celerity between two consecutive TLM nodes
c_0	adiabatic sound celerity
c_{eff}	effective celerity
c_{TLM}	TLM celerity over the network
d	distance between the AML interface and a point inside the test area
d_N	distance between the AML interface and a point inside the AML
e_{AL}	total absorbing layer thickness
f	frequency
$F_{(i,j)}$	attenuation factor for the matched connexion laws
i, j	discrete TLM coordinates
k	wave number
L_{scat}	scattered pressure level
n, m	number of the main TLM branches
n_d	dimension of the TLM calculation
$N_{\lambda_{\text{AL}}}$	equivalent absorbing layer thickness in wavelength unit
p_{ff}	free-field acoustic pressure
$p_{(x,y,t)}$	physical acoustic pressure
p_i	incident pressure
p_s	scattered pressure
R	reflexion coefficient
S_{scat}	surface of the scatterers area
v	particle velocity
v_x	particle velocity: vectorial component following x-axis

v_y	particle velocity: vectorial component following y-axis
W	number of scatterers per square meter
Z	characteristic impedance of a TLM branch
Z_0	characteristic impedance
Z_{cyl}	impedance of the cylinder
Z_g	impedance of the ground

.

GENERAL INTRODUCTION

1 Context

Noise pollution is a major environmental problem within the European Union (EU). The World Health Organization [1,2] estimates that about 40% of the population in EU countries are exposed to road traffic noise at levels exceeding $55\ \mathrm{dB(A)}$, and 20% are exposed to levels exceeding $65\ \mathrm{dB(A)}$ during daytime. The social costs of traffic noise have been estimated to 0.4 % of total GDP[1]. The French National Institute of Statistics and Economic Studies (INSEE) [3] has shown that 54% of the French households living in a city are annoyed by noise at home. Among the noise sources that impact the households, transportation noise is in the first position.

It is now well known that noise exposure has an impact on public health. Among the physical health effects, noise exposure can cause annoyance, sleep disturbance, cognitive impairment, physiological stress reactions, endocrine imbalance, and cardiovascular disorders [4,5].

This demonstrates that protection of the population from noise annoyance remains a major challenge. In this view, noise problems can either be treated at the source or at the receiving position. In the case of transportation noise, a first option can consist in reducing the dominant source of noise. The rolling noise can be approached through the study of tyre/road or wheel/rail contacts [6,7]. The second option is to treat the propagation medium, *i.e.* to protect the receiver by altering the noise propagation path. In this view, noise barriers [8] are widely used to screen residential areas from high levels of traffic noise. Nowadays, with the growing interest for sustainable development, acoustic protections should be investigated using the most ecological and natural existing material. In this sense, the following paragraph gives an overview of some vegetation acoustic properties.

2 Noise mitigation and vegetation

Historically, among the first works that relate noise attenuation to vegetation, Aylor [9,10] proposed two studies on noise transmission through corn, hemlock and

[1]The Gross Domestic Product (GDP) is the market value of all officially recognized final goods and services produced within a country in a year.

reed fields. It is shown that both the ground and the stems of the vegetation have a significant impact on noise transmission.

More recently, interest for the vegetation ability to attenuate noise can be illustrated through the work proposed by Horoshenkov *et al.* [11]. The leaf area density and orientation, and the properties of the soil substratum are considered to be the determinant parameters for the prediction of the acoustic absorption of low growing plants. At the same time, Ding *et al.* [12] studied the influence of loose leaves on a porous substrate, as found on vegetative walls or green roofs, and proposed a theoretical model that predicts the attenuation coefficient. The measurements performed using impedance tube show that an increase of the absorption coefficient is expected at middle frequency (500-2000 Hz).

As recalled by Ding *et al.* [12], increasing the wall absorption in a city street results in a noticeable noise reduction in an adjacent city canyon. This has been demonstrated by Van Renterghem *et al.* [13] using finite-difference time-domain (FDTD) simulations. Similarly, the façade absorption is shown to give significant noise reduction in the work presented by Hornikx and Forssén [14]. Therefore, in urban areas, solutions such as green roof [15–17] or green façade [18] have been investigated as promising protections from noise for the residents.

To moderate the impact of vegetation on noise propagation, an experimental study on forest edges performed by Van Renterghem *et al.* [19] shows that relatively low noise reduction for light vehicle is expected from hedges. Although measured insertion loss of hedges is estimated to be only about 1.5 dBA, it is noticeable that the presence of hedges improves the ground effect at low frequency and leads to significant noise absorption due to the presence of foliage at high frequency.

Considering classical noise protection such as concrete noise barriers, they can either be associated to earth berms [20] or vegetation hedges [21] in order to improve their performances. Although classical noise barrier materials such as concrete are common, the use of natural protection from vegetation remains an important topic.

Each of these works shows that vegetation can be seen as an additional solution for the attenuation of noise levels. In order to accurately assess such solutions, *in situ* measurements can be performed and corroborated using numerical prediction models as proposed in the European project Hosanna [11] and the French National Research Agency (ANR) project VegDUD [22]. The present thesis follow on from these projects using an alternative time domain numerical method: the Transmission-Line Matrix (TLM) method for the study of sound propagation in forests. However, as shown in the following sections, the potential propensity of vegetation for noise mitigation is not the only motivation of this work.

3 Forested areas in France and their interest for acoustics

3.1 Development and importance of forests in France

An aspect of the economic development is the movement of population from the countryside to cities. In France, urbanization took the form of similar growth rates

across cities of different sizes [23]. As a consequence, agricultural landscape, forests, and natural landscapes represent 87% of the French territory. In addition to urbanization, the decrease of pasture lands (-7% between 1992 and 2002) contributed to the increase in forested areas (+470000 hectares between 1992 and 2002) [24]. Today, forest in itself covers about 28% of the country total area [25].

3.2 Forested areas and quiet areas

The Environmental Noise Directive (2002/49/EC) [26] suggests that the competent authorities of each European country should take actions on the preservation of quiet areas in agglomerations and in open country. Although the definition of quiet area remains under study as pointed out by Delaitre *et al.* [27], forests appear to be relevant places where to define a quiet area. In addition to noise mitigation, the natural surrounding that can be constituted by a forest can be seen as a health benefit typical of quiet areas, as defined in the the European Environmental Agency [28] technical report.

3.3 Forested areas and biodiversity

Despite acoustic constraints of forest habitats, many species living in forests rely on sounds to communicate as mentioned, for instance, in chapter 4 of the book written by Catchpole and Slater [29]. In such a constraining acoustic environment, the efficiency of an acoustic communication system results from an information coding/decoding process particularly well tuned to the acoustic properties of this environment. Thus, modeling the sound propagation inside forest would give insight on how it impacts the available information to receivers after sound transmission through the habitat. Another important aspect, is the assessment and the control of anthropogenic noise exposure for animals living in forest edges (*e.g.* small forest strip) as reviewed by Barber *et al.* [30]. An accurate prediction of noise levels inside forests could provide useful informations for an accurate quantification of noise exposure for forest species.

Noise mitigation, protection of the existing quiet areas and study of the biodiversity constitute three axes of interest that motivate the investigation of sound propagation in forests.

4 Prediction methods and forest

Engineering methods used for noise mapping often ignore the presence of forests in their calculations. This can lead to inaccurate noise level predictions in the vicinity of forested areas. In order to overcome this lack of accuracy, the acoustical phenomena specific to forest can be numerically studied in the details using reference numerical methods. In the long term, the developments of reference methods would give rise to simplified formulations that can be used for the improvement of the engineering method predictions.

Considering the engineering methods, the international standard calculation method ISO 9613-2 [31] only takes into account an attenuation caused by the foliage as a function of the distance traveled through the foliage. The Nord 2000 [32] method gives a correction for scattering effect caused by obstacles and a mean flow resistivity for the forest ground equal to 31.5 kNsm^{-4}. The Harmonoise [33] method relies on a similar approach. The Nord 2000 model was compared to experimental data by Tarrero *et al.* [34]. It was shown that the ground dip is relatively well predicted, whereas at higher frequencies, where scattering phenomena are important, the model fails. Therefore, engineering methods still need some improvements for more accurate prediction of the sound levels in presence of forests.

Looking at the reference numerical methods, one of the first investigation has been performed by Huisman [35, 36]. He used a ray tracing method on a simplified forest showing that, in downwind condition, the downward refraction is increased compared to propagation above pasture land. The parabolic equation model has also been adapted for the simulation of sound propagation in forests. Barrière [37], White and Swearingen [38, 39] and Tunick [40] used the Green function parabolic equation (GFPE) with the effective celerity approach to take into account the specific meteorological conditions of forests. Johansson [41] used the Crank-Nicholson parabolic equation (CNPE). In addition to the classical ray tracing or frequency-domain methods, time-domain methods can also be an interesting way for the study of sound propagation in forests. In this sense, the FDTD method used by Heimann [42] shows that multiple scattering and downwind propagation cases can be taken into account for sound propagation in forests using time-domain methods.

This short review on the prediction methods shows that the forest is usually simplified for acoustic simulations. Although frequency-domain methods have been widely used, time-domain methods have received relatively moderate interest. During the last decades, the increase in computational resources promote the development of time domain methods that could present significant advantages for the simulation of sound propagation. In this sense, the Transmission Line Matrix (TLM) method can be seen as an interesting time domain reference method for the simulation of the acoustical phenomena related to sound propagation in forests. This method is adapted to the simulation of wave propagation in heterogeneous media with complex geometries. Thus, time-dependent phenomena, such as the superposition of incident and scattered time signals from multiple scattering caused by tree trunks inside a forest, can be modeled using the TLM method. This method has already been extended to outdoor sound propagation by several authors [43–46]. Its extension to sound propagation in forests is seen as an interesting feature to enlarge the scope of the method.

5 Thesis organization

As suggested before, protection of the population from noise (*i.e.* the forest seen as a noise barrier), preservation of quiet areas and biodiversity constitutes the three main motivations for the study of sound propagation in forests. During the last

years, the TLM method is the reference method that has been chosen and developed at Ifsttar[2] for the study of outdoor sound propagation. One of this thesis main purpose consist in developing the method for taking into account the acoustic phenomena related to the propagation in forests. In the short term, *i.e.* in the context of this thesis, the TLM method still needs to be improved for the study of long range sound propagation. The derivation of theory-based efficient absorbing layers adapted to the TLM method constitutes in itself a first important step. Then, the next step towards the simulation of sound propagation through forests consists in studying the ability of the TLM to model the scattering by trees of acoustic waves above an impedance ground. In the long term, the main challenge is the use of the TLM method as a reference prediction approach for the development of simplified formulations adapted to engineering methods.

To achieve the above-cited objectives, this thesis is divided into four chapters. Chapter 1 is a review on the influence of forests on sound propagation. This introduction to the acoustic properties of forest shows how the acoustic wave is impacted by the forest medium. Furthermore, this review presents how the forest has been considered in previous acoustic studies. The three main acoustic phenomena occurring in forests (*i.e.* effects from forest ground, multiple scattering from tree trunks and meteorological fluctuations) are detailed through the review of the previous acoustic publications.

Although the TLM method has been recently developed for the simulation of outdoor sound propagation [47, 48], no rigorous absorbing layer has been proposed yet for the TLM method in acoustics. Absorbing layers represent a major need in the case of outdoor sound propagation, where large propagation domains usually imply significant computational cost. The reduction of the computation domain (*i.e.* the reduction of the computational cost) using efficient absorbing layers is seen here as the first need for the method. In this view, chapter 2 presents the derivation of absorbing layer formulations adapted to the TLM method. These formulations are based on the adaptation of the perfectly matched layer theory to the TLM method.

Back to sound propagation in forests, chapter 3 deals with the ability of the TLM method to take into account scattering phenomena. The tree trunks are approximated as cylinders placed normal to an impedance ground. Scattering and ground effects are numerically, analytically and experimentally studied.

This validation of the TLM method leads to a more extensive parametric study presented in chapter 4, where the relative importance of forest ground effects compared to multiple scattering is studied using realistic forest parameters for the placement of the scatterers. This gives the main trends for the prediction of the impact of a simplified forest on sound propagation.

Lastly, concluding remarks based on the four chapters results are given. Furthermore, the conclusion provides the perspectives for future works in order to give some general guidelines to deal with sound propagation in the presence of forests using the TLM method.

[2]French institut of science and technology for transport, development and networks

Chapter 1

FOREST AND SOUND PROPAGATION

1.1 Introduction

In the literature related to outdoor sound propagation, many articles deal with the propagation inside or in the vicinity of forested areas. This section aims at referencing these papers to give an overview of the specificities related to the forest environment, which directly impact acoustic waves propagation. Moreover, this state of the art would give the material for better understanding of the complex "forest effects" on acoustic propagation. In this sense, the content of this first chapter presents some general background that would provide useful guidance for future investigations on sound propagation in forests.

The physical phenomena related to sound propagation in forests can be divided into three main branches such as ground effects, sound scattering and meteorological effects. Each of these aspects constitutes an area of research in itself, and has been widely, theoretically and/or experimentally investigated in the past. The structure of this chapter follows the evolution of the theories and experiments for each aspect related to sound propagation in forests.

To depict the state of the art on sound propagation inside and around forested areas, this chapter is organized as follows. Section 1.2 deals with the ground effect related to specific forest floors. The impedance models developed for the characterization of sound propagation above forest floor are detailed. Experimental method and data are reminded to give an overview of the floor properties. Section 1.3 treats the scattering phenomena related to the presence of trunks, branches and foliages. Both analytical models and measurement methods are recalled in their general principle. Lastly, section 1.4 presents the meteorological effects that occur when acoustic waves travel through or around forested areas.

1.2 Ground effects inside forest

Considering a source and a receiver both located above the ground surface, ground effects result of the interference between the direct wave (source to receiver) and

the wave reflected (source - ground - receiver) from the ground [49]. This leads to both constructive and destructive interferences at the receiver location. The inherent characteristics of a ground, such as a forest floor, directly influence this phenomenon.

1.2.1 Introduction to the forest floor

From a general point of view, many forest floors are made of layer superpositions whose properties are related to the state of the forest in itself. Among these layers, the two upper layers are made of organic deposit on top, supported by a layer of mineral matter. The organic layer can be subdivided into two sub-layers: the litter layer made of dead vegetative plant parts such as leaves, and the humus resulting from the decomposition of the litter matter. Each layer characteristic influences the wave propagation above such floors.

1.2.2 Impedance models

Forest floors have been extensively studied by Talaske [50]. In this work, it is shown that for a red pine and a deciduous forest, the two sub-layers can be merged and the complete floor can be approximated as a porous layer supported by a semi-infinite porous base. This gives the following impedance structural model written as:

$$Z(d) = Z_1 \frac{Z_2 - iZ_1 \tan(k_1 e)}{Z_1 - iZ_2 \tan(k_1 e)}, \tag{1.1}$$

where Z_1 and Z_2 are the characteristic impedance of, respectively, the upper porous layer of thickness e and the lower semi-infinite porous layer and where k_1 is the wave number in the upper layer.

Attenborough [51] proposed a four-parameter model that is combined to the original results of Talaske. The four parameters are the porosity Ω, the tortuosity α_∞, the flow resistivity σ_g and the pore shape factor s_p. Under the assumption of high flow resistivity, three parameters are identified as significant: the effective flow resistivity $\sigma_e = s_p^2 \sigma_g / \Omega$, the porosity and the tortuosity [52]. This impedance model is denominated by H3A (*Homogeneous three-parameter Approximation*), where the characteristic impedance Z_c is written as:

$$Z_c = \left(\frac{4\alpha_\infty}{3\Omega} + \frac{4\jmath\Omega^2\sigma_e}{\omega\rho_0} \right) \frac{1}{k_1}, \tag{1.2}$$

and the wave number is

$$k_1 = \sqrt{\gamma \left(b\alpha_\infty + \frac{4\jmath\Omega^2\sigma_e}{\omega\rho_0} \right)}, \tag{1.3}$$

where ω is the angular frequency, γ is the ratio of specific heats for air, ρ_0 the air density and $b = \frac{4}{3} - [(\gamma - 1)/\gamma] N_{pr}$ where N_{pr} is the Prandtl number. Under the assumption of homogeneous soil and high flow resistivity at low frequency, the H3A model can be reduced to

$$Z_c = \frac{k_1}{\gamma\Omega} = \sqrt{\frac{\sigma_e}{\pi\gamma\rho_0 f}}(1 + \jmath), \tag{1.4}$$

which is named as the H1A model. Under the assumption that the upper layer is thin enough to write $|k_1 d| \rightarrow 0$ and the characteristic impedance $|Z_1|$ is relatively small compared to $|Z_2|$, *i.e.* $|Z_1/Z_2| \ll 1$, the characteristic impedance Z_1 can be written as $Z_1 = Z_c$. This gives rise to the Attenborough's hard-backed layer impedance two-parameter model (2PA):

$$Z(d) \simeq Z_c \left(1 + \frac{\jmath}{2k_1 e}\right). \tag{1.5}$$

These models are used in [39, 51–53] for the prediction of sound propagation above forest floors. Tolerable agreements are found between measurements and Attenbourough's four-parameter model in [51]. Moreover, it has been noticed that the structural hard-backed model (Eq. (1.5)) can be more suitable for the red pine forest than the Talaske's structural porous model (Eq. (1.1)).

The phenomenological model from Zwicker and Kosten is used for forest floors in [54]. It can be written as [55]:

$$Z(\omega) = Z_\infty \sqrt{\frac{1 - \jmath\omega\tau}{-\jmath\omega\tau}} \tag{1.6}$$

where the time constant τ is given by

$$\tau = \frac{\rho_0 \gamma \alpha_\infty^2}{\sigma_g \Omega}, \tag{1.7}$$

where Z_∞ corresponds to the impedance when $\omega\tau$ tends to infinity,

$$Z_\infty = \frac{\rho c_0 \alpha_\infty}{\Omega} \tag{1.8}$$

with c_0 the sound speed in the air.

Attenborough *et al.* [54] compared slit-pore, Delany and Bazley, Zwicker and Kosten, as well as Taraldsen models to measurements. Among these models, Zwicker and Kosten (semi-infinite) and slit-pore models present the lowest fitting errors for the two tested forests: a pine forest and a beech forest. This shows that, in particular cases, a semi-infinite model can be used as a correct approximation. In this case, characteristic impedance can be used directly to predict the influence of forest floor on the acoustic wave propagation.

1.2.3 Estimation of the ground impedance parameters

In order to implement the impedance model, the corresponding parameters have to be assessed. Heisler *et al.* [56] carried out *in situ* measurements on forest floors using a standing wave tube. It is stated that the layer depth is difficult to assess with accuracy, which would impact the impedance prediction. Attenborough [51] used the results of these measurements to determine the values of each parameter. In the framework of the engineering method Nord2000, Tarero *et al.* [34] carried out flow resistivity measurements for pine, poplar and oak forests. It is interesting to note that the results show a global increase of the flow resistivity during winter. It is recalled that large spatial fluctuations are observed for a given forest that would significantly impact the accuracy of the flow resistivity prediction.

1.2.4 Insertion loss measurements

Embleton [57] carried out measurements in four different forest edges: cedar, pine, spruce and deciduous wood. It is shown that, at low frequency, the attenuation present an "S" shape, which is characteristic of the forest type. However, because the measurements have been carried out in third octave band, it seems difficult to accurately extract the ground properties from this study.

Kragh [58] realized several measurements on seven forest edges and compared them to measurements above meadow grounds. It has been observed that the ground dip obtained with the forests edges are overall shifted to lower frequencies.

Martens [59] performed measurements on the litter layer. He compared the results obtained with the litter to those where the litter was removed. Over five comparisons, only two results show that the litter layer gives rise to significant sound absorption at low frequency. However, these results are counterbalanced by Talaske [50] who stated that the presence of a highly porous organic layer that is rigidly backed by a mineral layer significantly impacts the acoustic properties of the ground.

1.2.5 Discussion on the ground effect related to forest floors

Among the impedance models used for the calculation of the characteristic impedance, H3A, Zwicker and Kosten (phenomenological) and the slit-pore models [51,54] show interesting results for the characterization of forest floors impedance. Depending on the type of forest floor, the characteristic impedance can be used directly assuming semi-infinite layer. However, two structural models such as the double porous layers proposed by Talaske [50] and the hard-backed layer used by Attenborough [51] present interesting results for multi-layered forest floors. The comparison and estimation of forest ground parameters have been performed using measurement data [34, 51, 56]. In addition, several experimental analyses showed the influence of forest floor types on the ground dip [50, 57–59].

In a first approach, the Zwicker and Kosten (semi-infinite) model would be an interesting choice for the simulation of forest floors using the TLM method. This model has already been adapted to time domain and more especially to the TLM method [60].

1.3 Scattering of acoustic waves inside forests

1.3.1 Introduction

From a macroscopic point of view, forests can be seen as a medium full of "macro"-heterogeneities constituted by obstacles such as leaves, twigs, branches or trunks. Acoustic waves propagating inside such a medium interact with the obstacles. This can give rise to the acoustic phenomenon named scattering for a single interaction or multiple-scattering when the acoustic waves interact with more than one obstacle. Multiple scattering in forests is mostly related to the presence of tree-trunks,

branches and leaves. The acoustic wave interacting with such obstacles is reflected in specific directions and/or dissipated through various absorption mechanisms.

1.3.2 Single scattering from an isolated tree-trunk

The interaction of an acoustic wave with a single obstacle induces the reflection of the incident wave in specific directions. This constitutes the scattered field, which can be represented by its directivity pattern. The characteristics of the scattered field (amplitude, frequency) depend on the properties of the incident wave and of the scatterer. The incident wave can be described by its frequency components and magnitude, and the scatterer is characterized by its apparent diameter, *i.e.* the largest dimension of the obstacles seen by the acoustic wave.

Single scattering can be encountered in sparsely planted forests where the tree trunk can be seen as an isolated obstacle. In this case, the isolated tree can be approximated by a cylinder planted normal to an impedance forest ground. Analytical solutions are found in the literature to describe the scattering by a circular two-dimensional scatterer (the tree-trunk) [61]. As an extension, a semi-analytic solution is proposed by Swearingen *et al.* [62] for the calculation of scattering from an impedance cylinder placed normal to an impedance ground. In this semi-analytic model, the scattering effect caused by a single cylinder is coupled to the ground effect. The ground effect part is based on the image integral proposed by Di and Gilbert [63]. The scattered part is based on the solution derived by Li and Ueda in [64]. The six components that constitute the full pressure field of this model can be split into two groups: (1) the three ground components, which correspond to the direct path, the ray reflected before or after the cylinder, and the image-integral that represents the complex reflection and the ground wave; (2) the three scattering components, which are the direct scattered, the reflected scattered or scattered reflected, and the image-integral. The full field is given by the summation of all components after numerical solving of the integrations. Both analytical solutions [61, 62] are detailed in the chapter 3 of this document, and are used as references for the characterization of single scattering.

Reethof *et al.* [65] performed impedance tube measurements on several samples of tree barks in order to determine the tree trunk absorption coefficients. It is shown that the absorption coefficient did not exceed 0.08 in the frequency range 100 Hz to 1000 Hz.

1.3.3 Multiple scattering

1.3.3.1 Multiple scattering theories

Generally speaking, forests can be seen as an arrangement of scatterers, which are spatially concentrated inside an area. The incident wave is thus supposed to interact with several obstacles, which gives rise to multiple scattering. The total acoustical field inside an infinite forest results in the superposition of the incident and scattered fields, as depicted for example in figure 1.1 using the FDTD method. The analytical description of this phenomenon was first presented by Twersky [66, 67].

This theory calculates the average transmitted field through an area of randomly located vertical cylinders.

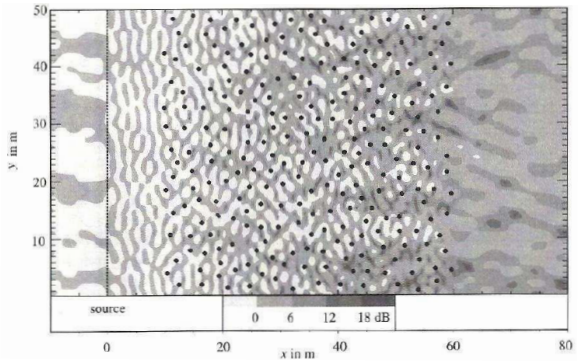

Figure 1.1: *Horizontal cross-section of the attenuation (in* dB*) by tree trunks without wind at* 1.5 m *above the ground. The position of the line source is indicated by the dashed line. The tree trunks are represented by the black dots* [42].

An extension of this theory is given by Linton *et al.* [68], where the average wave number is re-investigated in order to complete Twersky's theory, which, in some cases, can overestimate the scattering attenuation for densely planted forests.

Felbacq's theory [69] has been written for electromagnetic waves. However, this theory presents some similarities with acoustic wave formulations. Furthermore, this theory [37] can be adapted to acoustic scattering problems. Felbacq's theory relies on the quantification of the scattered field radiated by each scatterer through the calculation of scattering coefficients, which take into account the geometrical properties (radius and location) of each scatterer.

Bullen and Fricke [70] treat multiple scattering problems as a diffusion problem, where the probabilities of absorption and scattering for a given sound particle (also named phonon in [70]) are related to sound intensity. The parameter of the diffusion model such as the scattering cross-section and the absorption cross-section are estimated from both measurements on small scale models in semi-anechoic room and real trees in reverberant room. As an interesting feature, the estimation of the cross-section gives an estimation of the sound intensity inside forests.

1.3.3.2 Multiple scattering in prediction models

Twersky's theory has been used to predict the attenuation inside an array of cylinders caused by multiple scattering [71, 72] and compared to numerical data. The influence of density, trunk diameters and trunk surface impedance on the attenuations, are tolerably predicted in these works. On the other hand, Price *et al.* [53] compared Twersky's theory to measurements data, with relatively poor agreements. At higher frequency, the measurements fluctuations are not well described with the proposed model.

Swearingen and White [39] used the theory based on Linton's work [68] for the simulation of multiple scattering caused by tree trunks and the canopy. The green function parabolic equation (GFPE) model gives a good prediction of the ground dip, but shows some discrepancies above 1100 Hz compared to experimental data. Therefore, two methods have been tested for the computation of the scattering effect: (1) an attenuation coefficient is incorporated into a complex value wave number; (2) additional attenuation depending on the distance is calculated using Twersky or Linton's theory. The results given by the GFPE model show that the first method is in good agreement with Linton's theory.

Barrière [37] has linked Felbacq's and Twersky's analytical models for the study of multiple scattering in acoustics. The analogy is developed for the determination of the insertion loss caused by arrangements of scatterers that represent a periodic distribution of trees. A good agreement is found between this analogy and the boundary element method (BEM). The theory related to this work is known as the multiple scattering theory (MST), also named as the Korringa, Kohn, and Rostoker (KKR) approach. This has been used more recently, for instance, with sonic crystals made of bamboo rods in [73].

Although common forest arrangements can not be seen as sonic crystals because of the very low filling fraction, the multiple scattering phenomenon can not be mentioned without referring to wave propagation in sonic crystals. Sonic crystals can also be seen as three-dimensional periodic arrays of cylinders. Multiple scattering is the key phenomenon encountered in such a medium and gives rise to destructive interferences depending upon the filling fraction. This can lead to interesting bandgaps that attenuate a whole frequency band, which partly depends on the unit cell characteristics [73, 74].

Back to forests studies, simulations and experimentations have been carried out in order to determine the possible optimization of trees plantation for the creation of bandgaps [75–78]. In some cases, an additional dip at low frequency, which is clearly related to the periodical arrangement, is observed [75, 76]. This could be an interesting feature for traffic noise mitigation.

1.3.3.3 Scattering and noise emission induced by the foliage

The influence of the foliage on the acoustic propagation is mostly experimentally studied due to the complex geometry and arrangement of such obstacles. In several studies, the foliage is clearly seen as a low-pass filter where the cutoff frequency is estimated to be around 4000 Hz. In [79], experiments have been carried out with laser-Doppler-vibrometer in order to study the vibration of leaves. The author considers that a part of the incident energy on a leaf could be dissipated by friction. The vibration velocities measured on four species is 1 to 3 orders inferior to the air particle velocity. The author concludes that the portion of sound energy that involves the leaf vibration is not significant, and thus, most of the sound energy is simply reflected or scattered. However, for the author, even if the amount of the energy trapped by a leaf and converted to heat is relatively small, the average number of leaves per tree in a forest could be important enough to lead to a significant excess attenuation.

Yang *et al.* [80] clearly identify the foliage as responsible for sound scattering. In this experimental study on a single-isolated tree, the foliage is shown to have an influence around 4000 Hz. At this frequency most of the sound energy is scattered by the leaves.

In his work, Burns [81] takes the forest attenuation issue as an energetic problem too, and attempts to experimentally identify different dissipation processes that could take place in a pine forest. Among the possible dissipation phenomena, thermo-viscous absorption on the surface of a needle or a branch is shown to be responsible for small attenuation. The other absorption mechanisms such as flexing of needles or branches at low frequency seem to be removed from the potential attenuation factors.

Regardless of scattering phenomenon, vegetation-induced noise is another field of investigation related to the study of the acoustic influence of foliage. Fégeant [82] attempts to predict the acoustic emission from foliage as a function of the wind speed. After experimental investigation on several species, the author noticed that deciduous foliage emits sound around the frequency 4000 Hz irrespectively of the wind speed. Pine species emit at the frequency f, which corresponds to a Strouhal number equal to 0.2, $S_t = \frac{f\ D}{v}$, where D is the average diameter of the needles and v the mean flow speed. The predicted maximum pressure values along frequency corresponds to needles diameter that are used for the experimentation. More recently, Bolin [83] proposed a wind-induced vegetation noise model for the prediction from coniferous, deciduous and leafless trees. The comparison between the prediction of the model and the measurements shows a correct agreement.

1.3.3.4 Consequences of scattering

Reverberation inside forests

From an internal point of view, a forest can be seen as a room delimited by its ground, edges and canopy. In this sense, the reverberation time can be investigated assuming that the studied forest is equivalent to an enclosed volume. Few studies [41, 84–86] have been carried out on this topic, where the reverberation can be seen as a direct consequence of sound scattering inside a forest.

Huisman and Attenborough [84] studied the reverberation time inside forests to calculate the absorption coefficient used in a stochastic particles bounce model. Although no values are given for the reverberation time in itself, the main trends are extracted from the simulated decay curves. They found out that a periodic forest with relatively small trunk diameters is more inclined to present high reverberation times than forests with the same trunk locations but larger trunk diameters.

Padgham [85] showed that reverberation measurements is an interesting way for the quantification of the excess attenuation found in particular frequency bands. Moreover, its is reminded that reverberation measurements are easily carried out and can be quickly interpreted. In this work, it is noticed that for the frequency band 1000 Hz - 3000 Hz, sound levels do not decrease as fast as for lower frequencies. The wavelengths here are closely related to the tree trunks diameters and foliage.

Yang *et al.* [80] showed that the reverberation time can be used to determine the proportion of scattered sound from a single tree. In this experimental study

performed on trees of different species (oak, cherry, maple and lime), it is observed that the reverberation time is proportional to the tree crown size. Moreover, as seen before for the scattering, the leaves are identified as responsible for the increase of reverberation time at 4000 Hz.

The influence of sound scattering by a forest edge was experimentally studied by Swearingen and Swanson [87]. The waveforms resulting from an impulse source show that the primary pulse is followed by reverberation. This is identified as a consequence of sound scattering inside the forest edge.

In addition, the reverberation time in forests provided useful informations for the bio-acoustic community. Within the context of birds communication, it can be interesting to define the characteristics of the propagation medium. Marten *et al.* [86] showed for example that reverberation and thus scattering can directly influence birds communication. The same frequency band 1000 Hz - 3000 Hz as in [85] have been identified as the so-called Morton's window [88], who observed that birds have adapted their communication regarding to this specific frequency window as a result of evolution.

Sound absorption

Multiple scattering leads to sound absorption. Considering energetic approaches [70, 84, 89], absorption coefficients are often determined from the measurements and directly included in the model as an additional coefficient. In the other hand, in wave theory, the absorption is defined through the wavenumber whose imaginary part is defined to predict the wave dissipation, such as in [67, 68]. In both approaches, it is clearly stated that multiple scattering leads to an absorption of sound. This directly impacts the excess attenuation shown in several papers, such as illustrated in [9, 89, 90].

1.3.4 Discussion on sound scattering inside forests

The theory related to multiple scattering can be split into two classical approaches: wave and energetic approaches. Among the wave theory, Twersky and Linton theories are the most commonly cited. These are used as a reference to describe the multiple scattering phenomena in forests. The energetic approaches have known relatively moderate interest, but still provide interesting insight into the dissipation mechanisms. This literature review shows that multiple scattering can lead to an increase in reverberation time for specific frequency bands. This shows that the energy can be dissipated inside a forest, which gives rise to an excess attenuation related to multiple scattering.

This review confirms the necessity to take into account scattering phenomena in a prediction model. The frequency dependence of scattering and its effect on the reverberation time justify the use of a time and undulatory approach, such as the FDTD [72] or the TLM methods. Therefore, chapter 3 will focus on the ability of the TLM method to model the scattering phenomenon. Wave propagation in presence of scatterers will be studied through the comparison of the TLM method with the analytic models proposed by Swearingen and Swanson [87] and Embleton [71] for, respectively, the single and multiple scattering. Because of the measurements re-

sults on tree barks shown by Reethof *et al.* [65], in a first approach, the simulations in chapters 3 and 4 assume that the trunks are perfectly reflecting.

1.4 Meteorological effects

Sound propagation in the lower atmosphere can be strongly influenced by atmospheric conditions [91]. Firstly, the meteorological fields impacted by the presence of forests are listed. Secondly, the influence of the meteorological fluctuations on acoustic wave propagation are presented regarding forests morphology.

1.4.1 Meteorological fluctuation related to forests

Atmospheric fields such as vertical wind speed profiles, vertical temperature, and humidity profiles are modified due to the presence of forests. The leaf density, the latent heat flow, the evapotranspiration, which are relative to a given species, lead to meteorological fluctuations to a certain extent. In this sense, the forest canopy can be seen as an active thermodynamic medium. The following sections briefly summarize the corresponding meteorological aspects.

1.4.1.1 Temperature

The lower atmosphere in the presence of forests can be split into two layers separated by the canopy. During a sunny day, the upper part of the canopy accumulates the heat and protects the lower part from high temperature. In this case, in the evening, the canopy shows higher temperature than in the atmosphere, which can give rise to vertical temperature profile inversion at sunset. The vertical temperature profile in forests depends on the canopy structure, the sunshine rate and the cloud layers. Different models are found in the literature such as in [40, 92] to predict the vertical temperature profiles in presence of forests.

1.4.1.2 Wind

The presence of forests leads to the modification of the vertical wind profiles. Additional drag, canopy forces and surface fluxes influence wind speed fluctuations in the vicinity of forests. Predictions model such as in [93] study the coupling between the atmospheric layers in order to solve the surface boundary layer (inside and above the canopy) to predict the vertical wind profiles with accuracy. The leaf density is also taken into account in the steady-state and the conservation equations, for the prediction of the turbulent fluxes and mean variances of the wind speed [40,93]. Engineering models such as [94] simply take into account two parameters: roughness length and displacement height, for the prediction of vertical wind speed fluctuations.

1.4.1.3 Turbulence

The presence of a forest canopy gives rise to a turbulent flow over the forested area. This leads to wind speed and temperature fluctuations around average val-

ues. Large-eddy simulation (LES) is a mathematical model used for the numerical simulations of turbulence at very fine scale through the fluid dynamics equations. This model has been used within and above heterogeneous vegetation canopies, for example in [95]. This turbulent fluctuation can then be integrated to prediction systems such as the Advanced Regional Prediction System (ARPS) [95].

1.4.1.4 Humidity

Humidity fields in the vicinity of forests are impacted by the evapotranspiration. This phenomenon can be seen as the addition of the evaporation and the trees transpiration. This constitutes the largest component of the terrestrial hydrological cycle, and directly depends on the vegetation and the ground type [96]. Humidity fluctuation is a consequence of this phenomenon.

A detailed review on the sensitivity of wind, temperature and humidity fields inside and above the canopy to atmospheric stability and seasonal canopy changes can be found in [97].

1.4.2 Impact of the meteorological fluctuations on acoustics

The work carried out by Eyring [98] in 1946, called "Jungle acoustics", is one of the first experimental studies on sound propagation in forests. Among the observations realized in a tropical forest, it is admitted that no temperature or wind gradient influence the acoustic propagation inside the forest, *i.e.* below the canopy. However, from the literature issued during the last decades (see for example [91]), it becomes clear that meteorological conditions are of prime importance for the prediction of outdoor sound propagation. This is especially true when looking at the impact of forested areas on the meteorological conditions.

Temperature inversion caused by the canopy and the specific wind vertical profiles in presence of forests can be responsible for refraction of the acoustic energy either upward or downward. Furthermore, it is well known that the turbulent flow can cause an acoustic shadow zone due to scattering of sound energy [91]. These atmospheric variations lead to the fluctuation of the noise levels measured or predicted in forested areas. The temperature and wind vertical profiles specific to forests have been taken into account in different ways in several numerical prediction models [37,39,40,48,72,84]. The effective sound celerity c_{eff} approach takes into account the wind speed $u(z)$ and temperature $T(z)$ gradients, it is written as [99]:

$$c_{\text{eff}}(z) = c(z) + u(z)\cos\theta = \sqrt{\gamma R T(z)} + u(z)\cos\theta, \tag{1.9}$$

where R is the gas constant, γ is the ratio of specific heats and θ is the angle between the wind direction and the sound propagation direction. This relation (1.9) can be seen as the summation of the adiabatic sound speed and the projected wind speed into the propagation direction. Effective sound celerity related to forest is presented, as an example, in figure 1.2. The canopy is well marked at the inflection point of both curves for downwind and upwind propagation.

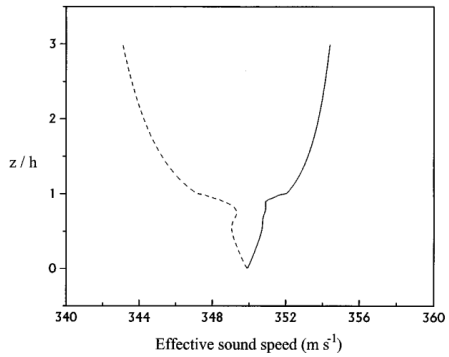

Figure 1.2: *Profiles of effective sound speed through the atmosphere for downwind propagation (solid) and upwind propagation (dashed) inside and above the forest canopy, where h is the height of the canopy and z the height above the ground* [40].

1.4.3 Discussion on the meteorological effects

The morphological characteristics of a forest (structure, height, density, species...) induce the modification of the meteorological conditions. Wind speed, temperature and humidity profiles are the main atmospheric conditions that influence the acoustic propagation. Although the wind and temperature gradients can be smoothed inside a forest (below the canopy) [40,84], for larger distances, the specific modification of the meteorological conditions in presence of forested areas should be taken into account for an accurate prediction of sound propagation through forests.

The hypothesis of homogeneous meteorological conditions inside a forest, *i.e.* below the canopy, can be justified regarding the references presented in this review. In this document, for the study of wave propagation inside forests (Chapter 3 and 4), the meteorological fluctuations are not taken into account. This would constitute an important perspective for future work.

1.5 Synthesis of the literature review

Each physical phenomenon that influences the sound propagation in/through/around forested areas has been treated separately to give an overview of the complex interaction between the acoustic waves and forested environments.

Section 1.2 on the ground effects details the impedance models that are used or developed in relation to forest floors. Characteristic impedance models such as Zwicker and Kosten are used directly to predict the surface ground impedance under the assumption of semi-infinite ground. In addition, structural models are developed to describe a multi-layered floor typical of a forest. Among the measurement techniques, a standing wave tube has been used *in situ* to measure the normal impedance and extract the ground parameters.

Section 1.3 presents the multiple scattering phenomenon caused by obstacles such as trunks, branches or leaves, which directly impact the sound propagation

inside a forest. In the literature, the analytical description of multiple scattering is derived from either energetic or wave theories. The analytic models of interest in the present work are based on wave theory. As a consequence of the scattering, the persistence of sound in certain frequency bands, due to the multiple reflections, can cause an increase of the reverberation time inside forests. An excess attenuation is also expected as a consequence of sound scattering. For instance, in an experimental study of different tree species, it has been shown that the foliage acts as a low pass filter for the acoustic propagation.

The meteorological effects reviewed in section 1.4 have shown that forests lead to the modification of wind, temperature and humidity gradients. Moreover, the heat flow or the wind speed discontinuities induce turbulences. All these atmospheric fluctuations directly impact the propagation of acoustic waves, especially inside and above the canopy.

This literature review shows that forests are complex media, where acoustic waves are impacted by a large number of physical phenomena. This chapter gives some references that might be useful for numerical simulation of acoustic phenomena in forests. This review can be used as an introduction for the future development of a reference model dedicated to the prediction of noise propagation in forests. The literature review on sound scattering (Section 1.3) is extended and used in chapter 3 for the validation of the TLM method in the framework of sound propagation in forests.

In the framework of this thesis, it can be reminded that causal impedance models such as Zwicker and Kosten model can be used for the prediction of the forest ground surface impedance. This can be used with time-domain methods such as the Transmission Line Matrix (TLM) method as shown by Guillaume *et al.* [60]. The ability of the numerical model to take into account single and multiple scattering can be checked by comparing the analytic solutions found in [71, 100]. Finally, meteorological effects could be implemented using the effective celerity approach, considering the celerity profiles proposed in [101].

Chapter 2

ABSORBING MATCHED LAYERS FOR THE TRANSMISSION-LINE MATRIX METHOD

In most numerical methods, the simulation of outdoor sound propagation requires to consider absorbing boundaries in order to avoid any reflection on the limit of the numerical domain. Among all absorbing boundary approaches, the efficiency of the perfectly matched layer (PML) formulation has been proved for many numerical methods in acoustics, as for instance, the FDTD method. Although some interesting, but empirical, absorbing layer approach has already been proposed for the TLM, the PML formulation has not yet been implemented for this method. Since the PML theory could increase the efficiency of the method, it is investigated in this chapter.

This chapter is made of two main sections. Section 2.1 introduces the TLM method for general heterogeneous and dissipative media. Section 2.2 is an original contribution proposed in this thesis. It consists in the development of absorbing layer formulations based on rigorous analytical derivations for the TLM method in acoustics. The content of this second part is the subject of a paper accepted by the Journal of Sound and Vibration.

2.1 Presentation of the transmission-line matrix (TLM) method

2.1.1 Introduction

The transmission-line matrix (TLM) method can be seen as a numerical technique for the calculation of acoustic fields. A discretized transmission-line network is made of nodes connected to each other through transmission-lines. The pulses are transmitted from a node to the adjacent ones through the lines. In acoustics, it is probably more relevant to see these lines as tubes, which are the connexions between volumes (the nodes), as mentioned by Kagawa *et al.* [102]. However, in this

document, it has been chosen to keep the terms "branches" and "nodes", as they are the most frequently used for the TLM description.

The TLM method has originally been developed for electromagnetism simulations and is based on the analogy between a space and time dependent physical problem and an electrical network. It has first been introduced in 1971 by Johns and Beurle [103]. Among the advantages of the TLM method, Johns and Beurle [103] identify the possibility of transient analysis, *e.g.* a TLM simulation can be used for the study of a system response to an impulse excitation source. In this sense, a TLM result is in the time-domain and may cover a broad frequency range [103]. Through the first decades, the TLM method has been gradually developed through the study of boundary problems [104, 105]. A method has been also introduced to condense the electromagnetic field components through the symmetrical condensed node approach [106], and thus, to simplify the implementation of the TLM method.

In acoustics, the TLM method has first been introduced in 1990 by Saleh and Blanchfield [107] for the study of an array of transducers. El-Masri *et al.* [108] implemented the TLM method to study the acoustic propagation in a vocal tract, where Taylor's expansion is used to define an absorbing boundary condition. Kagawa *et al.* [44,102] studied wave propagation in heterogeneous and dissipative media, which has been expanded more recently by Hofmann and Heutschi [45]. For a detailed literature review on the TLM method for acoustics, the reader can refer to Guillaume's PhD thesis [47].

In a first approach, section 2.1.2 aims at describing the TLM method for two-dimensional (2D) propagation cases. The TLM method is introduced for the general case of wave propagation in heterogeneous and dissipative media. This presentation details the numerical steps related to acoustic wave propagation in a TLM-network, and recalls the main notations that are used for the developments of the method. Although the TLM method has originally been developed using an empirical approach, the link between the numerical method and the acoustic wave equation is clearly stated in section 2.1.2.4. Moreover, a condition is set on the TLM celerity in order to verify the Courant-Friedrich-Levy (CFL) stability criterion for a simplified form of the TLM wave equation (Section 2.1.2.5).

2.1.2 Description of the TLM method

In this section, for simplicity, the TLM method is described considering a 2D propagation domain. Appendix A generalizes the TLM formulation in 3D.

2.1.2.1 Principle

The TLM method is a numerical approach that simulates acoustic wave propagation inside a regular discretized network, made of *nodes* and *transmission lines* (also named *branches*). In the transmission-line network, the node position is given by the indexes (i, j) that correspond to the discretization of the spatial continuous variables (x, y) used in a 2D Cartesian coordinate system. The spatial step is noted δl and is taken as $\delta l = \delta x = \delta y$. The time step δt corresponds to the duration for an impulse to cover the distance δl in the transmission-line network. Hence, the celer-

ity of the acoustic wave between two consecutive nodes is $c = \delta l/\delta t$. The acoustic pressure $p(x, y, t)$ in the transmission-line network is written ${}_t p_{(i,j)}$.

In the TLM network, the sound propagation is modeled as *indicent* and *scattered* pressure pulses travelling from a node to its neighbours through transmission lines. The transformation of incident pulses to scattered pulses at every node is called the *scattering process*. Moreover, each node is connected to neighbours through *connexion laws*. Both scattering process and connexion laws describe the transmission-line network properties, and will be detailed in section 2.1.2.3.

For a 2D homogeneous and non-dissipative propagation medium, each node is connected to four branches. Incident pulses ${}_t I^n_{(i,j)}$ and scattered pulses ${}_t S^m_{(i,j)}$ for a given node position (i, j) are depicted by figure 2.1. Superscripts n and m ($n, m \leq 4$) correspond to the number of the main branches where pulses are traveling. Following a vector notation, incident and scattered pulses can be re-arranged as follows:

$$ {}_t\mathbf{I}_{(i,j)} = [\, {}_t I^1;\ {}_t I^2;\ {}_t I^3;\ {}_t I^4]^T_{(i,j)}, \tag{2.1a} $$

$$ {}_t\mathbf{S}_{(i,j)} = [\, {}_t S^1;\ {}_t S^2;\ {}_t S^3;\ {}_t S^4]^T_{(i,j)}, \tag{2.1b} $$

where the exponent T denotes the transpose operator.

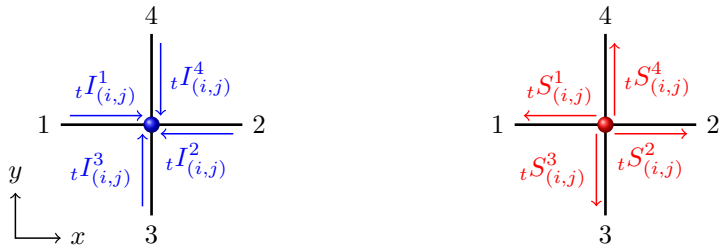

Figure 2.1: *Incident* ${}_t I^n_{(i,j)}$ *and scattered* ${}_t S^m_{(i,j)}$ *pulses for a node* (i, j) *at the time* t *for an homogeneous and non-dissipative medium (2D).*

2.1.2.2 Transmission-lines impedance

Characteristic impedance of main branches

In a 2D transmission-line network, for an homogeneous and non-dissipative propagation medium, all main branches ($n, m \leq 4$) are defined by a characteristic impedance, denoted Z_0 and given by:

$$ Z_0 = \rho_0 c_0, \tag{2.2} $$

where ρ_0 is the medium density and c_0 is the acoustic celerity in the medium that should be equal to the apparent propagation celerity c_{TLM} in the transmission-line network ($c_{\text{TLM}} = c_0$, Section 2.1.2.5).

Propagation medium with discontinuities: heterogeneity branch

In the case of outdoor sound propagation, physical phenomena such as meteorological effects induce heterogeneities in the propagation fluid. In the TLM approach, the fluid heterogeneities are approximated as small discontinuities in the propagation medium properties, where the characteristic size is, at least, of the order of the network spatial step. Acoustic propagation in non-homogeneous fluid induces refraction of acoustic waves caused by the local variation of the sound celerity [91]. Within the TLM concept, it has been shown [102] that an additional branch on each node can be used to set the local sound celerity. This approach introduces the parameter η, which can be used to modify the local impedance through an additional fifth branch of length $\delta l/2$. This branch presents a characteristic impedance Z_0/η (Figure 2.2). The heterogeneity that is introduced in the transmission-line network is isotropic.

Propagation medium with dissipation: dissipative branch

In outdoor sound propagation, sound attenuation can be caused by either geometrical divergence and/or atmospheric absorption. Although geometrical divergence is naturally taken into account in the TLM method, the atmospheric absorption can be simulated, for a given frequency, by adding a branch [102] at each node of the TLM network. This branch presents an anechoic termination and a specific impedance Z_0/ζ (Figure 2.2).

As the termination of the dissipative branch is anechoic, the wave that travels in such a branch is neither transmitted nor reflected. Hence, dissipation in the TLM method is made up *via* an attenuation factor that introduces a damping at every node (Section 2.2.4.3).

2.1.2.3 TLM formalism for propagation in heterogeneous and dissipative media

The TLM formulation for an heterogeneous and dissipative medium requires to consider two additional branches, as depicted in figure 2.2. The only additional branch responsible for the modification of the local celerity is the heterogeneity branch, since the dissipation branch is anechoic. Thus, the vector notation for heterogeneous and dissipative medium deals with five incident and scattered pulses [46]:

$$ {}_t\mathbf{I}_{(i,j)} = [\, {}_tI^1;\ {}_tI^2;\ {}_tI^3;\ {}_tI^4;\ {}_tI^5]^T_{(i,j)}, \tag{2.3a} $$

$$ {}_t\mathbf{S}_{(i,j)} = [\, {}_tS^1;\ {}_tS^2;\ {}_tS^3;\ {}_tS^4;\ {}_tS^5]^T_{(i,j)}, \tag{2.3b} $$

where ${}_tI^5$ and ${}_tS^5$ correspond to incident and scattered pulses from the additional fifth branch that aims at introducing heterogeneities in the transmission-line network.

Scattering process

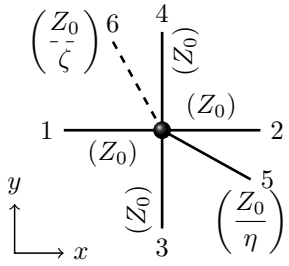

Figure 2.2: *Additional branches for acoustic propagation in an heterogeneous and dissipative medium (2D).*

The scattering process for each node of the transmission-line network is described by the following equation:

$$ {}_t\mathbf{S}_{(i,j)} = {}_t\mathbf{D}_{(i,j)}\ {}_t\mathbf{I}_{(i,j)}, \tag{2.4} $$

where the scattering matrix ${}_t\mathbf{D}_{(i,j)}$ is derived for the transmission and reflection coefficients (Appendix A) for wave propagation in an heterogeneous and dissipative 2D network is given by:

$$ {}_t\mathbf{D}_{(i,j)} = \frac{2}{\eta_{(i,j)} + \zeta_{(i,j)} + 4}\ {}_t \begin{bmatrix} a & 1 & 1 & 1 & \eta \\ 1 & a & 1 & 1 & \eta \\ 1 & 1 & a & 1 & \eta \\ 1 & 1 & 1 & a & \eta \\ 1 & 1 & 1 & 1 & b \end{bmatrix}_{(i,j)} . \tag{2.5} $$

The fifth column of the scattering matrix (2.5) corresponds to the fifth branch that accounts for the fluid heterogeneities. Dissipation is taken into account through coefficients that depend on the term ζ. The matrix coefficients are written:

$$ a_{(i,j)} = -\frac{\eta_{(i,j)}}{2} - \frac{\zeta_{(i,j)}}{2} - 1, \tag{2.6a} $$

$$ b_{(i,j)} = \frac{\eta_{(i,j)}}{2} - \left(\frac{\zeta_{(i,j)}}{2} + 2\right). \tag{2.6b} $$

Relations (2.4) and (2.5) give scattered pulses, in relation to incident pulses at a node position (i, j), as follows:

$$ \sum_{m=1}^{4} {}_tS^m_{(i,j)} + {}_tS^5_{(i,j)} = \frac{\eta_{(i,j)} - \zeta_{(i,j)} + 4}{\eta_{(i,j)} + \zeta_{(i,j)} + 4} \left[\sum_{n=1}^{4} {}_tI^n_{(i,j)} + \eta_{(i,j)}\ {}_tI^5_{(i,j)} \right]. \tag{2.7} $$

Acoustic pressure

The superposition principle gives the acoustic pressure at a given node position as follows:

$$ {}_tp_{(i,j)} = \frac{2}{\eta_{(i,j)} + \zeta_{(i,j)} + 4} \left[\sum_{n=1}^{4} {}_tI^n_{(i,j)} + \eta_{(i,j)}\ {}_tI^5_{(i,j)} \right]. \tag{2.8} $$

Equation (2.7) can also be rewritten using equations (2.4) and (2.8), leading to:

$$ {}_tS^n_{(i,j)} = {}_tp_{(i,j)} - {}_tI^n_{(i,j)}. \tag{2.9}$$

A scattered pulse from branch n is then expressed as a function of the acoustic pressure at corresponding node (i,j) and of the incident pulse in the same branch.

Connexion laws

At a given node position (i,j), each scattered pulse ${}_tS^m$ covers the discretized distance δl during the time δt and becomes an incident pulse ${}_{t+\delta t}I^n$ at an adjacent node. For the node position (i,j) this is written as:

$$ {}_{t+\delta t}I^1_{(i,j)} = {}_tS^2_{(i-1,j)}, \tag{2.10a}$$

$$ {}_{t+\delta t}I^2_{(i,j)} = {}_tS^1_{(i+1,j)}, \tag{2.10b}$$

$$ {}_{t+\delta t}I^3_{(i,j)} = {}_tS^4_{(i,j-1)}, \tag{2.10c}$$

$$ {}_{t+\delta t}I^4_{(i,j)} = {}_tS^3_{(i,j+1)}. \tag{2.10d}$$

$$ {}_{t+\delta t}I^5_{(i,j)} = {}_t\,S^5_{(i,j)}. \tag{2.10e}$$

The set of equations (2.10) are the connexion laws for a 2D heterogeneous and dissipative transmission-line network. Equation (2.10e) is the additional connexion law that corresponds to the heterogeneity branch.

2.1.2.4 Relation between the TLM propagation scheme and the wave equation

Connexion laws (2.10) associated to the acoustic pressure formulation (Eq. (2.8)) give:

$$ \frac{\eta_{(i,j)}+\zeta_{(i,j)}+4}{2}\,{}_{t+\delta t}p_{(i,j)} = {}_tS^2_{(i-1,j)} + {}_tS^1_{(i+1,j)} + {}_tS^4_{(i,j-1)} + {}_tS^3_{(i,j+1)} + \eta_{(i,j)}\,{}_tS^5_{(i,j)}. \tag{2.11}$$

Equation (2.9) is used to expand equation (2.11) that gives:

$$ \begin{aligned} \frac{\eta_{(i,j)}+\zeta_{(i,j)}+4}{2}\,{}_{t+\delta t}p_{(i,j)} = {}&{}_tp_{(i-1,j)} - {}_tI^2_{(i-1,j)} + {}_tp_{(i+1,j)} - {}_tI^1_{(i+1,j)} \\ &+ {}_tp_{(i,j-1)} - {}_tI^4_{(i,j-1)} + {}_tp_{(i,j+1)} - {}_tI^3_{(i,j+1)} \\ &+ \eta_{(i,j)}\,{}_tp_{(i,j)} - \eta_{(i,j)}\,{}_tI^5_{(i,j)}. \end{aligned} \tag{2.12}$$

Equation (2.12) is then rewritten using connexion laws (2.10):

$$ \begin{aligned} \frac{\eta_{(i,j)}+\zeta_{(i,j)}+4}{2}\,{}_{t+\delta t}p_{(i,j)} = {}&{}_tp_{(i-1,j)} + {}_tp_{(i+1,j)} + {}_tp_{(i,j-1)} + {}_tp_{(i,j+1)} \\ &+ \eta_{(i,j)}\,{}_tp_{(i,j)} - \left[\sum_{m=1}^{4} {}_{t-\delta t}S^m_{(i,j)} + \eta_{(i,j)}\,{}_{t-\delta t}S^5_{(i,j)}\right]. \end{aligned} \tag{2.13}$$

Finally, the summation of the scattered pulses in equation (2.13) is rewritten using equations (2.7) and (2.8), to give:

$$
\begin{aligned}
{}_{t+\delta t}p_{(i,j)} =& \frac{2}{\eta_{(i,j)}+\zeta_{(i,j)}+4}\left[\,{}_{t}p_{(i+1,j)} + \,{}_{t}p_{(i-1,j)} + \,{}_{t}p_{(i,j+1)} + \,{}_{t}p_{(i,j-1)} + \eta_{(i,j)}\,{}_{t}p_{(i,j)}\right] \\
&- \frac{\eta_{(i,j)}-\zeta_{(i,j)}+4}{\eta_{(i,j)}+\zeta_{(i,j)}+4}\,{}_{t-\delta t}p_{(i,j)},
\end{aligned}
\tag{2.14}
$$

which corresponds to the TLM propagation scheme for an heterogeneous and non-dissipative medium.

After rearrangement and approximation of the space and spatial derivatives based on first and second order centered finite differences

$$
\frac{\partial p(x,y,t)}{\partial t} \sim \frac{p(x,y,t+\delta t) - p(x,y,t-\delta t)}{2\delta t} \equiv \frac{{}_{t+\delta t}p_{(i,j)} - {}_{t-\delta t}p_{(i,j)}}{2\delta t}, \tag{2.15a}
$$

$$
\frac{\partial^2 p(x,y,t)}{\partial t^2} \sim \frac{p(x,y,t+\delta t) - 2p(x,y,t) + p(x,y,t-\delta t)}{\delta t^2} \equiv \frac{{}_{t+\delta t}p_{(i,j)} - 2\,{}_{t}p_{(i,j)} + {}_{t-\delta t}p_{(i,j)}}{\delta t^2}, \tag{2.15b}
$$

$$
\frac{\partial^2 p(x,y,t)}{\partial x^2} \sim \frac{p(x+\delta x,y,t) - 2p(x,y,t) + p(x-\delta x,y,t)}{\delta x^2} \equiv \frac{{}_{t}p_{(i+1,j)} - 2\,{}_{t}p_{(i,j)} + {}_{t}p_{(i-1,j)}}{\delta x^2}, \tag{2.15c}
$$

$$
\frac{\partial^2 p(x,y,t)}{\partial y^2} \sim \frac{p(x,y+\delta y,t) - 2p(x,y,t) + p(x,y-\delta y,t)}{\delta y^2} \equiv \frac{{}_{t}p_{(i,j+1)} - 2\,{}_{t}p_{(i,j)} + {}_{t}p_{(i,j-1)}}{\delta y^2}, \tag{2.15d}
$$

the TLM propagation scheme (2.14) can be identified to:

$$
\left[\left(\frac{\partial^2}{\partial x^2}+\frac{\partial^2}{\partial y^2}\right) - \frac{\eta+4}{2}\frac{\delta t^2}{\delta l^2}\frac{\partial^2}{\partial t^2} - \zeta\frac{\delta t}{\delta l^2}\frac{\partial}{\partial t}\right]\,{}_{t}p_{(i,j)} = 0. \tag{2.16}
$$

Equation (2.16) corresponds to the wave equation for propagation in an heterogeneous and dissipative network, where the celerity in the TLM network c_{TLM} is given by:

$$
c_{\mathrm{TLM}} = \sqrt{\frac{2}{\eta+4}}\,c, \tag{2.17}
$$

where $c = \delta l/\delta t$ is the celerity between two consecutive nodes.

This rewrite demonstrates that the TLM principle is in perfect agreement with the wave theory, although the TLM starts from a physical principle (*i.e.* Huygens' principle) and not from the acoustic equations.

2.1.2.5 The celerities and the CFL stability criterion

This section aims at relating the celerity in the TLM network to the Courant-Friedrich-Levy (CFL) stability criterion [109], also named Courant number, which is a necessary condition for the model stability. The Courant number can be seen as a dimensionless spatial transport per time step. In this study, the dissipation term in the wave equation (2.16) is set equal to zero, which gives

$$
\left[\left(\frac{\partial^2}{\partial x^2}+\frac{\partial^2}{\partial y^2}\right) - \frac{1}{c_{\mathrm{TLM}}^2}\frac{\partial^2}{\partial t^2}\right]\,{}_{t}p_{(i,j)} = 0. \tag{2.18}
$$

The celerity inside the TLM network c_{TLM} can be related to the CFL condition by considering an harmonic solution for the pressure written as:

$$ {}_{t}p_{(i,j)} = P_0 e^{\jmath(\omega t - k_x x - k_y y)}, \tag{2.19} $$

where P_0 is the amplitude of the acoustic pressure, ω the angular frequency, k_x and k_y are the wave numbers relative to respectively, the x and y cartesian coordinates. Substituting this harmonic solution in the wave equation (2.18) gives

$$ \frac{e^{-\jmath k_x \delta x} - 2 + e^{\jmath k_x \delta x}}{\delta x^2} + \frac{e^{-\jmath k_y \delta y} - 2 + e^{\jmath k_y \delta y}}{\delta y^2} = \frac{1}{c_{\mathrm{TLM}}^2} \frac{e^{-\jmath \omega \delta t} - 2 + e^{\jmath \omega \delta t}}{\delta t^2}. \tag{2.20} $$

This can be rewritten using Euler formula $\cos x = \frac{e^{\jmath x} + e^{-\jmath x}}{2}$ and the relation $\sin^2 x = \frac{1-\cos 2x}{2}$ as:

$$ \left[\frac{1}{\delta x} \sin\left(\frac{k_x \delta x}{2}\right)\right]^2 + \left[\frac{1}{\delta y} \sin\left(\frac{k_y \delta y}{2}\right)\right]^2 = \left[\frac{1}{c_{\mathrm{TLM}} \delta t} \sin\left(\frac{\omega \delta t}{2}\right)\right]^2. \tag{2.21} $$

The angular frequency can be written as:

$$ \omega = \frac{2}{\delta t} \arcsin\left(c_{\mathrm{TLM}} \delta t \sqrt{\left[\frac{1}{\delta x} \sin\left(\frac{k_x \delta x}{2}\right)\right]^2 + \left[\frac{1}{\delta y} \sin\left(\frac{k_y \delta y}{2}\right)\right]^2} \right). \tag{2.22} $$

In order for the harmonic solution to not be an evanescent wave (*i.e.* exponentially decreasing in magnitude) and because $\arcsin(x) = \int_0^x \frac{1}{\sqrt{1-t^2}} dt$, we have:

$$ c_{\mathrm{TLM}} \delta t \sqrt{\left[\frac{1}{\delta x} \sin\left(\frac{k_x \delta x}{2}\right)\right]^2 + \left[\frac{1}{\delta y} \sin\left(\frac{k_y \delta y}{2}\right)\right]^2} \leqslant 1. \tag{2.23} $$

Reminding that $\delta x = \delta y = \delta l$, this gives in the worst case (*i.e.* $\sin^2(x) = 1$)

$$ c_{\mathrm{TLM}} \delta t \leqslant \frac{1}{\sqrt{\frac{2}{\delta l^2}}}, \tag{2.24} $$

which corresponds to the CFL condition. This can be generalized for n_d dimensions (Appendix A), where the Courant number is written:

$$ c_{\mathrm{TLM}} \frac{\delta t}{\delta l} = \frac{c_{\mathrm{TLM}}}{c} \leqslant \frac{1}{\sqrt{n_d}}. \tag{2.25} $$

For a 2D Cartesian TLM-networks, the CFL condition is written

$$ \sqrt{2} c_{\mathrm{TLM}} \leqslant c. \tag{2.26} $$

In order to have a full overview of the celerity formalisms used in the present approach, table 2.1 summarizes all different celerities used in the TLM formulation.

	Name	Domain	Scale	Description	Expression
c	Branch celerity	Numeric	Microscopic	Celerity between two consecutive nodes.	$c = \delta l/\delta t$, with δl: numerical spatial step, δt: numerical time step.
c_{TLM}	TLM celerity	Numeric	Macroscopic	Celerity over a macroscopic region.	Homog.: $c_{\text{TLM}} = \frac{1}{\sqrt{2}} c$ (2D) ; Heterog.: $c_{\text{TLM}} = \sqrt{\frac{2}{\eta+4}}\, c$ (2D)
c_0	Adiabatic sound celerity	Acoustic	Macroscopic	Physical sound speed in free field	$c_0 = \sqrt{\gamma RT}$, with γ: ratio of specific heats, R: gas constant.
c_{eff}	Effective celerity	Acoustic	Macroscopic	Sound speed for temperature T and wind speed u fluctuations.	Eq. (1.9)

Table 2.1: *Definition of the celerities used for the 2D TLM description (see Appendix A for 3D relations).*

2.1.3 Implementation of the TLM method

During this thesis, depending on the purpose of the study, the TLM method has been developed using three scientific programming languages. Firstly, the open source Scilab programming language is used to compute 2D TLM domains such as for the absorbing layers and the single scattering presented in, respectively, Chapter 2 and the first part of Chapter 3. These scripts are named **Scilab-TLM code**. Because of the restriction of the Scilab stack-size memory, most of the Scilab scripts have been rewritten using Matlab programming language. These scripts are named **Matlab-TLM code**. Lastly, the TLM Python/OpenCL code developed at Ifsttar[1] has been used for 3D calculations (Chapter 3 and 4). This code uses Graphics Processing Unit (GPU) as the main computational resource for the TLM calculation. These scripts are named **Python/OpenCL-TLM code**.

In addition, TLM calculations have been performed on the High-Performance Computing (HPC) department of Strasbourg University. The HPC numerical resources are made of more than 3500 processors and 11 TO of random-access memory storage. The six GPUs dedicated to scientific calculations are NVIDIA Tesla K20 and K40 devices. The HPC cluster has been used with both **Scilab-TLM code** and **Python/OpenCL-TLM code**.

2.2 An absorbing matched layer implementation for the Transmission-Line Matrix (TLM) method

2.2.1 Introduction

Computational resources are often a limitation for the numerical simulation of long range sound propagation. Especially, time domain methods such as FDTD or TLM methods for acoustics still require substantial computational power. Simulations of

[1]French institut of science and technology for transport, development and networks

free-field wave propagation should be equivalent to wave propagation in an infinite domain but in practice the computational domain is always finite. Furthermore, the truncation of the propagation domain can be seen as an approach to minimize computational burden. Therefore, the truncation, *i.e.* the artificial numerical boundary, should not impact the propagation domain of interest. The methods that prevent from phenomena such as unwanted reflections can be divided into two categories: absorbing boundaries and absorbing layers.

Considering the TLM method, absorbing boundaries have shown limited interest, *e.g.* some of them induce instabilities and/or are only efficient for normal incidence. Therefore, absorbing layer methods appear to be more promising for the TLM method. Two absorbing layer methods have already been tested with the TLM method: the dissipative medium [45] and the matched connexion law [47,110]. Known as an efficient absorbing layer in several numerical methods such as the FDTD, the perfectly matched layer (PML) has not been yet adapted to the TLM method. Initially proposed by Bérenger in electromagnetism [111], the PML theory has been used in several methods for acoustic simulations. This approach shows convincing performances in most calculation methods, thus its adaptation to the TLM method in acoustics would be interesting. The present section aims at proposing an approximate PML implementation for the TLM method.

A review of the absorbing conditions used for the TLM method in acoustics is presented in sections 2.2.2. The PML theory is emphasized in section 2.2.3 to give the main background that would lead to the derivation of an absorbing layer formulation for the TLM method. Section 2.2.4 presents an adaptation of the PML theory to the TLM method through the identification of the PML attenuation factor and the heterogeneous and dissipative TLM terms. Section 2.2.5 presents two approximate PML formulations for the TLM, renamed as absorbing matched layers (AML), which are compared to the absorbing layer used as a reference in the TLM method for acoustics (*i.e.* the one-way approach, Section 2.2.2.2).

2.2.2 Overview of the absorbing conditions used for the TLM method

This review aims at presenting the approaches that have already been implemented to simulate absorbing condition in the TLM method for acoustics. Two kinds of absorbing conditions are distinguished in this presentation: the absorbing boundaries and the absorbing layers. The efficiency in terms of reflection error is discussed for each approach.

2.2.2.1 Absorbing boundaries

The aim of absorbing boundaries is to simulate infinite space by means of conditions that are imposed on the boundaries of the propagation domain of interest. Such boundaries can be seen as damping termination and are usually applied to the nodes that constitute the limit of the computational domain. Two kinds of absorbing boundaries for TLM method are found in the literature: the real impedance condition and the boundary operator method.

Real impedance boundary condition

Real impedance boundary condition consists in imposing directly a purely real impedance at the nodes that constitute the boundary of the propagation domain. This impedance is estimated from the theoretical reflection coefficient.

The matching condition is one of the first real impedance boundary condition that has been implemented for numerical modeling. This condition is defined using the characteristic impedance Z_0 of the propagation domain of interest. For an incidence angle θ with respect to the normal to the boundary, the theoretical reflection coefficient is given by:

$$R(\theta) = \frac{Z\cos\theta - Z_0}{Z\cos\theta + Z_0}. \tag{2.27}$$

For normal incidence ($\theta = 0 \Rightarrow \cos\theta = 1 \Rightarrow R = 0$), matching condition consists in replacing the truncated medium that surrounds the propagation domain of interest by its characteristic impedance Z_0. In the TLM method, matching condition at node location (i,j) between the scattered $S_{(i,j)}$ pulses at time t and the incident $I_{(i,j)}$ pulses at time $t+\delta t$ is expressed through the connexion laws (2.10) as:

$${}_{t+\delta t}I_{(i,j)} = R(\theta)\ {}_tS_{(i,j)}\ . \tag{2.28}$$

Hofmann and Heutschi [45] defined an absorbing boundary based on empirical simulations for the TLM method. They confirmed that a matched impedance condition $Z = Z_0$ does not give satisfying results for grazing incidence, whereas $Z = \sqrt{2}Z_0$ can most likely be interpreted as free-field impedance boundary for a regular transmission-line network. However, this last solution gives strong reflections for normal incidence (Section 2.2.2.3) and is still not acceptable for acoustic simulations. Therefore, the authors advised to use an absorbing layer approach as presented in section 2.2.2.2.

Boundary operator method

The boundary operator method consists in estimating numerically the pressure field that would be reflected at the limit of the propagation domain. The estimated acoustic pressure coming from the boundary is canceled by subtracting it from the effective pressure field. Among the boundary operators used for the TLM method, two methods can be distinguished: Taylor's series expansion and Higdon's operator.

Taylor's series expansion has been first introduced by Saguet [112] for electromagnetism. It has been used by El-Masri *et al.* [108] for the simulation of acoustic wave propagation in vocal tracts. This approach is based on the definition of a reflection coefficient that is implemented in the TLM method *via* the connexion laws. For a node position (i,j), at time t, Taylor series expansion for the TLM method gives:

$${}_tR(i,j) = 2.5\ {}_{t-\delta t}R(i-1,j) - 2\ {}_{t-2\delta t}R(i-2,j) + 0.5\ {}_{t-3\delta t}R(i-3,j), \tag{2.29}$$

where ${}_tR(i,j)$ is the reflection coefficient at time t and at the node (i,j), δt is the time step. In equation (2.29), the reflection coefficient is given for wave propagation along the x-axis. Notations and process for the reflection coefficients are depicted

by figure 2.3. Although Taylor's series expansion predicts the reflected pressure for normal incidence more accurately than matching condition, it introduces numerical instabilities [47, 113] (Section 2.2.2.3).

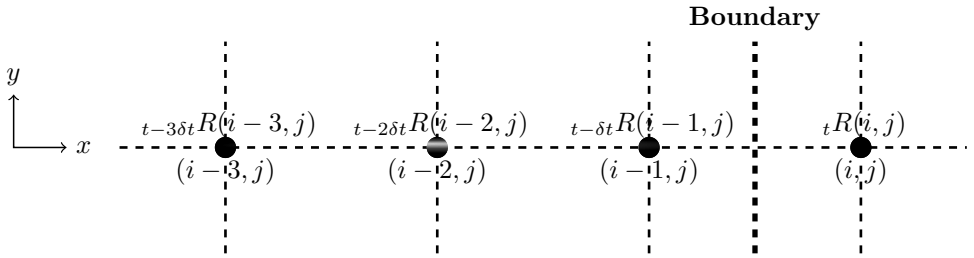

Figure 2.3: *Reflection coefficients in the TLM network used for Taylor's series expansion.*

Higdon's operator [114] is another approach still based on numerical estimation of an accurate reflection coefficient for the boundary. In acoustics, the theory of Higdon's operator has been applied to FDTD [115] and TLM [116] methods. Higdon's theory has been extended and generalized by the complementary operators method (COM) [115]. Its efficiency is discussed in section 2.2.2.3.

2.2.2.2 Absorbing layers

Absorbing layers are applied to a larger portion of the computational domain than absorbing boundaries. This leads to a gradual dissipation of the incident acoustic field inside the absorbing layer.

Although absorbing layers require more computational power than absorbing boundaries, it has been shown [47, 113] that interesting results can be obtained for the TLM method.

Absorbing layers can be seen as an artificial absorbing material that is placed adjacent to the edges of the propagation domain of interest, as depicted in figure 2.4. The amplitude of a wave that propagates in the absorbing layer decays significantly due to the absorption process of the medium. In this sense, absorbing layers are usually used to reduce the numerical domain in order to restrict the whole computational domain. Therefore, absorbing layers must be designed to minimize reflections arising from the truncated boundary. A proper truncation of the simulation domain would prevent from computational overload.

Dissipative medium

Kagawa [102], as well as Hofmann and Heutschi [45] proposed to use the definition of lossy media for the TLM method. Lossy medium for a transmission-line network is based on the addition of a branch at each node inside the absorbing layer. This branch has a specific impedance ζ and its termination is anechoic to avoid any reflection. Therefore, this approach requires only the dissipative coefficient ζ, which should increase slightly inside the layer to prevent unwanted reflections. This dissipation process is implemented through the scattering matrix in the TLM method.

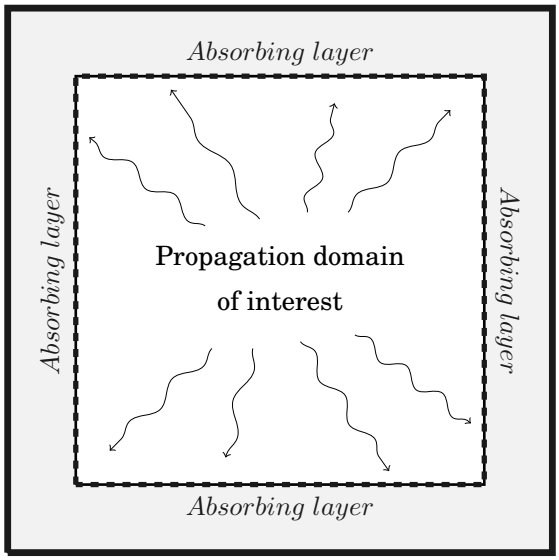

Figure 2.4: *Schematic representation of a propagation domain surrounded by an absorbing layer.*

Hofmann and Heutschi [45] suggest to size this absorbing layer with about 500 nodes for a spatial step equal to $\delta l = \lambda/10$ (where λ is the wavelength), which represents a significant burden in terms of computational cost.

Matched connexion laws

The matched connexion laws approach has first been introduced by de Cogan [110]. This approach consists in multiplying the scattered pulses by an attenuation factor $F_{(i,j)}$ *via* the connexion laws (Eqs. (2.30)). This attenuation factor aims at simulating a graded loading of transmission-lines. Therefore, this approach is named by the author as *Graded Perfectly Matched Load* (GPML). For 2D transmission line network, at node location (i, j), this can be written as:

$$ {}_{t+\delta t}I^1_{(i,j)} = F_{(i,j)} \times {}_tS^2_{(i-1,j)}, \tag{2.30a} $$

$$ {}_{t+\delta t}I^2_{(i,j)} = F_{(i,j)} \times {}_tS^1_{(i+1,j)}, \tag{2.30b} $$

$$ {}_{t+\delta t}I^3_{(i,j)} = F_{(i,j)} \times {}_tS^4_{(i,j-1)}, \tag{2.30c} $$

$$ {}_{t+\delta t}I^4_{(i,j)} = F_{(i,j)} \times {}_tS^3_{(i,j+1)}. \tag{2.30d} $$

It is important to note that the attenuation factor is applied on each connexion law, *i.e.* following the two Cartesian directions x and y. The proposed formulation for the attenuation factor $F(i, j)$ given by de Cogan [110] for a layer thickness e_{AL} is written:

$$ F_{(i,j)} = 1 - \exp\left[\frac{-(x_{(i,j)} - e_{\text{AL}})^2}{A}\right], \tag{2.31} $$

where $x_{(i,j)}$ is the normal distance between a point inside the absorbing layer and its boundary with the computational domain. The factor A is a constant that determines the rate of the decay.

Matched connexion law optimization: the one way approach

Guillaume [47, 113] proposed an optimized formulation of the matched connexion laws. Instead of applying the attenuation factor on the four connexion laws, Guillaume's formulation [47] treats only the connexion law normal to the boundary for outgoing waves, similarly to the PML approach (Section 2.2.3). Considering an outgoing direction following the impulse $I^1_{(i,j)}$, the matched connexion laws are rewritten as:

$$ {}_{t+\delta t}I^1_{(i,j)} = F_{(i,j)} \times {}_tS^2_{(i-1,j)}, \tag{2.32a} $$

$$ {}_{t+\delta t}I^2_{(i,j)} = {}_tS^1_{(i+1,j)}, \tag{2.32b} $$

$$ {}_{t+\delta t}I^3_{(i,j)} = {}_tS^4_{(i,j-1)}, \tag{2.32c} $$

$$ {}_{t+\delta t}I^4_{(i,j)} = {}_tS^3_{(i,j+1)}. \tag{2.32d} $$

As the solution $F_{(i,j)} = 0$ can generate instabilities, the attenuation factor is redefined as:

$$ F_{(i,j)} = (1+\epsilon) - \exp\left[-\frac{(x_{(i,j)} - e_{\mathrm{AL}})^2}{A}\right], \tag{2.33} $$

where $\epsilon = 10^{-5}$ and where the decay constant A is given by:

$$ A = -\frac{e^2_{\mathrm{AL}}}{\ln \epsilon}. \tag{2.34} $$

This absorbing layer formulation (Eqs. (2.32) and (2.33)) is named "Guillaume's matched connexion law" or simply "one-way" in this document.

The shape of the attenuation factor $F_{(i,j)}$ is shown in figure 2.5 as a function of the equivalent thickness of the layer in wavelength unit λ: $N_{\lambda_{\mathrm{AL}}} = e_{\mathrm{AL}}/\lambda$. The attenuation factor is decreasing from $F_{(i,j)} = 1$ to $F_{(i,j)} = \epsilon$ at the end of the absorbing layer. Such an absorbing layer can be considered as perfectly matched to the propagation domain of interest. Furthermore, it can be seen from figure 2.5 that the attenuation factor is gradually decreased when the distance inside the layer increases. This graded loadings inside the absorbing layer nodes is more progressive when reducing the value of ϵ. Therefore, a reduced value of ϵ leads to a minimization of the unwanted reflection coming from the absorbing layer. Thus, the parameter ϵ is usually chosen as equal to 10^{-5} [47, 48, 113].

2.2.2.3 Discussion on the existing absorbing conditions for the TLM method

All results presented in this section (Figures 2.7, 2.8, 2.9) are based on the geometry depicted in figure 2.6.

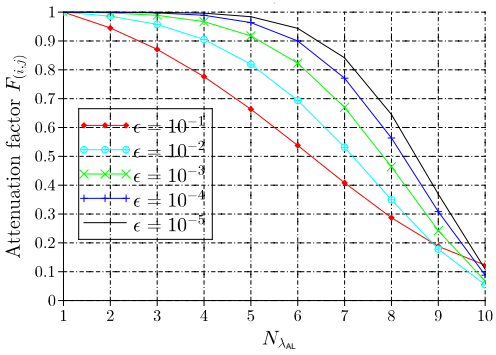

Figure 2.5: *Attenuation factor $F_{(i,j)}$ as function of the absorbing layer thickness $N_{\lambda_{\mathrm{AL}}}$, for five ϵ gradings* [47].

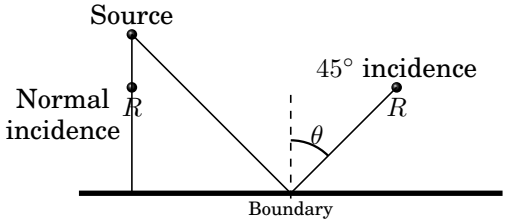

Figure 2.6: *Schematic representation of the sound reflection by a boundary (normal and oblique incidence).*

Efficiencies of the absorbing conditions implemented for the time domain methods

Porti and Morente [116] compared three absorbing conditions: matching condition, Higdon's operator and PML (perfectly matched layer). In their study, the PML has not been implemented directly into the TLM formalism, but through an absorbing FDTD domain connected to the TLM domain. For normal incidence and $45°$ incidence, figure 2.7 shows that PML is more efficient than the two other methods. Matching condition is slightly more efficient than Higdon's operator method at low frequencies. Although the PML appears to be an efficient approach to avoid unwanted reflection from the truncated boundary (Figure 2.7 (a) and (b)), it is important to remind that, in this case [116], the PML has been calculated with the FDTD method.

Schneider and Ramahi [115] studied Higdon's operator and the COM approaches with the FDTD method. Figure 2.8 shows that COM method is slightly more efficient than Higdon's operator. In this study, the reception point is located close to a corner of the propagation domain, *i.e.* surrounded by the boundary.

Guillaume and Picaut [113] compared pressure field reflected at the boundary, *i.e.* the unwanted pressure signals, obtained with Taylor's series expansion, real

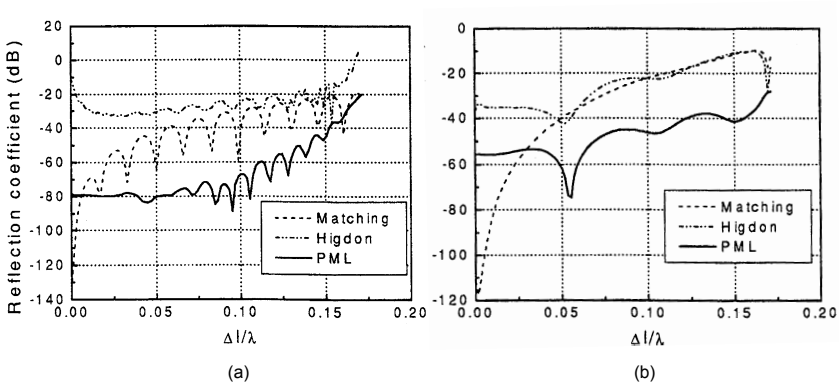

Figure 2.7: *Reflection coefficient for: (a) normal incidence; (b) 45° incidence* [116].

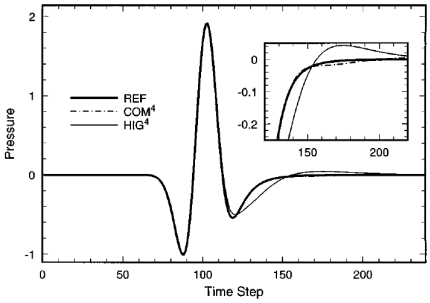

Figure 2.8: *Time pressure signal for* $45°$ *incidence using the average of the two complementary results (COM) and obtained using a Higdon fourth-order operator (HIG). The inset box shows the pressure from time step 120 to 220 with the vertical scale magnified by a factor of 10* [115].

impedance condition, de Cogan's matched connexion laws and its optimized version for the TLM method, *i.e.* the one way approach. From figure 2.9, it can be seen that the optimized matched law proposed by Guillaume [113] attenuates to a larger extent than the original de Cogan formulation. Among the absorbing boundary conditions that have been presented in the previous sections, the matching condition ($Z = Z_0$) presents a significant attenuation but not perfect because of the discretization of the method (*i.e.* regular square mesh). In addition, results obtained with Taylor's series expansion present important instabilities. Finally, the formulation proposed by Guillaume and Picaut [113] gives the most satisfying results in terms of attenuation of the unwanted reflections. It should be noted that these simulations have been carried out at normal incidence, which is an idealized case.

Discussion on the absorbing condition for the TLM method

From this review on absorbing boundaries (Section 2.2.2.1) and absorbing layers (Section 2.2.2.2), it can be seen that absorbing layers show the most convincing results for the TLM method in acoustics. Although absorbing layers are usually more

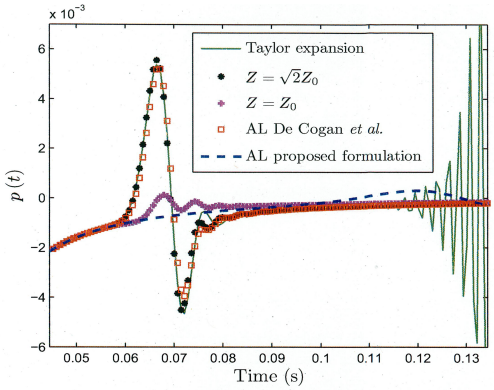

Figure 2.9: *Temporal pressure signals p(t) recorded at normal incidence for absorbing boundaries defined by Taylor's series expansion of the acoustic pressure on the computational limit and by purely real impedance condition ($Z = Z_0$ and $Z = \sqrt{2}Z_0$), compared to the absorbing layers (AL) based on matched connexion laws* [113].

costly to implement, approaches such as Guillaume's matched connexion law [47] and the FDTD-PML [116] remain the most efficient in term of reflection error.

Guillaume's matched connexion law appears to be efficient in term of absorption [47] but still not as efficient as the FDTD-PML [116]. Furthermore, Guillaume's matched connexion law is based on an empirical approach and still requires large layer thickness, which is numerically costly. The PML approach appears to be numerically efficient for time-domain simulation of acoustic wave propagation [116, 117]. Thus, it seems interesting to investigate such a theory in order to obtain a rigorous formulation specifically written for the TLM method. In this view, the following section details the PML theory that would give rise to the development of an approximate PML approach for the TLM method in section 2.2.4.

2.2.3 The perfectly matched layer (PML) theory

The perfectly matched layer (PML) corresponds to a specific absorbing layer introduced by Bérenger [111] to simulate electromagnetic wave propagation in free-space. This means that a propagation domain surrounded by a PML should be theoretically equivalent to a spatially infinite domain. Initially developed for the absorption of electromagnetic waves, this technique has been proved to be also efficient for acoustic propagation simulation based on time domain methods such as FDTD [117]. The main idea behind the PML theory is to define a set of solutions that give large attenuations inside the absorbing layer without producing any unwanted reflections.

Two equivalent formulations for the PML can be distinguished: the split-field PML and the uniaxial-PML (UPML). Both formulations are the result of a complex-coordinate stretching. Complex-coordinate stretching can be seen as a method used to derive the wave equations system for a PML [118]. The following sections briefly present how a PML can be analytically formulated for acoustic wave propagation.

2.2.3.1 Split-field PML formulation

Berenger's original PML formulation [111] is called the split-field PML as it artificially splits the wave solutions into a sum of new artificial field components. Based on an analogy between electromagnetic and acoustic fields, for a 2D acoustic wave propagation case, the acoustic pressure p is split into two additive components: $p = g(x) + h(y)$. The functions g and h are the pressure that only depends on, respectively x and y. The particle velocity $\vec{\mathbf{v}}$ is composed of two components v_x and v_y following the x and y directions respectively. The split-field PML formulation involves the four acoustic components g, h, v_x and v_y, through the mass continuity and momentum equations. In 2D Cartesian coordinates, the PML can be written as:

$$\frac{\partial g}{\partial t} + \rho c_0^2 \frac{\partial v_x}{\partial x} + \sigma_x g = 0, \tag{2.35a}$$

$$\frac{\partial h}{\partial t} + \rho c_0^2 \frac{\partial v_y}{\partial y} + \sigma_y h = 0, \tag{2.35b}$$

$$\rho \frac{\partial v_x}{\partial t} + \frac{\partial p}{\partial x} + \rho \sigma_x v_x = 0, \tag{2.35c}$$

$$\rho \frac{\partial v_y}{\partial t} + \frac{\partial p}{\partial y} + \rho \sigma_y v_y = 0. \tag{2.35d}$$

It is important to note that the momentum equation is split into two equations (2.35a) and (2.35b), where $g(x)$ is related to $(\partial v_x/\partial x)$ and $h(y)$ is related to $(\partial v_y/\partial y)$. The parameters σ_x and σ_y correspond to the artificial PML attenuation factor respectively applied following the x and y directions. After rearrangement, equations (2.35) lead to the following propagation system:

$$\frac{\partial^2 g}{\partial t^2} - c_0^2 \frac{\partial^2 p}{\partial x^2} + 2\sigma_x \frac{\partial g}{\partial t} + \sigma_x^2 \, g = 0, \tag{2.36a}$$

$$\frac{\partial^2 h}{\partial t^2} - c_0^2 \frac{\partial^2 p}{\partial y^2} + 2\sigma_y \frac{\partial h}{\partial t} + \sigma_y^2 \, h = 0. \tag{2.36b}$$

The PML theory results in wave equations and solutions that are attenuated in the direction normal to the interface boundary. Therefore, a PML should be calculated regarding the preponderant acoustic wave direction. For example, if acoustic waves propagate more likely along x-axis, then the PML should be normal to x-axis, which induces $\sigma_y = 0$ in equations (2.35) or (2.36).

Assuming that $\sigma = \sigma_x = \sigma_y$, equations (2.36) can be rewritten into an unsplit form as follows:

$$\frac{\partial^2 p(x,y,t)}{\partial t^2} - c_0^2 \left(\frac{\partial^2 p(x,y,t)}{\partial x^2} + \frac{\partial^2 p(x,y,t)}{\partial y^2} \right) + 2\sigma \frac{\partial p(x,y,t)}{\partial t} + \sigma^2 p(x,y,t) = 0, \tag{2.37}$$

where the pressure p and the acoustic velocity v are unsplited. Equation (2.37) is named as the unsplit PML wave equation.

2.2.3.2 Coordinate stretching approach

The coordinate stretching approach is another theoretical way of describing the perfectly matched layer. It can be seen as equivalent to the split-field formulation under

certain assumptions. However, this gives more insight into the analytical mechanism of the PML. It has been first defined for electromagnetism by Chew *et al.* [119]. As described by Johnson [118], coordinate stretching gives the principle of PML through three main steps: the analytic continuation, the coordinate transformation and the truncation of the domain.

Analytic continuation

The analytic continuation is based on the evaluation of the wave equation solution along an axis that is considered as infinite. Inside the PML, the solution of the wave equation is exponentially decaying (Figure 2.10), *i.e.* the solution along x-axis is multiplied by $e^{-k\Im(x)}$, where k is the wave number and $\Im(x)$ is the imaginary part of x (*i.e.* $x = \Re(x) + j\Im(x)$). As shown by figure 2.10, the harmonic wave propagat-

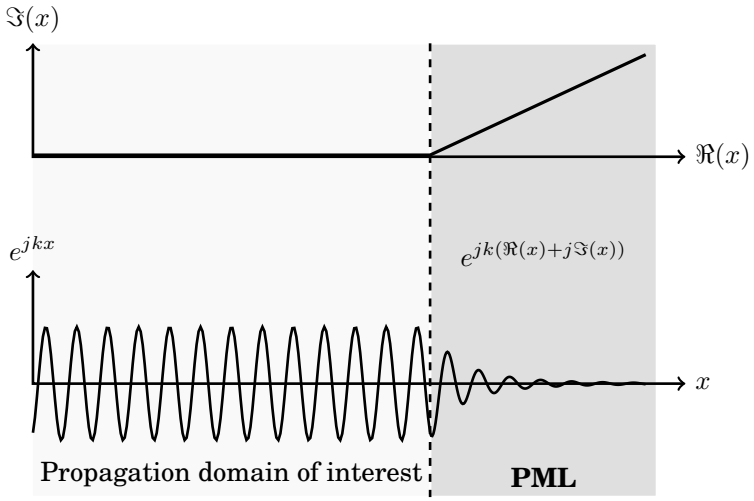

Figure 2.10: *Plot of the signal contour (top) and schematic representation of an harmonic wave propagating along the x-axis toward a PML (bottom).*

ing towards the PML decays exponentially inside the absorbing layer. Propagation inside the PML can be seen as an analytic continuation of the solution obtained in the propagation domain of interest. To solve the wave equation for the PML region, a coordinate transformation is required.

Coordinate transformation

The continuation of the analytic solution inside the PML region induces a deformation of the contour along the imaginary $\Im(x)$-axis (Figure 2.10). The variable is denoted by $x = \Re(x) + jf(x)$, where $\Im(x) = f(x)$ is the deformation function of the contour inside the PML. It is convenient to set $\partial f/\partial x = \sigma_x(x)/\omega$, where $\sigma_x(x)$ is the PML attenuation coefficient. Finally, the change of variable is equivalent to the

following transformation of the spatial derivative in the frequency domain:

$$\frac{\partial}{\partial x} \longrightarrow \frac{1}{1+j\frac{\sigma_x(x)}{\omega}}\frac{\partial}{\partial x}\,, \tag{2.38}$$

where ω is the angular frequency. The term $1/\omega$ means that all wavelengths decay at the same rate.

Truncation of the domain

Theoretically, the PML can be defined as thin as possible if a very large σ_x is considered. This is not true when the propagation domain is discretized. Unwanted reflections can be numerically observed coming from the discontinuity caused by implementation of the PML. In this case, it is possible to define an optimal shape for the function σ_x inside the PML.

Derivation of 2D PML with coordinate stretching

Starting from the mass continuity and the momentum equations, the relation between particle celerities (v_x, v_y) and acoustic pressure $(p = g(x) + h(y))$, assuming harmonic regime and a time dependence $e^{-j\omega t}$, can be written as:

$$\frac{\partial p}{\partial t} = -\rho c_0^2\left(\frac{\partial v_x}{\partial x}+\frac{\partial v_y}{\partial y}\right) = -\jmath\omega p, \tag{2.39a}$$

$$\frac{\partial v_x}{\partial t} = -\frac{1}{\rho}\frac{\partial p}{\partial x} = -\jmath\omega v_x, \tag{2.39b}$$

$$\frac{\partial v_y}{\partial t} = -\frac{1}{\rho}\frac{\partial p}{\partial y} = -\jmath\omega v_y. \tag{2.39c}$$

Equations (2.39) are transformed *via* the equation (2.38) and rewritten as:

$$-\rho c_0^2\left(\frac{\partial v_x}{\partial x}+\frac{\partial v_y}{\partial y}\left(1+\frac{\sigma_x}{\omega}\right)\right) = -\jmath\omega p + \sigma_x p, \tag{2.40a}$$

$$-\frac{1}{\rho}\frac{\partial p}{\partial x} = -\jmath\omega v_x + \sigma_x v_x, \tag{2.40b}$$

$$-\frac{1}{\rho}\frac{\partial p}{\partial y} = -\jmath\omega v_y. \tag{2.40c}$$

A Fourier transform is applied on this set of equations (2.40) to transform it back into time domain. Assuming that $-j\omega$ becomes a time derivative and $1/\omega$ corresponds to integration, equations (2.40) are written:

$$-\rho c_0^2\left(\frac{\partial v_x}{\partial x}+\frac{\partial v_y}{\partial y}\right) + \psi = -\jmath\omega p + \sigma_x p, \tag{2.41a}$$

$$\frac{\partial v_x}{\partial t} = -\jmath\omega v_x + \sigma_x v_x, \tag{2.41b}$$

$$\frac{\partial v_y}{\partial t} = -\frac{1}{\rho}\frac{\partial p}{\partial y}, \tag{2.41c}$$

where ψ is an auxiliary field variable, which satisfies $-j\omega\psi = \rho c_0^2 \, \partial v_y/\partial y$. This initial condition on the acoustic field is usually set at $\psi = 0$. Therefore, this set of equations (2.41) is equivalent to the split-field formulation (2.35) initially proposed by Bérenger [111].

Hence, the coordinate stretching approach is equivalent to the split-field formulation as both approaches give rise to an equivalent set of equations (2.35) and (2.41).

2.2.3.3 Definition of the PML attenuation factor

The connection between the propagation domain of interest and the PML can give rise to unwanted reflections if the transition is not adapted through the PML attenuation factor. Therefore, the PML attenuation factor is defined in order to smooth the transition between the two domains. Yuan [117] proposed to gradually increase the value of σ inside the layer from zero to a maximum value σ_{max}. Thus, in time-domain PML formulations, the PML attenuation factor can be written as:

$$\sigma_x = \sigma_{max} \left(\frac{x}{e_{\text{AL}}} \right)^{\beta}, \tag{2.42a}$$

$$\sigma_y = \sigma_{max} \left(\frac{y}{e_{\text{AL}}} \right)^{\beta}, \tag{2.42b}$$

where e_{AL} is the PML depth and β denotes the polynomial grading.

From equation (2.42), the PML attenuation factor can be calculated for the three first polynomial gradings ($\beta = 1, 2, 3$). Figure 2.11 shows the PML attenuation factor normalized to σ_{max} as a function of the absorbing layer thickness N_λ. If the total layer depth in meter is e_{AL}, then the equivalent thickness is given by $N_\lambda = e_{\text{AL}}/\lambda$.

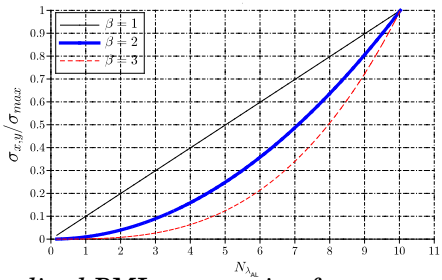

Figure 2.11: *Normalized PML attenuation factor $\sigma_{x,y}/\sigma_{max}$, as a function of the absorbing layer thickness N_λ, for three polynomial gradings.*

2.2.3.4 Conclusion

The PML theory has been derived from mass continuity and momentum equations, which gives a PML wave equation. This constitutes an elementary background that is used in the following section to derive an absorbing layer formulation for the TLM method based on the PML theory.

2.2.4 Derivation of a PML-based absorbing layer for the TLM method

This section aims at providing absorbing layers formulations for the TLM method. Based on the PML derivations presented in section 2.2.3, a method is presented to implement an approximate PML formulation for the TLM method. This approach is based on the identification of terms coming from the propagation scheme obtained from the split-field PML derivation and the TLM propagation scheme derived for acoustic wave propagation in heterogeneous and dissipative media.

2.2.4.1 PML iterative scheme

The unsplit PML wave equation propagation scheme

For the PML, the propagation scheme is derived from the discretization of the specific unsplit PML wave equation (2.37). The unsplit form has been chosen as pressure field and particle velocities in the TLM method are generally unsplit. Therefore, this form of PML equation (2.37) is more likely to be adapted to the general TLM method.

In this section, the discretization process corresponds to an approximation of the spatial and time derivatives by centered-finite differences (Eqs. (2.15)). The unsplit PML wave equation (2.37) can be rewritten using centered finite differences expansion as:

$$\begin{aligned}
&\frac{p(x,y,t+\delta t) - 2p(x,y,t) + p(x,y,t-\delta t)}{\delta t^2} \\
&- c_0^2 \left(\frac{p(x+\delta x,y,t) - 2p(x,y,t) + p(x-\delta x,y,t)}{\delta x^2} + \frac{p(x,y+\delta y,t) - 2p(x,y,t) + p(x,y-\delta y,t)}{\delta y^2} \right) \\
&+ 2\sigma \, \frac{p(x,y,t+\delta t) - p(x,y,t-\delta t)}{2\delta t} + \sigma^2 p(x,y,t) = 0.
\end{aligned} \tag{2.43}$$

The acoustic pressure can be expressed for a regular lattice where $\delta x = \delta y = \delta l$, and where continuous coordinate positions (x, y) become the discrete TLM node location (i, j). Therefore, the discretized acoustic pressure at time t and at node (i, j) is written ${}_t p_{(i,j)}$. For such a transmission-line network, the celerity between two successive nodes is given by $c = \delta l/\delta t$ at the microscopic scale. At macroscopic scale, the TLM celerity over the network c_{TLM} is set as equal to the physical celerity $c_0 = c_{\text{TLM}}$. In order to take into account oblique incidence for acoustic wave propagation inside a rectangular mesh, the celerity is corrected as $c_0 = \sqrt{2}\, c = \sqrt{2}\, (\delta l/\delta t)$ (Section 2.1.2.5). Hence, equation (2.43) can be rewritten as:

$$\begin{aligned}
&\frac{{}_{t+\delta t}p_{(i,j)} - 2\,{}_t p_{(i,j)} + {}_{t-\delta t}p_{(i,j)}}{\delta t^2} \\
&- \frac{1}{2}\frac{\delta l^2}{\delta t^2} \left(\frac{{}_t p_{(i+1,j)} - 2\,{}_t p_{(i,j)} + {}_t p_{(i-1,j)}}{\delta l^2} + \frac{{}_t p_{(i,j+1)} - 2\,{}_t p_{(i,j)} + {}_t p_{(i,j-1)}}{\delta l^2} \right) \\
&+ 2\sigma \left(\frac{{}_{t+\delta t}p_{(i,j)} - {}_{t-\delta t}p_{(i,j)}}{2\delta t} \right) + \sigma^2 \, {}_t p_{(i,j)} = 0,
\end{aligned} \tag{2.44}$$

which becomes the following discretized propagation scheme:

$$
\begin{aligned}
{}_{t+\delta t}p_{(i,j)} = & \frac{1}{2}\frac{1}{(1+\sigma\delta t)}\left[{}_{t}p_{(i+1,j)} + {}_{t}p_{(i-1,j)} + {}_{t}p_{(i,j+1)} + {}_{t}p_{(i,j-1)} - 2\sigma^2\delta t^2\ {}_{t}p_{(i,j)}\right] \\
& - \frac{1-\sigma\delta t}{1+\sigma\delta t}\ {}_{t-\delta t}p_{(i,j)}.
\end{aligned}
\tag{2.45}
$$

TLM propagation scheme for heterogeneous and dissipative media

For the TLM method, a propagation scheme can be derived using the method proposed by Hofmann and Heutschi [45] (Section 2.1.2.4). For acoustic wave propagation in heterogeneous and dissipative media, the TLM propagation scheme is given by equation (2.14), where both η and ζ depend on the node location (i,j):

$$
\begin{aligned}
{}_{t+\delta t}p_{(i,j)} = & \frac{2}{\eta_{(i,j)}+\zeta_{(i,j)}+4}\left[{}_{t}p_{(i+1,j)} + {}_{t}p_{(i-1,j)} + {}_{t}p_{(i,j+1)} + {}_{t}p_{(i,j-1)} + \eta_{(i,j)}\ {}_{t}p_{(i,j)}\right] \\
& - \frac{\eta_{(i,j)}-\zeta_{(i,j)}+4}{\eta_{(i,j)}+\zeta_{(i,j)}+4}\ {}_{t-\delta t}p_{(i,j)}.
\end{aligned}
$$

This propagation scheme presents significant similarities with the unsplit PML wave equation propagation scheme (2.45). Therefore, the next section presents an approach for the adaptation of this absorbing layer to the TLM method.

2.2.4.2 Adaptation of the PML to the TLM method

The propagation schemes (2.45) and (2.14) can be compared and each factor can be identified from one equation to the other. From this identification, a system of three linear equations with two unknown variables η and ζ, can be written:

$$
\frac{2}{\eta+\zeta+4} = \frac{1}{2}\frac{1}{1+\sigma\delta t}, \tag{2.46a}
$$

$$
\frac{2\eta}{\eta+\zeta+4} = -\frac{\sigma^2\delta t^2}{1+\sigma\delta t}, \tag{2.46b}
$$

$$
\frac{\eta-\zeta+4}{\eta+\zeta+4} = \frac{1-\sigma\delta t}{1+\sigma\delta t}. \tag{2.46c}
$$

In order to simplify the notation used in this section, the indexes (i,j) are not written, keeping in mind that each variable η, ζ and σ may depend on the node location (i,j) in the TLM model.

The system (2.46) is overdetermined for the two unknown variables η and ζ, *i.e.* there is no solution that satisfies all the three equations 2.46 simultaneously. This means that no exact implementation of a PML can be found using this approach. However, approximate formulations can be derived by considering separately the combinations of equations (2.46a) and (2.46b), (2.46b) and (2.46c) or (2.46a) and (2.46c). The three combinations of equations give rise to three independent sets of solutions for η and ζ, which are written as:

$$
\begin{cases} \eta = -2\sigma^2\delta t^2 \\ \zeta = 4\sigma\delta t + 2\sigma^2\delta t^2 \end{cases}, \tag{2.47a}
$$

$$\begin{cases} \eta &= -4\sigma^2\delta t^2/(2+\sigma^2\delta t^2) \\ \zeta &= 8\sigma\delta t/(2+\sigma^2\delta t^2) \end{cases}, \tag{2.47b}$$

$$\begin{cases} \eta &= 0 \\ \zeta &= 4\sigma\delta t \end{cases}. \tag{2.47c}$$

If σ is chosen so that $\sigma^2\Delta t^2 << \sigma\Delta t$, which is true in most cases, then solutions (2.47a) and (2.47b) become similar. The difference between these two solutions has been numerically evaluated. The results are presented and discussed in section 2.2.5.5. Hence, only two solutions remain and give the two possible formulations of an approximated PML for the TLM method in acoustics with the two absorbing matched layers (AML) noted $\mathrm{AML}_{\zeta,\eta}$ and AML_{ζ} defined by:

$$\mathrm{AML}_{\eta,\zeta} \quad \begin{cases} \eta &= -2\sigma^2\delta t^2 \\ \zeta &= 4\sigma\delta t \end{cases}, \tag{2.48}$$

and

$$\mathrm{AML}_{\zeta} \quad \begin{cases} \eta &= 0 \\ \zeta &= 4\sigma\delta t \end{cases}. \tag{2.49}$$

2.2.4.3 Discussion

Distinction between the two proposed formulations and the existing absorbing layers

The two proposed formulations $\mathrm{AML}_{\eta,\zeta}$ and AML_{ζ} are mainly related to the TLM scattering matrix of equation (2.5). The additional connexion law introduced by η is equivalent to a continuity relation between incident and scattered pulses (Equation (2.10e)). In this sense, it is important to distinguish the proposed formulations that act mostly on the scattering process of the TLM modeling from the De Cogan's or the Guillaume's approaches [110, 113] (Section 2.2.2.2) that are related to the connexion laws, *i.e.* the transmission process.

Distinction between the two proposed formulations

The two absorbing matched layers describe two artificial media that are physically different: $\mathrm{AML}_{\eta,\zeta}$ accounts for a medium that is both heterogeneous and dissipative, whereas AML_{ζ} accounts for a medium that is purely dissipative. This distinction is taken into account in the TLM method when computing the scattering matrix (Equation (2.5)).

The purely dissipative formulations and the lossy wave equation

It is interesting to note that the purely dissipative solution AML_{ζ} can also be obtained from a first order discretization of the lossy wave equation [120] written as:

$$\frac{\partial^2 p(x,y,t)}{\partial t^2} - c_0^2\left(\frac{\partial^2 p(x,y,t)}{\partial x^2} + \frac{\partial^2 p(x,y,t)}{\partial y^2}\right) + 2\sigma\frac{\partial p(x,y,t)}{\partial t} = 0, \tag{2.50}$$

which gives a propagation scheme similar to equation (2.14) if the solution (2.49) is applied:

$$
\begin{aligned}
{}_{t+\delta t}p_{(i,j)} =& \frac{2}{\zeta_{(i,j)}+4}\left[\ {}_{t}p_{(i+1,j)} + \ {}_{t}p_{(i-1,j)} + \ {}_{t}p_{(i,j+1)} + \ {}_{t}p_{(i,j-1)}\right] \\
&- \frac{4-\zeta_{(i,j)}}{4+\zeta_{(i,j)}}\ {}_{t-\delta t}p_{(i,j)}\ .
\end{aligned}
\tag{2.51}
$$

Therefore, the solution (2.49) can rigorously be attached to the lossy wave equation (2.50).

Absorbing layers adaptation: definition of the damping factor

Both solutions (2.48) and (2.49) rely on the damping parameter σ. It is chosen so that it gradually increases from zero for the nodes at the interface between the AML and the propagation domain to a maximum value σ_{max} for the nodes located at the computational domain limit:

$$
\sigma(d_N) = \sigma_{max}\left(\frac{d_N}{e_{\mathrm{AL}}}\right)^2, \tag{2.52}
$$

where e_{AL} is the AML thickness and d_N is the normal distance between a node N inside the AML and the interface between the AML and the propagation medium (Figure 2.13). In a first approach, it is assumed that the maximum value for the TLM dissipation term ζ is set equal to unity. From equations (2.48) and (2.49), this induces to set the maximum value of the damping factor equal to $\sigma_{\max} = 500\ \mathrm{s}^{-1}$. Therefore, in the first set of simulations the damping factor is gradually increased inside the absorbing layer from $0\ \mathrm{s}^{-1}$ at the entrance to $500\ \mathrm{s}^{-1}$ at the end, following equation (2.52). The maximum value for σ is investigated and discussed in the following results section.

2.2.5 Numerical results

The aim of the following numerical simulations is to evaluate the efficiency of a given absorbing layer directly implemented through the TLM method. The numerical simulations presented in this section are calculated using both the Scilab-TLM code and the Matlab-TLM code (Section 2.1.3).

2.2.5.1 Assessment of the absorbing layers efficiency

In order to assess the numerical efficiency of a given absorbing condition, an ideal free-field wave propagation should be defined and used as a reference. This reference free-field acoustic pressure p_{ff} can be calculated from an extended propagation domain in which the acoustic wave would not collide with any boundary during the simulation duration. Next simulations are carried out to calculate the acoustic pressure p at the same location in real conditions, *i.e.* with a propagation domain surrounded by the tested absorbing condition. The acoustic pressure p can be compared to the free-field pressure p_{ff} in order to get an objective criterion for the assessment

of the absorbing condition efficiency. Therefore, Sheu *et al.* [121] defined the mean error function to study the impact of absorbing layers on the truncated propagation domain of interest, as:

$$\mathbf{error}(x,y) = 10\log_{10}\left(\frac{\sum_{t=0}^{T}|p_{\mathrm{ff}}(x,y,t)-p(x,y,t)|^2}{\sum_{t=0}^{T}|p_{\mathrm{ff}}(x,y,t)|^2}\right). \tag{2.53}$$

The error is infinitely small when the pressure p is rigorously equal to the free-field pressure p_{ff}, and its value increases when the pressure diverges from the free-field pressure value. Overall, a low value of the reflection error index indicates a good efficiency of the AML.

2.2.5.2 Numerical settings

The signal used for numerical simulations can be seen as a Gaussian impulse with a frequency distribution centered around a specific frequency. The initial signal is a sinusoid and the peak-to-peak dynamics goes from -1 to 1. In order to obtain an equilibrium between the duration and the frequency response of the signal, the sinusoid has been windowed by a Kaiser window, where the window parameter is $\alpha = 40$. This parameter is an arbitrary non-negative real number that determines the shape of the window. The test signal $p_{\mathrm{S}}(x,y,t)$ can be written as:

$$p_{\mathrm{S}}(x,y,t) = \sin(2\pi f t) \times \mathrm{w}_{kr}(t), \tag{2.54}$$

where f is the frequency and $\mathrm{w}_{kr}(t)$ is the Kaiser's window. Figure 2.12 shows an example of a test signal for $f = 100$ Hz. The temporal windowing is used to restrict the duration of the signal and to keep a frequency response centered around the frequency of interest. From figure 2.12, it can be seen that the duration of the excitation signal is about 0.1 s with a frequency content centered around 100 Hz.

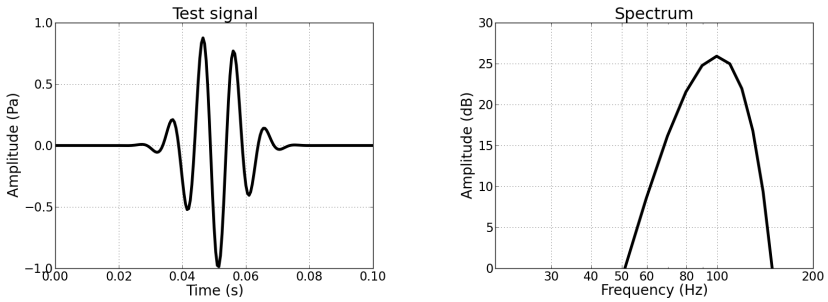

(a) (b)

Figure 2.12: *Example of the test signal (a) and its spectrum (b), for* $f = 100$ Hz.

For each simulation the number of nodes per wavelength has been set to 20 and the sound speed is $c_0 = 340$ m.s^{-1}. This induces a spatial step $\delta l = 0.17$ m, and a time step $\delta t = 5.10^{-4}$ s. In this section, the number of iterations for a simulation is set to 1000, which gives a total simulation duration of $t_{\mathrm{sim}} = 0.5$ s.

2.2.5.3 Geometrical configuration of the computation domain

All simulations presented in this section are calculated using two-dimensional (2D) computational domains as depicted in figure 2.13. The absorbing layer computation domain (Figure 2.13(a)) is made up of two sub-domains: the propagation domain D_0 and the absorbing layer domain D_1. It is important to distinguish the propagation domain D_0, where the diffusion matrix is set to simulate acoustic wave propagation in an homogeneous and non-dissipative medium, and the absorbing layer domain D_1, where the tested AML formulation is implemented. The separation of the computational domain into two sub-domains is defined in order to work on two independent scattering matrices. This appears to be a convenient method to test each AML formulation keeping the same geometrical set-up. The free field computation domain (Figure 2.13(b)) required for the calculation of the error level is calculated using a double sized domain D_0 (90 m $\times$ 70 m) with no absorbing layer. The four outer boundaries encompassing the whole computational domain are perfectly reflecting. A point source is located on the plane $y = 0$, in order to artificially extend the domain to a semi-infinite domain, and at a distance $d_S = 10$ m from the AML. The mean error function is evaluated inside a test area (10 m $\times$ 54 m) located in the D_0 domain between the source and the AML. The assessment of the absorbing layer is given for a large range of incident angles ($0° \leq \theta \leq 70°$), thanks to the large size of the test area.

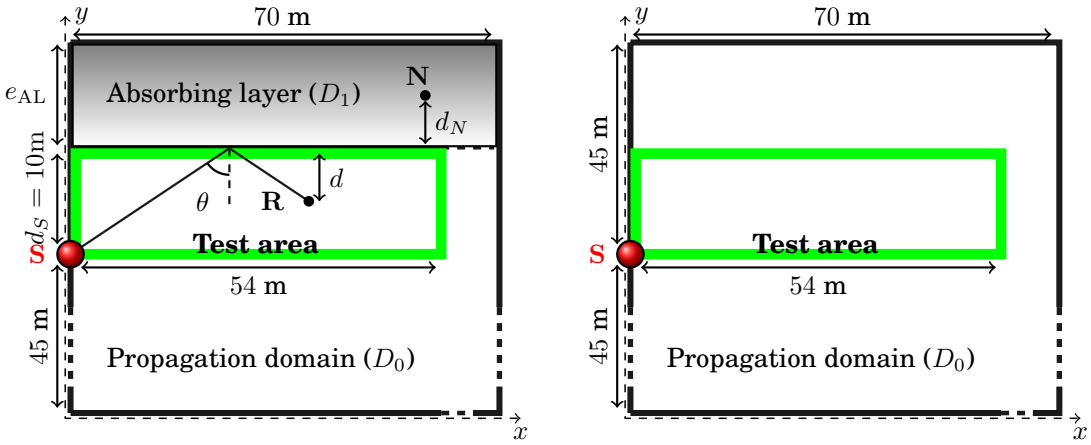

(a) Absorbing layer computation domain (b) Free field computation domain

Figure 2.13: *Computational domains used to assess the efficiency of an absorbing layer (D_1) inside the test area (green rectangle):* (a) *with absorbing layer,* (b) *free field.*

2.2.5.4 Calculation process for each absorbing layer

Numerical simulations are carried out in two steps. Firstly, the size of propagation domain D_0 is doubled (90 m $\times$ 70 m) and no absorbing layer is computed in order

to simulate a free-field propagation during the simulation time $t_{\mathrm{sim}} = 0.5$ s. The free-field acoustic pressure p_{ff} obtained from this so-called free-field domain is used as a reference. Secondly, the free-field domain is replaced by the domain shown in figure 2.13(a), where the absorbing layer D_1 is computed. It is important to note that the pressure is calculated at the same locations, *i.e.* inside the test area for every simulation. Therefore, the pressure obtained for each absorbing layer can be compared to the free-field pressure. This comparison is used to assess the efficiency of the absorbing layer through the calculation of the mean error function level defined in section 2.2.5.1.

2.2.5.5 Results and discussion

This section aims at comparing the efficiencies of the two proposed absorbing layers $\mathrm{AML}_{\eta,\zeta}$ and AML_{ζ} with the "one-way" matched connection law proposed by Guillaume [113] (Section 2.2.2.2), using the parameter $\epsilon = 10^{-5}$ for the one-way approach.

Verification of the equivalence between the two solutions (2.47a) and (2.47b)

The differences between the solutions (2.47a) and (2.47b) are numerically calculated. Figure 2.14 shows the difference between the two solutions calculated over all the test area surface. The absolute frequency is the number of times a particular values of the difference level is observed inside the test area. It is shown that most of the difference are constrained between the levels 0.06 and 0.10, and the differences levels do not exceed 0.5 dB at 100 Hz. Therefore, the solutions (2.47a)

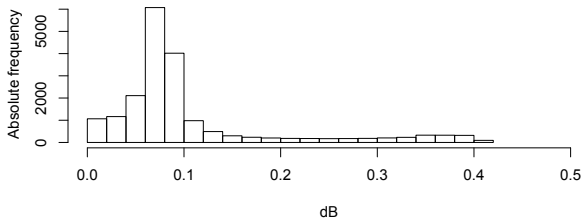

Figure 2.14: *Absolute frequency (i.e. the number of times a particular values of the difference is observed inside the test area) of the error difference levels between the solutions* (2.47a) *and* (2.47b) *inside the test area. AML thickness* $N_{\lambda_{\mathrm{AL}}} = 2$*,* $\sigma_{\max} = 500\ \mathrm{s}^{-1}$*,* $f = 100$ Hz.

and (2.47b) can be seen as numerically equivalent. Therefore, the following simulations focused on the comparison of the two proposed $\mathrm{AML}_{\eta,\zeta}$ and AML_{ζ}, with the one-way approach.

Overview of the mean error levels

In this section, the mean error levels as a function of space are presented for two test signals centered respectively at the frequencies 100 Hz and 300 Hz. For each calculation, the absorbing layer thickness is set equal to two wavelengths at 100 Hz, $N_{\lambda_{\mathrm{AL}}} = 2$, *i.e.* $e_{\mathrm{AL}} = 3.4\ \mathrm{m} \equiv 20\ \mathrm{nodes}$. From a general point of view, the mean error levels inside the test area gives a global idea of each AML efficiency. Figures 2.15 and 2.16 show the spatial distribution of the mean error levels for signal frequencies respectively centered around 100 Hz and 300 Hz.

At 100 Hz (Figure 2.15), it can be seen that the proposed formulation AML_{ζ} (Figure 2.15(a)) performs slightly better than the empirical one-way approach (Figure 2.15(c)). The $\mathrm{AML}_{\eta,\zeta}$ (Figure 2.15(b)) for small incidence angles shows mean error levels that would be the result of reflections caused by a discontinuity at the boundary between the propagation domain and the absorbing layer. As expected, the mean error level increases with the increase in the incident angle; this aspect is detailed in the following sections. However, it can be noticed that at a minimum distance $d = 4\ \mathrm{m}$ from the absorbing layer, the mean error levels for small incidence angles are below $-30\ \mathrm{dB}$, which ensures significant attenuation for each formulation.

Mean error level at 100 Hz

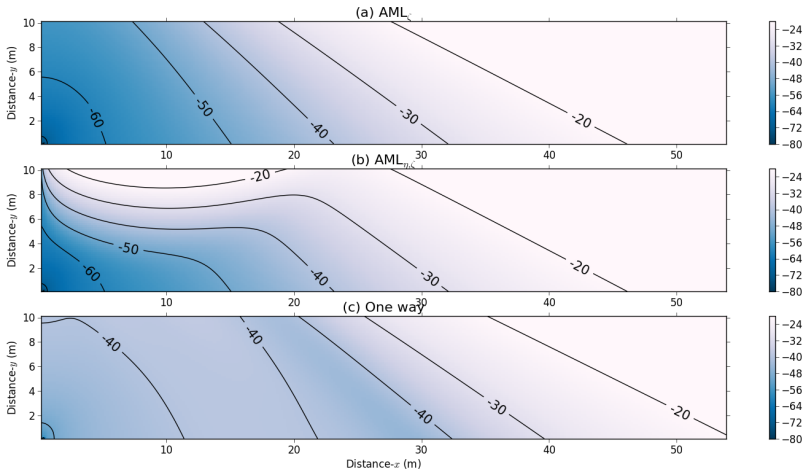

Figure 2.15: *Mean error function level* (dB) *inside the test area for a test signal centered at* 100 Hz *and an absorbing layer thickness* $N_{\lambda_{\mathrm{AL}}} = 2$*:* (a) AML_{ζ}*;* (b) $\mathrm{AML}_{\eta,\zeta}$*;* (c) *One-way*.

At 300 Hz (Figure 2.16), the mean error levels appear to be simply transposed to lower levels and the same global shapes for the contour lines. However, for small incident angles, it can be seen that lower levels are reached with the one-way approach compared to the two AML_{ζ} and $\mathrm{AML}_{\eta,\zeta}$.

The mean error level representation as a function of space gives an interesting overview of the ability for a given approach to absorb incoming waves. However, in order to focus on the frequency, incident angles or layer thickness, it is more suitable to focus on few interesting key points located inside the test area. Therefore, in

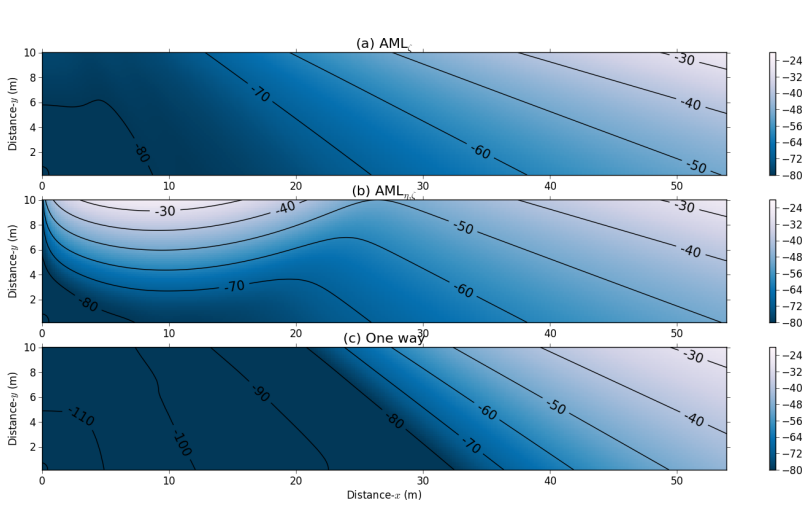

Figure 2.16: *Mean error function level (*dB*) inside the test area for a test signal centered at* 300 Hz *and an absorbing layer thickness* $N_{\lambda_{\mathrm{AL}}} = 2$*:* (a) AML$_\zeta$*;* (b) AML$_{\eta,\zeta}$*;* (c) *One-way*.

the following sections, specific locations are selected and described to focus on the influence of the frequency, incident angles or layer thickness on the error levels for each AML approach.

The mean error level as a function of frequency

Figure 2.17 shows the mean error levels as a function of frequency from 40 Hz to 600 Hz at six given points taken inside the test area. Three points are along the x-axis at the bottom of the test area ($d/d_s = 1.0$), and the three others are aligned in the middle of the test area ($d/d_s = 0.5$). Each point location along the x-axis corresponds to the incidence angles: $0°$, $35°$ and $70°$. At 10 meters from the layer ($d/d_s = 1.0$), the two proposed AML formulations show the same error levels along frequency for all incident angles. However, for smaller distance ($d/d_s = 0.5$), as observed on figures 2.15(b) and 2.16(b), the AML$_{\eta,\zeta}$ formulation shows higher error levels than the AML$_\zeta$ at $35°$. This is caused by the strong reflection (high error level), at the boundary of the test area for small incident angles, observed with the AML$_{\eta,\zeta}$ formulation in the previous section. It can be seen that for low incident angles ($0°$ to $35°$), the two proposed AML perform slightly better below 200 Hz than the one-way approach for both distances. At higher frequencies, the error level of the proposed AML formulations converges towards an almost constant value, that depends on the angle. Above 300 Hz, the one-way approach gives lower error levels when increasing the frequency. For near grazing incidence angle ($70°$), the difference between the two approaches is reduced for frequencies below 300 Hz; this is illustrated by the similarity of the contour lines orientation in figures 2.15 and 2.16 at large incident angles. It can be observed for the AML$_\zeta$ and for the one-way approach that the receiver distance from the absorbing layers ($d/d_s = 1.0$ or 0.5)

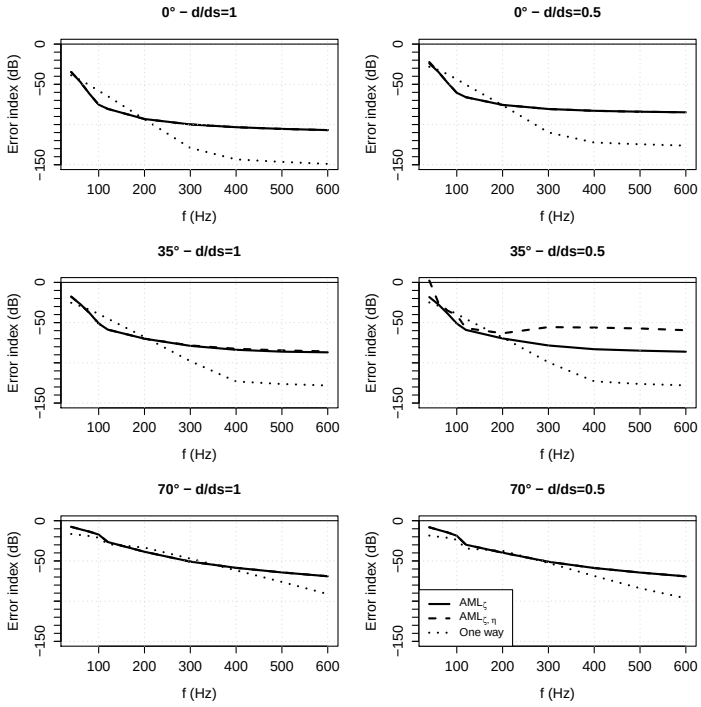

Figure 2.17: *Mean error function level (*dB*) as function of frequency: comparison between methods for three incidence angles (*$0°$*: normal incidence,* $35°$*: oblique incidence,* $70°$*: grazing incidence) and two distances from the* AML.

does not influence the global trends shown for the error level at each incident angle. In other words, at this frequency the error levels depend more on the incident angle value, *i.e.* the location along the x-axis, than on the location along the y-axis. The next section gives more insight on the angular dependence of the error level.

The mean error level as a function of the incident angle

In figure 2.18, the influence of the incident angle on the error levels are shown for three given frequencies: 40 Hz; 300 Hz and 600 Hz. At the distance $d/d_s = 1.0$, each approach shows lower error levels for small incident angles than grazing angles. For the distance $d/d_s = 0.5$, the $\text{AML}_{\eta,\zeta}$ differs from the AML_{ζ} and shows higher error levels from $5°$ to $60°$. This corresponds to the zone identified in figures 2.15(b) and 2.16(b) where significant reflections are obtained with the $\text{AML}_{\eta,\zeta}$ formulation.

The mean error level as a function of the layer thickness

The influence of the absorbing layer thickness for each approach at the frequency $f = 100$ Hz is presented in figure 2.19 for three incident angles: $0°$, $35°$ and $70°$. As expected, the error level decreases when the layer thickness increases. It should be noticed that very low error levels, such as for example -75 dB for normal incidence, are reachable with only $N_{\lambda_{\text{AL}}} = 2$ for both proposed AMLs. Generally speaking, sig-

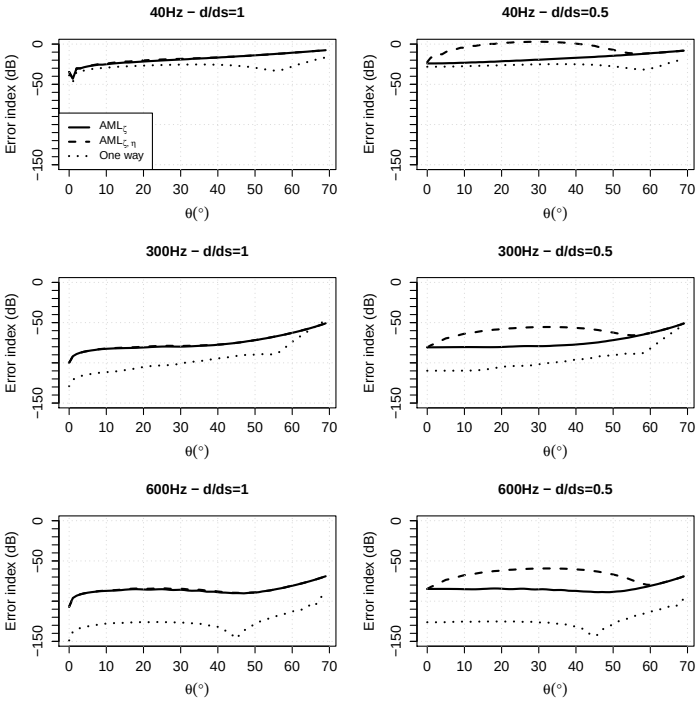

Figure 2.18: *Mean error function level (*dB*) as function of the incident angle, from normal (*0°*) to grazing (*70°*) incidence: comparison between methods for three frequencies (*$40\ \mathrm{Hz}, 300\ \mathrm{Hz}, 600\ \mathrm{Hz}$*) and two distances from the* AML *(left* $d/d_s = 1$*; right* $d/d_s = 0.5$*).*

nificant attenuations are achieved with small layer thickness for normal and oblique incident angles with the three approaches. Moreover, at this distance ($d/d_s = 1$) the proposed formulations AML$_{\eta,\zeta}$ and AML$_\zeta$ show lower error levels, from $N_{\lambda_{\mathrm{AL}}} = 1$ to 4 for normal and oblique incident angles, than the one-way approach.

2.2.5.6 Optimization of the proposed AML

As a general observation, it can be noticed that the formulation AML$_{\eta,\zeta}$ always performs worse than the AML$_\zeta$. Therefore, it is suggested to work with the purely dissipative approach AML$_\zeta$, rather than with the AML$_{\eta,\zeta}$.

As stated in section 2.2.4.3, the maximum value for the damping factor $\sigma_{\max}$ is set as a function of the TLM parameter ζ as equal to $\sigma_{\max} = 500\ \mathrm{s}^{-1}$.

The following investigation shows that keeping the same gradual increase with lower values for $\sigma_{\max}$ can improve the properties of the proposed formulation AML$_\zeta$. Figure 2.20 shows the error level for the AML$_\zeta$ at 100 Hz for two values of $\sigma_{\max}$. It is first shown for $\sigma_{\max} = 200\ \mathrm{s}^{-1}$ that lower error levels are reached compared to the case with $\sigma_{\max} = 500\ \mathrm{s}^{-1}$ (Figure 2.15(a)). The area in which lowest error level (< 40 dB) is extended to larger incident angles. Furthermore, decreasing the value of $\sigma_{\max}$ to $50\ \mathrm{s}^{-1}$ (Figure 2.20(b)), the error level for large incident angles is decreased, whereas, the error level at normal incidence is slightly increased. This

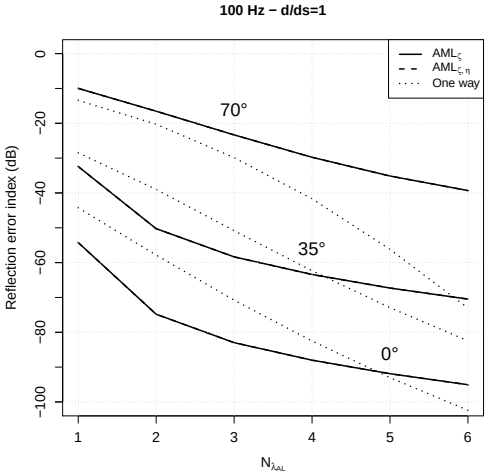

Figure 2.19: *Mean error function level (dB) as function of the absorbing layer thickness* $N_{\lambda_{\mathrm{AL}}}$ *at the frequency* $f = 100$ Hz *for three incident angles (in these cases,* AML_ζ *and* $\mathrm{AML}_{\zeta,\eta}$ *are overlapped).*

shows that a balance can be found at this frequency using an intermediate value of $\sigma_{\max}$.

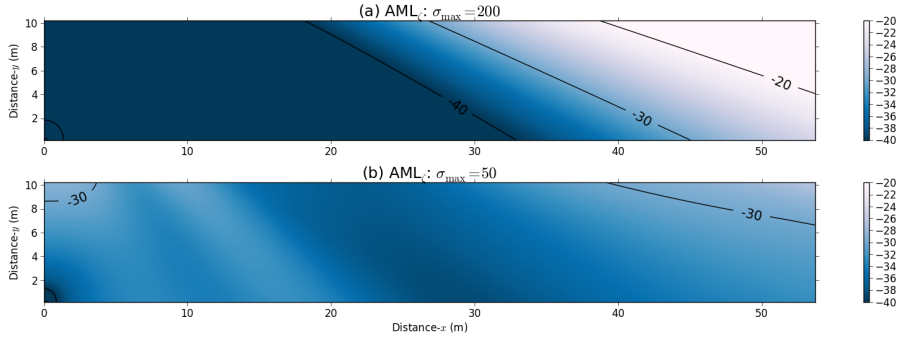

Figure 2.20: *Mean error function level (*dB*) inside the test area for two values of* $\sigma_{\max}$*, using the* AML_ζ *with a test signal centered at* 100 Hz *and an absorbing layer thickness* $N_{\lambda_{\mathrm{AL}}} = 2$*:* (a) $\sigma_{\max} = 200\ \mathrm{s}^{-1}$ *;* (b) $\sigma_{\max} = 50\ \mathrm{s}^{-1}$.

As the efficiency of an AML is also relative to its thickness, the following results show the mean error levels for the AML_ζ when the thickness is reduced to $N_{\lambda_{\mathrm{AL}}} = 1$, relatively to the frequency 100 Hz, *i.e.* $e_{\mathrm{AL}} = 3.4$ m. In this case, the maximum value of the damping factor has been empirically set equal to $\sigma_{\max} = 150\ \mathrm{s}^{-1}$. As shown in figure 2.21, it is interesting to note that for such a thin layer, error levels lower than -25 dB are reachable for a wide span of incident angles (larger than $50°$).

The previous investigations demonstrate that the absorbing layer thickness can be reduced and an optimized value of $\sigma_{\max}$ can be found to achieve a homogeneous low mean error level over a large surface of the test area. In addition, figure 2.22

(a) Error level inside the test area

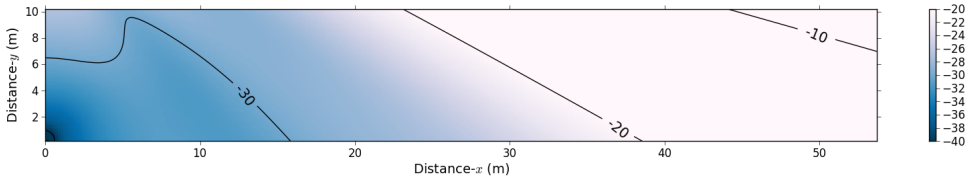

(b) Error level as a function of the incident angle

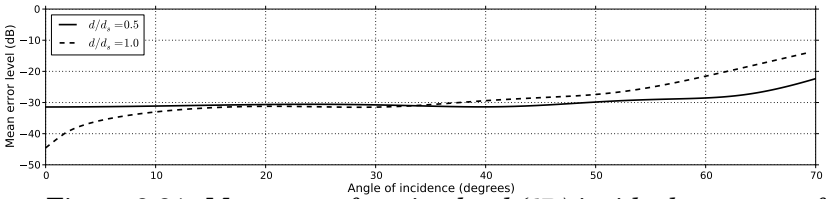

Figure 2.21: *Mean error function level (*dB*) inside the test area for* $\sigma_{\max} = 150\ \mathrm{s}^{-1}$ *using the* AML_ζ *and a test signal centered at* 100 Hz *and an absorbing layer thickness* $N_{\lambda_{\mathrm{AL}}} = 1$*: (*a*) in the test area; (*b*) as a function of the incident angle.*

shows the error level as a function of the damping factor $\sigma_{\max}$ for seven incident angles and at two distances from the absorbing layer $d/d_s = 1.0$ and $d/d_s = 0.5$. In this case, the absorbing layer thickness is reduced to $N_{\lambda_{\mathrm{AL}}} = 1$ in order to test the damping factor dependency in critical conditions.

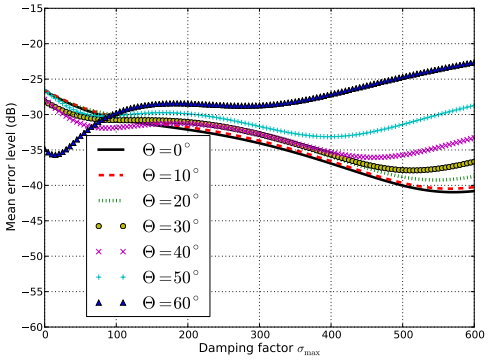

(a) $d/d_s = 0.5$

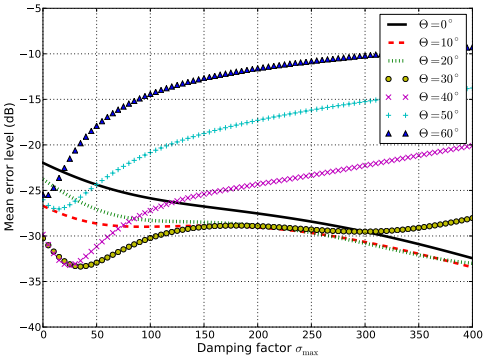

(b) $d/d_s = 1.0$

Figure 2.22: *Mean error function level (*dB*) inside the test area for seven incident angles as a function of the damping factor* $\sigma_{\max}$ *for* $f = 100$ Hz *and* $N_{\lambda_{\mathrm{AL}}} = 1$ *at the distances:* (a) $d/d_s = 1.0$*;* (b) $d/d_s = 0.5$*.*

The results obtained at $d/d_s = 1.0$ show that for the first incident angles (*i.e.* below $40°$), an increase in $\sigma_{\max}$ leads to lower error levels, whereas above $40°$, the lowest error levels are obtained when $\sigma_{\max} = 20\ \mathrm{s}^{-1}$. The trade-off over all incident

angles is achieved for $\sigma_{\max} \in [40; 80]$ s^{-1}. This range ensures an error level inferior to -30 dB for the maximum of incident angles at both $d/d_s = 1.0$ and $d/d_s = 0.5$.

In practice, depending on the geometry of the numerical domain, three cases can be extracted, where each case has its own optimized $\sigma_{\max}$ value. Firstly, for the case where normal incident angles are dominant, such as in urban areas, for instance $\sigma_{\max} = 380$ s^{-1} would be advised. Secondly, for the case where grazing incident angles are dominant such as in long range outdoor sound propagation, for instance $\sigma_{\max} = 20$ s^{-1} would be the optimum. Thirdly, if the numerical domain presents a mix between the two previous cases, then $\sigma_{\max} \in [40; 80]$ s^{-1} would represent the best balance.

2.2.6 Conclusion on the AML formulations

Two absorbing matched layer formulations (AML$_{\eta,\zeta}$ and AML$_{\zeta}$) have been proposed for the implementation of an approximate perfectly matched layer (PML) for the transmission-line matrix (TLM) method in acoustics. The two AML formulations are based on the identification between the TLM heterogeneity and dissipation terms, and the PML attenuation factor. It is important to note that the two proposed AML formulations are not based on empirical approaches, but on rigorous derivation of the PML theory originally introduced by Bérenger [111] for electromagnetism. However, the resulting AML formulations are only equivalent to approximate PML as the derivation presented here does not lead to a straightforward solution. The AML$_{\eta,\zeta}$ is equivalent to an heterogeneous and dissipative medium, and the AML$_{\zeta}$ corresponds to a purely dissipative medium. This AML$_{\zeta}$ formulation has rigorously been linked to the lossy wave equation. Both formulations act mainly on the scattering matrix, whereas the existing absorbing layers such as the one-way deal with the connexion laws.

The proposed AML formulations have been compared to the empirical one-way approach proposed by Guillaume [113]. Numerical results are based on the calculation of the mean error level, which gives the efficiency of an absorbing layer in terms of reflection error induced by the truncation of the propagation domain of interest. From the representation of the error level inside a large test area for two frequencies, it has been observed that the two AML formulations are both frequency and spatially dependent. Although the AML$_{\zeta}$) efficiency is slightly better than the one-way approach below 200 Hz, from 300 Hz the empirical one-way approach performs better at each position. When looking at the angular dependency of the error level, it is shown that the one-way approach performs better than the two proposed formulations. From the study of the layer thickness, it is observed that significantly low error levels are reached from a layer width that is about 2 wavelengths thick at 100 Hz, for the three tested incident angles. As an important contribution, it can be noticed that for small layer widths, the proposed AML formulations are more efficient for normal and oblique incident angles than the one-way approach. However, this is not verified at grazing incidence. This can be seen as an interesting feature, as the major goal is to propose thin efficient absorbing layers in order to reduce the computational cost. Most importantly, it is shown at the end of this chapter that the most efficient proposed formulation (AML$_{\zeta}$), can be optimized from the damp-

ing factor maximum value. The optimization of the $\sigma_{\max}$ value at a given frequency leads to acceptable error level for a wide incident angle span.

2.3 Conclusion

The TLM method has been introduced in the first part of this chapter to give the general background related to this numerical method. Although the TLM method is often presented as an empirical approach for the simulation of wave propagation, it has been rigorously related to the classical acoustic wave equation. The presentation of the TLM method is oriented here to give a global idea of the numerical mechanism and, more importantly, to remind that the TLM method can be derived from acoustic wave equation using classical iterative schemes.

From the literature review on the absorbing conditions, it has been observed that absorbing layer approaches were the most interesting perspective to simulate an infinite domain from truncated boundaries. Furthermore, it has been noted that the perfectly matched layer (PML) shows convincing results with other time-domain method such as FDTD. However, no rigorous implementation of this theory has been yet proposed for the TLM method in acoustics. Thus, through the identification of the PML attenuation factor and the TLM heterogeneous and dissipative terms, two absorbing matched layer formulations have been tested and compared to the empirical Guillaume's one-way approach [113].

The AML_ζ formulation has been identified as a convincing theoretical approach for the implementation of absorbing layers in the TLM method for acoustics. In this sense, the optimization of this formulation has shown satisfying results, and would be an interesting perspective for propagation domains with large incident angles such as in outdoor sound propagation. Moreover, this dissipative approach, first introduced by Kagawa [102] and expanded by Hofmann and Heutschi [45], has been linked here to a form of the theoretical lossy wave equation [120].

However, the proposed formulation is not exactly a PML, as the adaptation of the PML theory requires deeper investigation and more fundamental development of the TLM method. From now, the link between the TLM method and acoustics relies on a wave equation. Thus, the only variable that can be handled here is the pressure. The fundamental work that remains open consists in the expansion of the mass conservation and momentum equations for the TLM method. These equations would enable to adapt anisotropic absorbing layers using the acoustic velocity as originally written in the PML theory.

As an interesting feature, the representation of the mean error level for a given surface can be seen as an interesting approach to assess absorbing layers in term of reflection error. Using this representation, the spatial variations of the error level for each absorbing layer are shown at first sight.

As an interesting future work, the one-way approach and the AML_ζ could be combined to form an hybrid absorbing layer where both the scattering matrix and the connexion laws are used for the dissipation of the outgoing waves.

Due to lack of time, the proposed AML formulation has not been implemented neither in the Python/OpenCL-TLM code nor in the Scilab-TLM code, used for the

simulations presented in chapters 3 and 4. In the following chapters, the absorbing layers used with the TLM method are based on the one-way approach exclusively.

Chapter 3

SCATTERING OF ACOUSTIC WAVES BY CIRCULAR SCATTERERS USING THE TRANSMISSION-LINE MATRIX METHOD

3.1 Introduction

Sound waves emanating from road traffic traveling through forested areas or more generally through vegetation are going to be scattered by obstacles such as trunks, branches or leaves. It should first be noticed that scattering is frequency dependent. In other words, the scattering of acoustic waves of a given wavelength is closely related to the obstacles apparent size. Therefore, in the scattering theory, the frequency is usually introduced through the wave number $k = 2\pi f/c_0$, where c_0 is the sound speed and f is the frequency. A common way to look at the significance of acoustic scattering is to consider the factor ka, where a is the size of the scatterer. For the simplest case of single scattering (or acoustic refraction by circular scatterer, see section 3.2), the scattered pressure field becomes preponderant when the factor ka is superior or close to unity, *i.e.* $ka \sim 1$. Considering a representative road traffic noise source, it can be assumed that most part of the A-weighted acoustic energy is centered around 1000 Hz for high speed traffic (*i.e.* 90 km/h) [122] and below for low speed, where most of the acoustic emission comes from the car engine. Hence, taking 1000 Hz as the maximum frequency, the minimum obstacles diameter for the study of road traffic noise scattering is about $a \sim 10^{-2}$ m. Therefore, obstacles considered as small compared to the wavelength, such as branches, twigs or leaves, are excluded from the present scattering study. In a first approach, for the study of sound scattering through forested area, the three-dimensional forest can be reduced to an area containing cylinders that stand for the tree trunks. Furthermore, in a two-dimensional space, an area full of scatterers such as tree trunks can be reduced to an area of randomly distributed 2D circular scatterers.

Since in the literature, no article has been found about scattering by cylindrical obstacles treated by the TLM method in acoustics, it seems important to verify

the ability of the TLM method for the calculation of acoustic scattering by single or multiple circular scatterers (*i.e.* tree trunks). In this chapter, the TLM simulations of sound scattering are compared to both analytical solutions and measurements on scale models. Section 3.2 deals with scattering of an acoustic plane wave by a single scatterer. The 2D polar variation of the scattered levels obtained from the analytical solution are then compared to the TLM results for several discrete frequencies. In addition, the 3D case of a single cylinder placed normal to an impedance ground is simulated using the TLM method and is compared to both analytical solutions and experimental results on scale models. Section 3.3 presents a multiple scattering theory, which analytically describes the acoustic field transmitted through an array of a randomly distributed circular scatterers. In the 2D multiple scattering case, the TLM results are compared to analytical solutions for two densities of scatterers. Finally, TLM simulations of 3D cases are compared to measurements on scale models for two configurations of scatterers. Since the literature shows that the absorption by tree bark trunks is small (Section 1.3.2), in this chapter the trunk are assumed to be perfectly reflecting.

3.2 Simulation of single scattering using the TLM method

Sound scattering by solid cylinders and spheres has been largely analytically and numerically studied. For instance, Faran [123] studied the effect of shear waves on the surface of the scatterers. In this work, scattering patterns (*i.e.* the polar variation of the scattered field) obtained from the analytical solutions are compared to experimental data as a function of frequency. Sound scattering also depends on the characteristics of the incident wave. This has been analytically studied for spherical and cylindrical sources respectively in [64] and [124]. The simulation of scattering with time-domain numerical method, such as the finite-difference time-domain (FDTD) method, has also already been investigated, for example by Tolan *et al.* [125].

Section 3.2.1 deals first with 2D single scattering, where the TLM simulations are compared to analytical solutions. Int section 3.2.2 the 3D case of single scattering above an impedance ground is studied by the comparison of the TLM results and measurements on scale models.

3.2.1 Scattering of a plane wave by a 2D circular scatterer

Single scattering corresponds to the diffraction of an acoustic wave by an obstacle named, in this document, as scatterer. In this section, the scatterer is assumed to be circular.

Firstly, the theory of diffraction by a 2D circular scatterer is introduced through the derivation of the Helmholtz equation solutions, written in cylindrical coordinate system. Secondly, the numerical results obtained from the TLM method are compared to the analytic solutions.

3.2.1.1 Theory

The propagation of a monochromatic acoustic wave in the vicinity of an isolated scatterer can be depicted as shown in figure 3.2. A cylinder of infinite height, of a

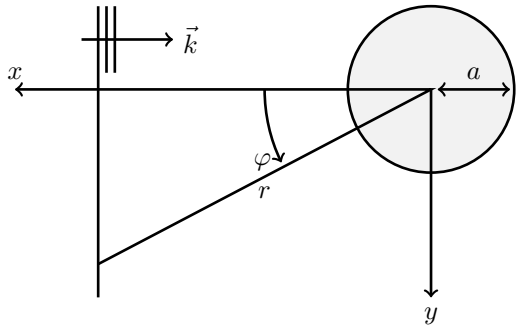

Figure 3.1: *Schematic of wave propagation in the vicinity of a cylinder.*

radius a is first considered in a cylindrical coordinate system (r, φ, z). In this case, the wave equation can be written as [61]:

$$\left[\frac{1}{r}\frac{\partial}{\partial r}\left(r\frac{\partial}{\partial r}\right) + \frac{1}{r^2}\frac{\partial^2}{\partial \varphi^2} + \frac{\partial^2}{\partial z^2} + k^2\right] p = 0, \tag{3.1}$$

where the distance r satisfies $r > a$. The incident wave is a monochromatic plane wave, which can be written as:

$$p_i = P_0 e^{\jmath kr\cos\varphi} e^{\jmath\omega t}, \tag{3.2}$$

where k is the wave number, ω the angular frequency and P_0 the amplitude of the incident wave. This plane wave can be rewritten as the sum of cylindrical waves as follows:

$$p_i = P_0 \sum_{m=0}^{\infty} (2-\delta_{m0})\jmath^m \; J_m\,(kr)\; e^{\jmath m\varphi}\; e^{\jmath\omega t}, \tag{3.3}$$

where δ_{m0} is the Dirac function and J_m is the Bessel function of the first kind for positive integer order m. The wave equation (3.1) is solved using Hankel function forms. The scattered wave is written as divergent cylindrical wave

$$p_s = P_0 \sum_{n=0}^{\infty} A_n H_n^{(1)}\,(kr)\; e^{\jmath n\varphi}\; e^{\jmath\omega t}, \tag{3.4}$$

where $H_n^{(1)}$ are the Hankel function of the first kind for positive integer order n. The coefficients A_n are derived from the boundary condition, which can be written at $r = a$:

$$\frac{\jmath}{k\rho c}\frac{\partial}{\partial r}(p_i + p_s) = \frac{-1}{Z}(p_i + p_s), \text{ for } r = a, \tag{3.5}$$

where Z is the normal acoustic impedance of the cylinder, ρ is the mass density and c the sound speed in the air. Thus, the coefficients A_n can be written as:

$$A_n = -\frac{(2-\delta_{n0})\jmath^n[\jmath J_n'(ka) + (\rho c/Z)J_n(ka)]}{\jmath H_n^{(1)'}(ka) + (\rho c/Z)H_n^{(1)}(ka)}. \tag{3.6}$$

Through this coefficient A_n, the surface impedance of the cylinder can be taken into account. The scattered pressure level relative to the incident pressure field can be defined as follows:

$$L_{\text{scat}} = 10 \log_{10} \left(\frac{p_s}{p_i} \right). \tag{3.7}$$

3.2.1.2 Numerical results for 2D single scattering

The scattering of sound has already been investigated using numerical time-domain method such as FDTD method. The following TLM simulations are inspired by the article written by Wang [126]. In this reference, the author studied the polar variations of the scattered field (also named as directivity patterns or scattering patterns). The geometry and the principle of the simulation are first detailed, and the TLM directivity patterns are compared to the analytic solutions. The numerical simulations presented in this section are exclusively calculated using the Scilab-TLM code (Section 2.1.3). In this section, the surface of the cylinder is assumed to be perfectly reflecting. Therefore, the surface impedance in the analytical formulation (Equation (3.6)) tends to infinity.

Geometry and principle

As shown in figure 3.2, the scatterer is located at the center of the computational domain and its radius is $a = 0.25$ m. The receivers are located on the circle whose radius is $r = 5$ m, centered on the scatterer. The top, bottom and left boundaries are considered as perfectly reflecting whereas the right boundary is made of an absorbing layer based on the one way approach (Section 2.2.2.2). The simulations duration is set to not exceed 0.06 s, which is short enough to avoid any unwanted reflection at each receiver location. The simulation duration gives at least four time periods of the source signal, at each receiver, for averaging the pressure field in order to calculate the root mean square pressure. The line source placed on the left boundary emits a sinusoid. In order to investigate a range of ka that is significantly large, the discrete frequency of the source signal is taken in the frequency range [200 - 1600] Hz.

TLM calculations are carried out in two main steps in order to extract the pressure field scattered by the scatterer. Firstly, TLM simulations are performed without scatterer for a given monochromatic excitation in the computation domain depicted by figure 3.2. This first step gives the incident pressure field whose root mean square value p_i^{rms} is calculated at each receiver position. The second step consists in running TLM simulations with the scatterer and the same excitation signal. This second step gives the total pressure field, *i.e.* the incident and scattered pressure fields. Finally, subtracting the incident pressure field of the first simulation from the total pressure field of the second simulation gives the scattered pressure field p_s for each simulation. The root mean square scattered pressure p_s^{rms} is then calculated from the scattered field over four periods at each receiver location. Finally, the scattered level L_{scat} (in dB), relative to the incident pressure, obtained from the

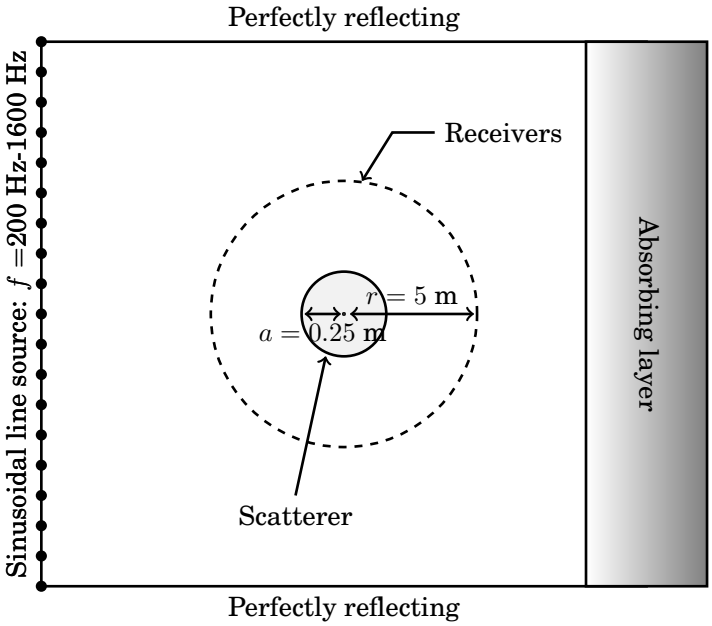

Figure 3.2: *Computational domain of the TLM simulations for the calculation of the pressure field scattered by a circular and acoustically rigid scatterer.*

TLM calculation is given by:

$$L_{\text{scat}} = 10 \log_{10} \left(\frac{p_s^{\text{rms}}}{p_i^{\text{rms}}} \right), \tag{3.8}$$

which can be compared to the analytical solution of equation (3.7).

Figure 3.3 shows an example of the pressure field simulated using the TLM method. A monochromatic plane wave of frequency $f = 100$ Hz coming from the left hits a perfectly rigid cylinder. The difference in magnitude of the instantaneous pressure are depicted by different gray levels, where the intermediate gray shade represents zero, whereas the darker and brighter show the minimal and maximal pressure magnitudes. Figure 3.4 shows the scattered field obtained after subtracting the acoustic field obtained without scatterer (*i.e.* the incident field) from the total field.

Comparisons between TLM calculations and analytical solutions

The scattered pressure level obtained from the TLM calculations are compared to the theoretical scattered level detailed in section 3.2.1 (Equation (3.7)). Figure 3.5 shows the polar variation of the scattered pressure field level obtained after the plane wave hits the cylinder. Each simulation corresponds to a given frequency of the line source in the frequency range [200 - 1600] Hz. For all simulations, the scattered pressure level pattern is in good agreement with the theory. Therefore, it can be said that 2D single scattering from a circular and perfectly reflecting scatterer can be taken into account using the TLM method.

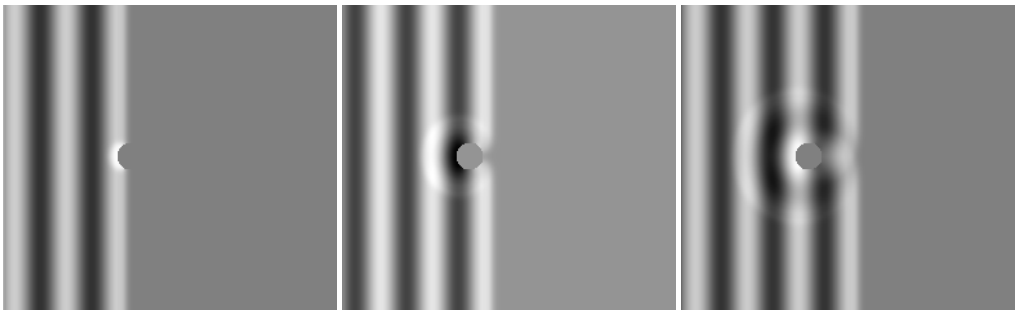

Figure 3.3: *TLM simulation of a monochromatic plane wave scattered by a perfectly reflecting cylinder; distribution of pressure magnitude at three different times.*

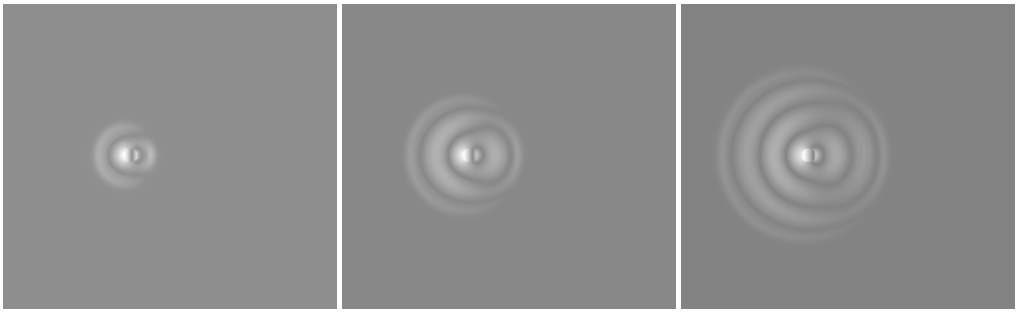

Figure 3.4: *Instantaneous pressure magnitude of the scattered field* p_s *at three different times.*

The slight differences between the analytic solution and the TLM simulation can be caused by the discretization inherent to the transmission-line network. Figure 3.6 shows that a reduced spatial step can lead to slightly better results for the two frequencies 400 Hz and 800 Hz. In this case, the influence of the discretization would need deeper investigations to be clearly observed.

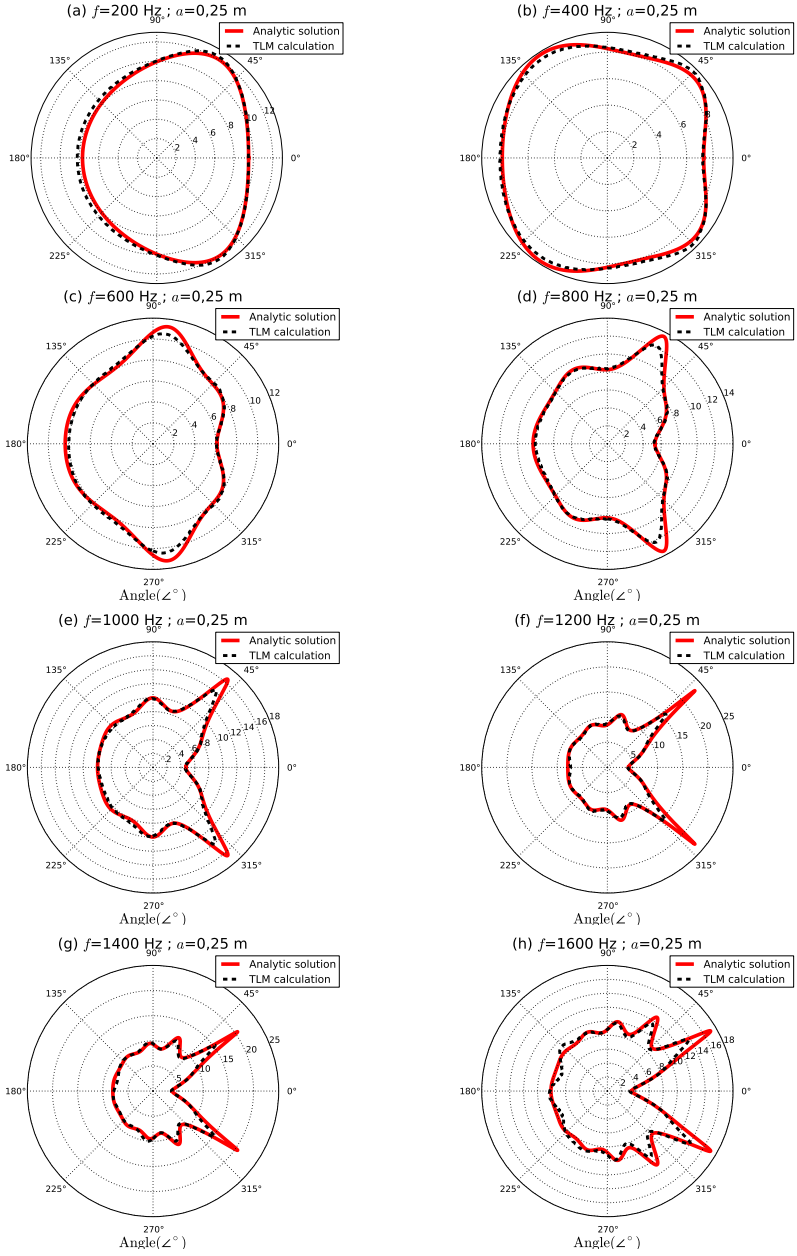

Figure 3.5: *Sound pressure level L_{scat} for a circular scatterer whose radius is $a = 0.25$ m, analytical solutions (Bruneau [61]) (red curve —) and TLM calculations (black dashes - -):* (a) $f = 200$ Hz, ***ka = 0.92;*** (b) $f = 400$ Hz, ***ka = 1.85;*** (c) $f = 600$ Hz, ***ka = 2.77;*** (d) $f = 800$ Hz, ***ka = 3.70;*** (e) $f = 1000$ Hz, ***ka = 4.62;*** (f) $f = 1200$ Hz, ***ka = 5.54;*** (g) $f = 1400$ Hz, ***ka = 6.47;*** (h) $f = 1600$ Hz, ***ka = 7.39.***

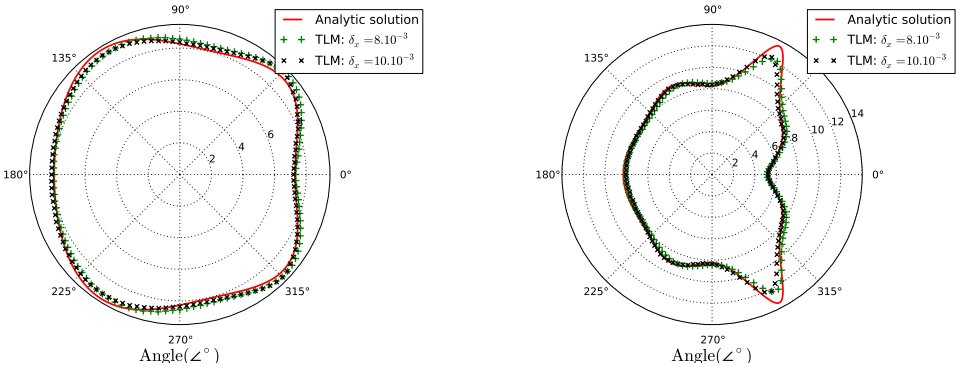

(a) $f = 400$ Hz (b) $f = 800$ Hz

Figure 3.6: *Sound level pressure L_{scat} for a circular scatterer; comparison between the analytic solutions and two TLM simulations with $\delta l = 8.10^{-2}$ m and $\delta l = 10.10^{-2}$ m, at* (a) $f = 400$ Hz *and* (b) $f = 800$ Hz.

3.2.2 Scattering of spherical wave by a cylinder normal to an impedance ground (3D)

In this section, the 3D case of wave scattering by a single cylinder normal to an impedance ground is considered. The TLM simulations are compared to both semi-analytic solutions and measurements on scale models.

3.2.2.1 Semi-analytic model

The present model has been published by Swearingen and Swanson [62]. The geometry of the semi-analytic model is depicted in figure 3.7. The spherical wave emitted by the point source interacts both with the ground and the cylinder of infinite height. Therefore, the scattering effect caused by the cylinder is coupled to ground effect. The ground is assumed to be locally reacting in this model.

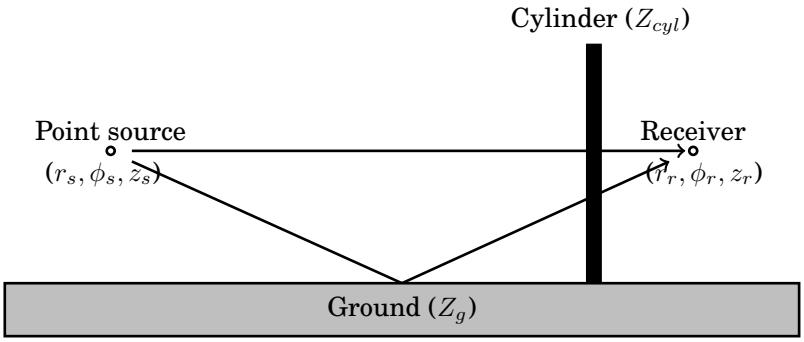

Figure 3.7: *Geometry of the model for a cylinder placed normal to an impedance plane.*

Using a cylindrical coordinate system (r, ϕ, z), the full pressure field can be split up into six components as:

$$\frac{e^{\jmath kR_1}}{R_1} = \int_{-\infty}^{\infty} p_{\text{inc}} e^{\jmath\zeta(z_r - z_s)} \mathrm{d}\zeta, \tag{3.9a}$$

$$\frac{e^{\jmath kR_2}}{R_2} = \int_{-\infty}^{\infty} p_{\text{inc}} e^{\pm\jmath\zeta(z_r + z_s)} \mathrm{d}\zeta, \tag{3.9b}$$

$$-2\frac{k}{Z_g}\int_0^{\infty} e^{-(k/Z_g)q} \frac{e^{\jmath k|r - \hat{x}r_s \pm \hat{z}(z_s + \jmath q)|}}{|r - \hat{x}r_s \pm \hat{z}(z_s + \jmath q)|} \mathrm{d}q = -\int_{-\infty}^{\infty} \frac{2k}{k + Z_g\zeta} p_{\text{inc}} e^{\pm\jmath\zeta(z_r + z_s)} \mathrm{d}\zeta, \tag{3.9c}$$

$$\int_{-\infty}^{\infty} p_{\text{scat}} e^{\jmath\zeta(z_r - z_s)} \mathrm{d}\zeta, \tag{3.9d}$$

$$\int_{-\infty}^{\infty} p_{\text{scat}} e^{\pm\jmath\zeta(z_r + z_s)} \mathrm{d}\zeta, \tag{3.9e}$$

$$-\int_{-\infty}^{\infty} \frac{2k}{k + Z_g\zeta} p_{\text{scat}} e^{\pm\jmath\zeta(z_r + z_s)} \mathrm{d}\zeta, \tag{3.9f}$$

with

$$p_{\text{inc}} = \sum_{n=0}^{\infty} P_n(\zeta)\varepsilon_n \jmath^n (-1)^n J_n(r\sqrt{k^2 - \zeta^2})\cos(n\phi), \tag{3.10}$$

and

$$p_{\text{scat}} = \sum_{n=0}^{\infty} P_n(\zeta)\varepsilon_n \jmath^n (-1)^n D(n) H_n^{(1)}(r\sqrt{k^2 - \zeta^2})\cos(n\phi), \tag{3.11}$$

where $D(n)$ is the scattering coefficient defined by equation (3.6) and P_n is given by:

$$P_n(\zeta) = \frac{\jmath(-\jmath)^n}{2} H_n^{(1)}(r_s\sqrt{k^2 - \zeta^2}). \tag{3.12}$$

Referring to the notation shown in figures 3.7 and 3.8, the distances R_1 and R_2 are written as:

$$R_1 = \sqrt{(r_r^2 + r_s^2 - 2r_r r_s\cos(\pi - \phi)) + (z_r - z_s)^2}, \tag{3.13a}$$

$$R_2 = \sqrt{(r_r^2 + r_s^2 - 2r_r r_s\cos(\pi - \phi)) + (z_r + z_s)^2}. \tag{3.13b}$$

The six components that constitute the full pressure field (Eqs. (3.9)) can be split into two groups. First, the ground components (a), (b) and (c) correspond respectively to the direct path, the ray that is reflected before (+) or after (-) the cylinder, and the image-integral that represents the complex reflexion and the ground wave. Secondly, the scattering components (d), (e) and (f) correspond respectively to the direct scattered, the reflected scattered (+) or scattered reflected (-), and the image-integral. The full field is given by the summation of all components after numerical integrations. The Miki impedance model [127] is used to estimate the surface impedance of the ground in the following analytic calculations. In the following sections, all the integrals of this analytic model are numerically solved using trapezoidal integration.

3.2.2.2 TLM simulations setup

The TLM simulations are carried out in a 3-dimensional computational domain using the Python/OpenCL-TLM code (Section 2.1.3). As shown in figure 3.8, the point source (S) is placed 2.0 m above the ground and a crown of 720 receivers (R) is centered around the cylinder at the same height. The radius of the cylinder is equal to $a = 1.25\ 10^{-1}$ m. The source signal is a pulse that is limited to the frequency 1000 Hz. The ground is first assumed to be perfectly reflecting, and secondly as locally reacting with a surface impedance Z_g. The ground surface impedance Z_g is calculated in the TLM model using the Miki impedance model [60]. The other edges of the domain are made of absorbing layers based on the one way approach (Section 2.2.2.2). The spatial step is set equal to $\delta_l = 2.10^{-2}$ m and the duration of the simulation is $t_{\text{sim}} = 0.5$ s.

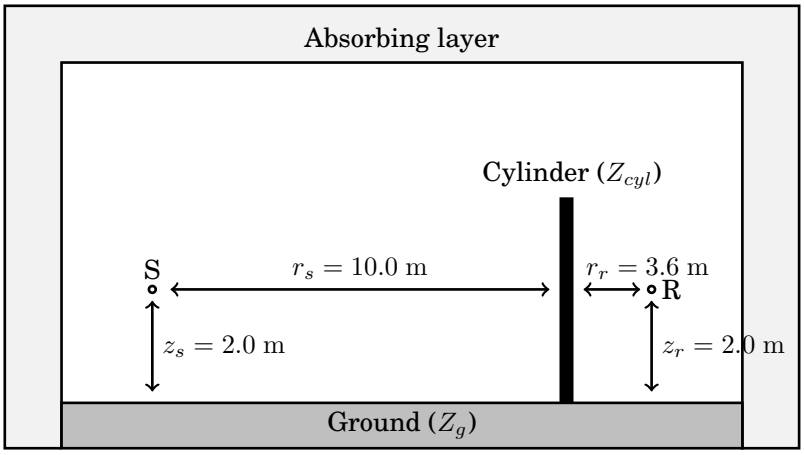

(a) Side view

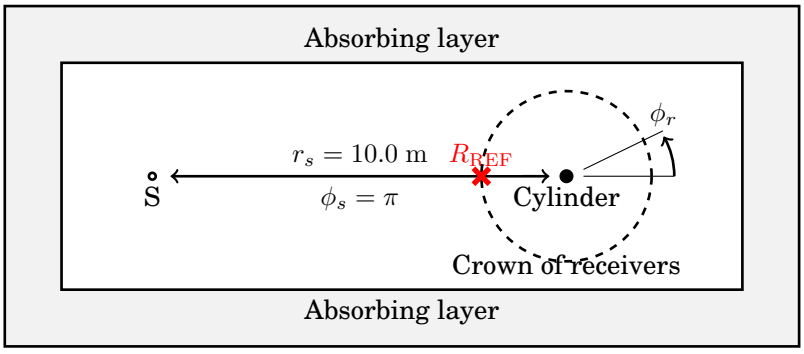

(b) Top view

Figure 3.8: *Geometry of the numerical setup:* (a) *side view;* (b) *top view*.

3.2.2.3 Measurements setup

The measurements are carried out on scale models, where the configuration depicted in figure 3.8 is reproduced at the scale 1:10. Figure 3.9 shows the experimental setup where the cylinder is made of poly vinyl chloride (PVC). This plastic tube is assumed to be perfectly reflecting. Two different types of grounds are used for the measurements. Firstly, a smooth varnished plate of wood, which is assumed to be perfectly reflecting, is used for the first set of measurements. A second set of measurements is performed above a felt-covered plate. The felt is about 1 mm thick and directly stuck on a plate of wood.

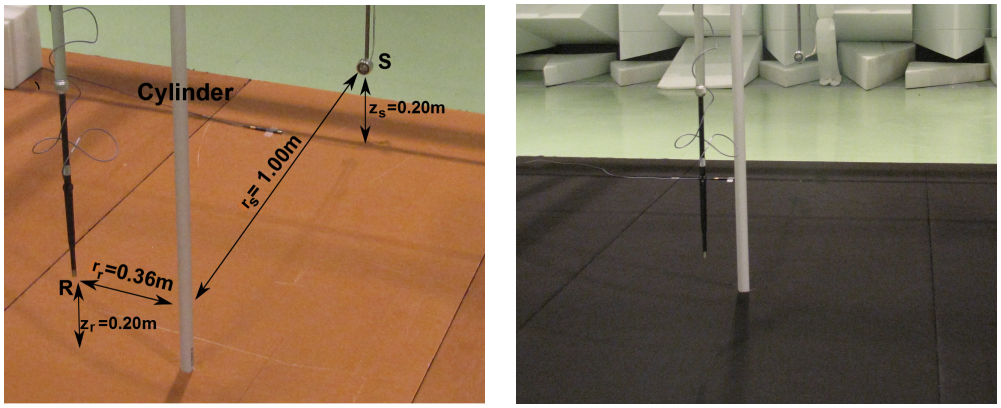

(a) Reflecting ground (b) Impedance ground

Figure 3.9: *Experimental setup for the measurement of spherical waves scattered by a rigid cylinder above a ground (example for receiver position* $\phi_r = 90°$*):* (a) *reflecting ground (*i.e. *varnished plate of wood),* (b) *impedance ground (*i.e. *felt covered plate).*

Measurements have been carried out over both the varnished plate of wood and the felt-covered plate in order to estimate the surface impedance of such artificial grounds. After fitting the curves for several source heights and microphones locations, it has been shown that the varnished plate of wood is equivalent to a perfectly reflecting surface. The mean flow resistivity of the felt-covered plate is estimated to be around $\sigma_g = 610$ kN.s.m^{-4}. This resistivity is used with the Miki impedance model for the calculation of the ground surface impedance for both the TLM simulations and the analytic solutions.

The source is a tweeter emitting a white noise from 1 kHz to 12.5 kHz at the scale model (SM) 1:10, which corresponds to 100 Hz to 1250 Hz at full scale (FS). The impulse response is calculated at each receiver position. To check the directivity of the source, the difference level relative to normal incidence for the octave bands from 2 kHz to 12.5 kHz (SM) is shown in figure 3.10 at two distances: 0.5 m and 1.0 m. It can be seen that for an incident angle that ranges from $-40°$ to $40°$, the absolute level deviation relative to normal incidence does not exceed 3 dB for the octave bands centered on 2 kHz to 8 kHz (SM). The fluctuation observed at 2 kHz

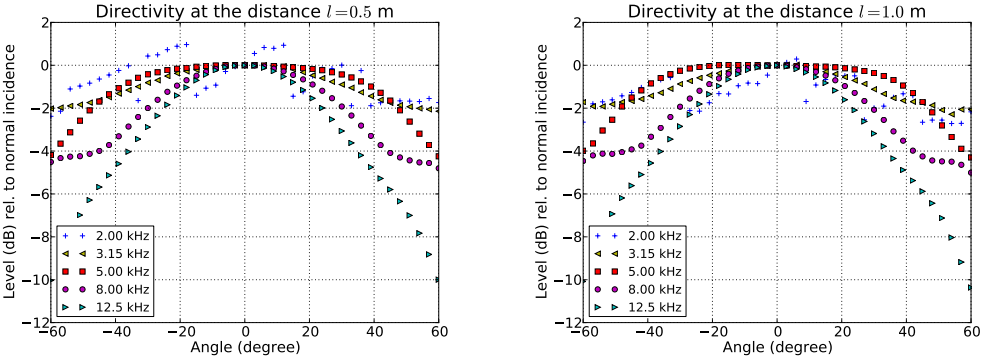

(a) $l = 0.5$ m (b) $l = 1.0$ m

Figure 3.10: *Source directivity (*dB*) relative to normal incidence (*0°*) at the distances:* (a) $l = 0.5$ m*;* (b) $l = 1.0$ m.

(SM) may be due to the low cut-off frequency of the tweeter. However, in a first approximation, the tweeter can be assumed to be omnidirectional regarding both the frequency range 1 kHz to 10 kHz (SM) and the small angle span considered in this study (*i.e.* for a single cylinder the directivity of the source is less important than for a forest).

The receiver is a 1/4 inch microphone, which is monitored by an automaton in order to set the most precise position at all measurement points. From the impulse response measured at each position, the frequency response is obtained. In the next section, these frequency responses are shown and compared to the analytic solutions and to TLM simulations.

3.2.2.4 Results

In this section, the results obtained from the TLM simulations are compared to the analytic solutions and to the measurements. Three receiver positions are chosen to present these comparisons, respectively at $\phi_r = 0°,\ 45°,$ and $90°$. Each frequency response is calculated relatively to the reference receiver located at $\phi_{r-\mathrm{REF}} = 180°$, *i.e.* the reference point is in front of the source (Figure 3.8). The results are presented respectively for a perfectly reflecting ground in figure 3.11 and for an impedance ground in figure 3.12 at full scale (FS) frequency.

At each position the TLM simulations are in good agreement with both analytic and experimental results for both the reflecting ground and the impedance ground. The peaks at frequencies 140 Hz and 160 Hz given by the analytic solution for reflecting ground are caused by the scattered part of the analytic model. No straightforward explanation is found yet for these two peaks that are not reproduced by the TLM response. The integration method in analytic model or to the approximation of the circle by staircases in TLM modeling could be responsible for this discrepancy. This remains to be tested for further explanations. It can be seen that, for the impedance ground, the analytic solution is slightly diverging compared to the simu-

lations and the measurements. At low frequency, this can be due to the impedance model chosen for the estimation of the ground surface impedance. At medium and high frequencies the fluctuations of the analytic results are more likely caused by the scattered part, where the trapezoidal integration method can be responsible for such phenomena. Although small discrepancies that could be additionally caused by the measurements or the simulations placement uncertainties, each frequency response for both reflecting and impedance grounds obtained with the TLM method are in good agreement with analytic and experimental results. This confirms the ability of the TLM method to take into account the scattering of an acoustic wave by a cylinder placed normal to a reflecting or an impedance ground.

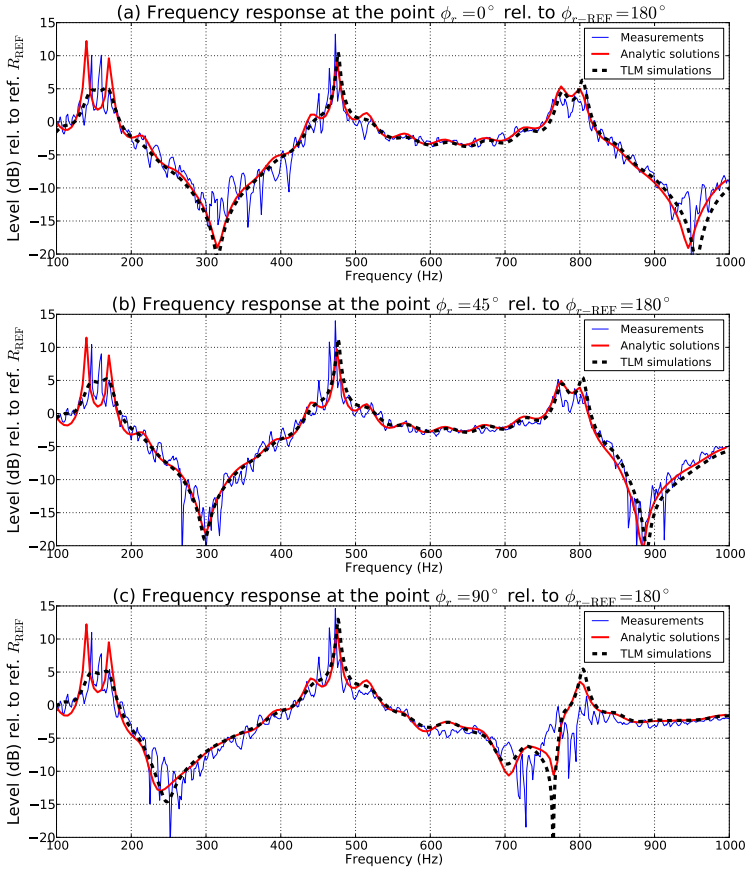

Figure 3.11: *Frequency responses (FS) for a perfectly reflecting ground relative to* $\phi_{r-\mathrm{REF}} = 180°$*, for the TLM simulation (dashed line), the measurements (blue solid line) and the analytical solutions (red solid line) calculated at:* (a) $\phi_r = 0°$*;* (b) $\phi_r = 45°$*;* (c) $\phi_r = 90°$.

It can be interesting to identify the ground effect contribution and the scattering contribution in the previous frequency responses. Therefore, the analytic solutions with and without cylinder for a reflecting ground and an impedance ground are calculated and shown in figure 3.13. In the case of the reflecting ground, it can be seen

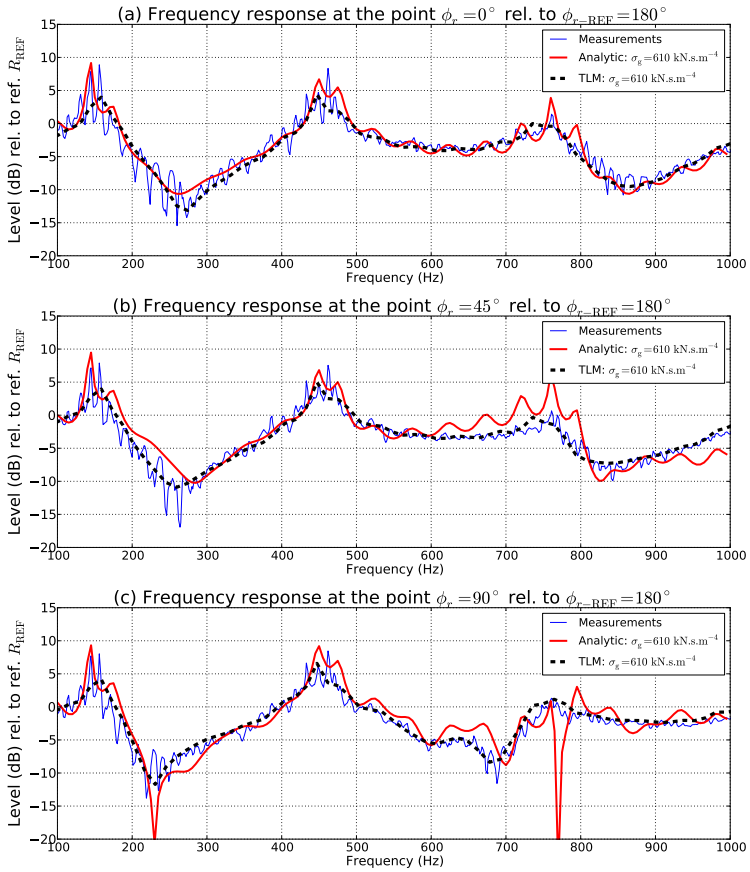

Figure 3.12: *Frequency responses (FS) for an impedance ground relative to* $\phi_{r-\mathrm{REF}} = 180°$*, for the TLM simulation (dashed line), the measurements (blue solid line) and the analytical solutions (red solid line) calculated at:* (a) $\phi_r = 0°$*;* (b) $\phi_r = 45°$*;* (c) $\phi_r = 90°$.

that the scattering induces small fluctuations of the frequency response that corresponds to the ground effect only. In the case of impedance ground, as expected, the resonance and anti-resonance dips are shifted to lower frequency compared to the perfectly reflecting cases. The first resonance of the impedance ground with scattering is slightly deeper and shifted to higher frequencies compared to the ground effect only. For both reflecting and impedance grounds, it can be seen that the scattering tends to increase the frequency response magnitudes compared to the ground effect only.

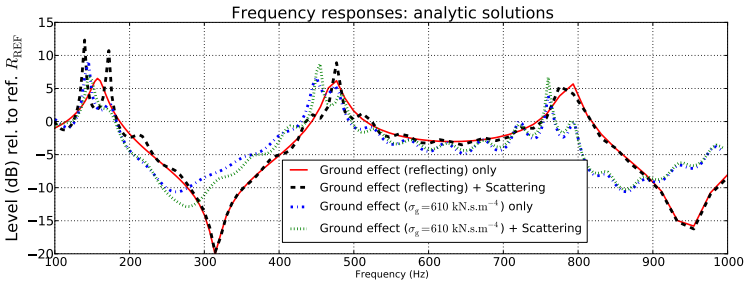

Figure 3.13: *Comparison between the analytic frequency responses (FS) with the ground effect only and the ground effect plus the scattering caused by the cylinder calculated at* (a) $\phi_r = 0°$ *relative to* $\phi_{r-\mathrm{REF}} = 180°$.

3.2.3 Conclusion

The general theory of 2D diffraction by a circular scatterer has been introduced through the derivation of the Helmholtz equation solutions written in a cylindrical coordinates system. TLM simulations have been carried out to study the diffraction of a plane wave by a single circular cylinder. The range of ka for this study spans over 0.92 to 7.39, which gives several distinct diffraction patterns as a function of the frequency. The polar variation of the scattered pressure field obtained from the TLM calculations are in good agreement with the theoretical scattered field. From this comparison, it is shown that the TLM method accurately takes into account the single diffraction of a plane wave by a circular scatterer. Moreover, the comparison of the frequency responses for the cylinder placed normal to either a reflecting or an impedance ground shows also that the TLM method is in correct agreement with both analytic and experimental results.

As stated at the beginning of this section, single scattering appears to be the simplest case leading to multiple scattering. Therefore, this first validation of the TLM method for single scattering can be seen as the starting point for the study of multiple scattering of sound wave through a forested area with the TLM method. Section 3.3 introduces the multiple scattering phenomena through analytical, experimental and numerical methods.

3.3 Simulation of multiple scattering using the TLM method

Considering an incident plane wave traveling through an area that contains several scatterers, the interaction of the acoustic wave with these scatterers gives rise to the physical phenomena named as multiple scattering. In this document, the scatterers are, in a first approach, considered acoustically perfectly reflecting and circular.

Section 3.3.1 deals with 2D multiple scattering that is studied analytically from Twersky [128] and Embleton [71] theory, and compared to the TLM simulations. Section 3.3.2 presents an experimental study of the 3D case, where multiple scattering from cylinders normal to a ground is measured on scale models and compared to the TLM simulations.

3.3.1 Multiple scattering by 2D circular scatterers

3.3.1.1 Theory

The geometry and the notations used for the derivation of the analytical models corresponds to those denoted in figure 3.14. In this section, multiple scattering

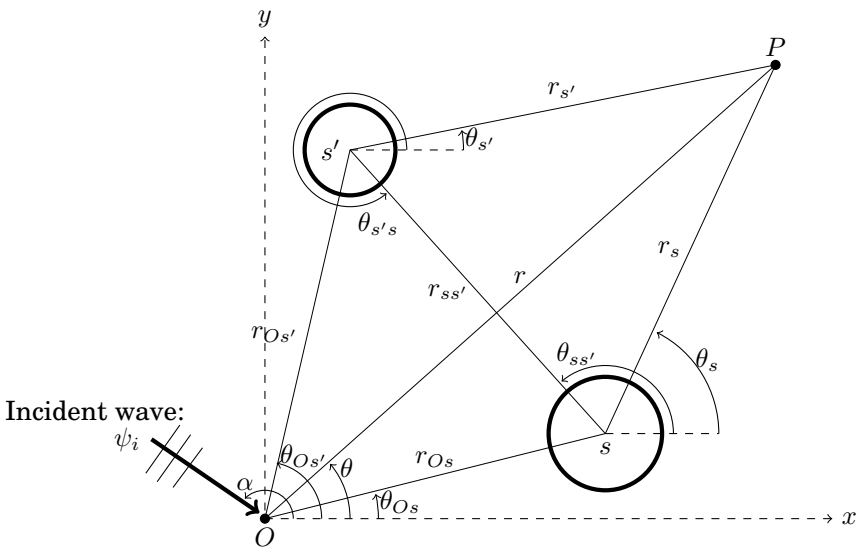

Figure 3.14: *Incident plane wave on a set of two circular scatterers.*

is described using the velocity potential ψ [128]. In the configuration depicted by figure 3.14, an incident plane wave ψ_i hits a set of two circular scatterers s and s'. The incident plane wave can be written in the coordinate system relative to the

origin as

$$\psi_i = e^{\jmath \vec{kr}} = e^{\jmath kr_{Os}\cos(\theta_{Os}+\pi-\alpha)} \sum_{n=-\infty}^{+\infty} J_n(kr_s) e^{\jmath n(\theta_s-\alpha+\pi/2)}$$
$$= \sum_{n=-\infty}^{+\infty} (-\jmath)^n e^{-\jmath kr_{Os}\cos(\alpha-\theta_{Os})-\jmath n\alpha} J_m(kr_s(P)) e^{\jmath m\theta_s(P)}, \tag{3.14}$$

where J_n is the Bessel function of order n, k is the wave number, $r,\ r_{Os}$ and r_s are the distances respectively between the reference and the observation point, between the reference and the considered scatterer, and between the considered scatterer and the observation point.

Twersky [128] introduces the concept of scattering orders, denoted by the index m in the following equations. Here, the wave equation is solved using Hankel functions. Considering the scatterer s, each order of scattering is written as

$${}^s\psi^m = \sum_{n=-\infty}^{+\infty} {}^sA_n^m H_n(kr_s) e^{\jmath n\theta_s}, \tag{3.15}$$

where ${}^sA_n^m$ are the scattering coefficients that can be determined from the boundary conditions for each order m and each scatterer s. The index n denotes the Hankel function orders. Thus, the total wave field scattered by a set of N circular scatterers ($s = [1:N]$), when the order of scattering tends to infinity ($m \to +\infty$), is written as

$$\Psi = \psi_i + \sum_{s=0}^{N}\sum_{m=1}^{+\infty} {}^s\psi^m = \sum_{s=0}^{N}\sum_{n=-\infty}^{+\infty} H_n(kr_s)e^{\jmath n\theta_s} \sum_{m=1}^{+\infty} {}^sA_n^m = \sum_{m=1}^{+\infty} \Psi^m. \tag{3.16}$$

The first scattering order ($m = 1$) corresponds to the incident wave and the scattering of this incident wave by the scatterer s only: $\psi^1 = \psi_i + {}^s\psi^1$. The second order of scattering ($m = 2$) corresponds to the scattering by the scatterer s of each scattered wave coming from the first order: $\psi^2 = \sum_{s'\neq s} {}^{s'}\psi^1 + {}^s\psi^2$. In this way, each scattering order m can be described from the order $m-1$. For example, using the Graf's addition theorem, written as:

$$H_m(kr_{s'}(P))e^{\jmath m\theta_{s'}(P)} = \sum_{q=-\infty}^{+\infty} e^{\jmath(m-q)\theta_{ss'}} H_{q-m}(kr_{ss'}) J_q(kr_s(P)) e^{\jmath q\theta_s(P)}, \tag{3.17}$$

the total field Ψ for $m = 2$ can be written as

$$\Psi = \sum_{n=-\infty}^{+\infty} \left((-\jmath)^n e^{-\jmath kr_{Os}\cos(\alpha-\theta_{Os})-\jmath n\alpha} + \sum_{s\neq s'}\sum_{q=-\infty}^{+\infty} {}^sA_q^1 H_{n-q}(kr_s s') e^{\jmath(q-n)\theta_{ss'}} \right) J_m(kr_s(P)) e^{\jmath m}$$
$$+ \sum_{l=-\infty}^{+\infty} ({}^sA_i^1 + {}^sA_i^2) H_l(kr_s(P)) e^{\jmath l\theta_s(P)}. \tag{3.18}$$

Considering the scatterer s as perfectly reflecting, the boundary condition for the order $m = 1$ can be written as:

$$(\psi_i + {}^s\psi^1)_{r=S_{cyl}} = 0, \tag{3.19}$$

where S_{cyl} is the surface of the scatterer s, which gives the solution for the scattering coefficient ${}^{s}A_n^1$. In reference [128], Twersky shows that a general expression for the scattering coefficients of m^{th} order of scattering can be derived from the $(m-1)^{\text{th}}$ order. In other words, from a general recursive relation, any order of scattering can be obtained from the previous orders.

The quantity of interest is the field transmitted ψ_t through an array of circular scatterers [67, 71]. This array can be seen as a linear time-invariant system whose acoustics properties can be predicted from the study of the scattering phenomena inside the system. The waves propagating inside the array of scatterers can be split into two parts: one is transmitted to the end of the array and the other is back-scattered. Embleton [71] reminds that such phenomena can be expressed with the average wave transmitted T and reflected R as given in [67] by:

$$T = \frac{2W}{k} \sum_{-\infty}^{\infty} A_n, \tag{3.20}$$

and

$$R = \frac{2N}{k} \sum_{-\infty}^{\infty} (-1)^n A_n \ , \tag{3.21}$$

where W is the number of scatterers per square meter, k is the wavenumber and the coefficient A_n is given by:

$$A_n = -\frac{\jmath J_n(kr) + (Z/\rho c) J_n'(kr)}{\jmath H_n(kr) + (Z/\rho c) H_n'(kr)}. \tag{3.22}$$

From equations (3.20) and (3.21), Twersky [67] defines two quantities γ and q given by:

$$\gamma_p = \sqrt{(k - \jmath T)^2 + R^2} \tag{3.23}$$

and

$$q = (T + \jmath k - \jmath \gamma_p)/R \ , \tag{3.24}$$

where γ_p is the complex propagation constant and q corresponds to the balance between the transmitted and back-scattered field. From Twersky [67], the internal wave field and transmitted wave field are written as:

$$\psi_i = (1-q) \frac{e^{\jmath \gamma_p x} + q e^{-\jmath \gamma_p (x-2d)}}{1 - q^2 e^{2\jmath \gamma_p d}}, \tag{3.25}$$

and

$$\psi_t = (1-q^2) \frac{e^{\jmath(\gamma_p - k)d}}{1 - q^2 e^{2\jmath \gamma_p d}} \ , \tag{3.26}$$

where ψ_i et ψ_t describes respectively the internal and the transmitted wave field. Embleton [71] studied the relative attenuation RA, which can be written as:

$$RA = 10 \log_{10} \left(\frac{|\psi_t|^2}{|\psi_{t,100ft}|^2} \right), \tag{3.27}$$

where $\psi_{t,100ft}$ is the reference transmitted field calculated for a scatterers array of 100 feet (30.48 m) length and normalized with respect to $Wa = 10^{-2}\ \text{m}^{-1}$, where W is the scatterer density and a the mean scatterer radius.

3.3.1.2 Numerical simulations

Geometry and numerical setup

The numerical simulations presented in this section aims at comparing the TLM method with the theory [71]. The TLM simulations, which refer to Embleton's work, are inspired by the results shown in [72]. In this approach, the numerical domain can be seen as a corridor that is made of a line source at the entrance and a line of receivers near to the end. The scatterers area is placed between the source and the receivers.

The TLM calculations are performed using the Scilab-TLM code (Section 2.1.3). A line source generating a sinus signal, which frequency ranges from 50 Hz to 800 Hz, is defined. The transmission-line network is defined as a square lattice with a spatial step equal to $\delta l = 2.5\ 10^{-2}$ m. This spatial step corresponds to a sampling frequency equivalent to $\lambda/17$ for the maximal frequency 800 Hz.

As shown in figure 3.15, the scatterers area is defined by its surface S_{scat} (*i.e.* the area where the scatterers are located), the radius of the scatterers a and the number of scatterers per square meter W. In this study, in order to produce realistic results, the placement of the scatterers is related to forest spatial structure analysis and is detailed in the next section. Boundaries along the length are perfectly reflecting, and the ends of the corridor are made of absorbing layers based on the one way approach (Section 2.2.2.2). The complete computational domain is an area

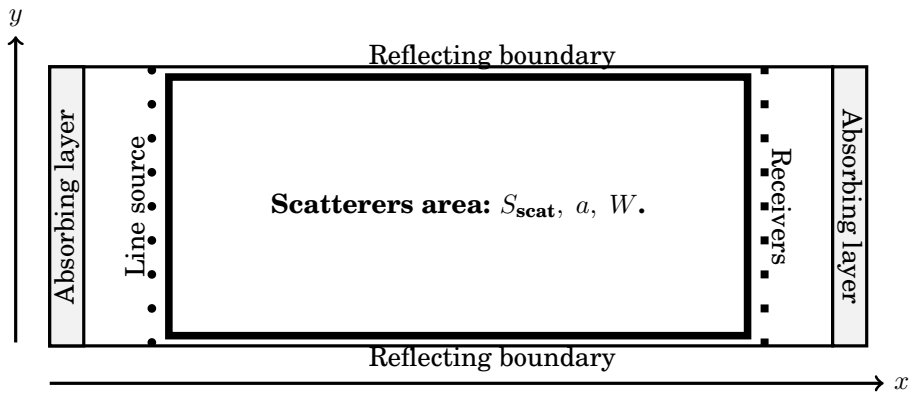

Figure 3.15: *Computational domain of the TLM simulations for the study of multiple scattering.*

of $10\ \text{m} \times 44.5\ \text{m}$, where the scatterers area is a sub-domain such as for example the one depicted in figure 3.18(a). Therefore, the transmission-line network is made of $(n_x = 1780) \times (n_y = 400) = 7.12\ 10^5$ nodes. The line source is located at $x = 4$ m along the y-axis and the receivers are located at $x = 34.48$ m parallel to the y-axis (Figure 3.15). This gives an horizontal distance between the source and the receivers equal to 30.48 m (100 ft) as used in [71]. The time step for each simulation is $\delta t = 5.4\ 10^{-5}$ s. The simulation duration is $t_{\text{sim}} = 0.41$ s. The scatterers are two-dimensional circles with the same radius $a = 0.10$ m. The surface of the scatterers is considered perfectly reflecting.

In this study, the aim is to define a pseudo-random placement for the scatterers, where a minimum distance is defined between two consecutive scatterers. The scatterers area is defined using point processes. A point process is a mathematical model that can produce an infinity of point patterns. An observed point pattern is a realization of a point process. The useful definitions that describe the conception of a given scatterer area are given in the following section.

Definitions and properties of a point process

The mathematical models described in this section are related to forest spatial structure analysis. A more exhaustive description of these mathematical models and their applications to this field can be found in the thesis written by Goreaud [129].

A point process is seen as a random process whose realization gives rise to a set of points (a point pattern) that are assumed to be isolated in space. Therefore, a given point process gives an infinity of realizations, where all point patterns have the same properties. In practice here, these properties are extracted from one realization only; thus, the point process is assumed to be homogeneous (stationary: translational invariance), isotropic (rotational invariance) and ergodic (extension of local measure to the complete domain). These hypotheses ensure that the properties extracted from a sub-domain are the same for all sub-sets and can be extended to the whole domain. The verification of the homogeneity is impacted by the bias caused by the presence of boundaries. This bias is taken into account using edge effect corrections for the calculations of the following functions. In the following cases, the point patterns are defined using properties such as density, scatterers radius, and attraction or repulsion distances.

The Poisson process is an homogeneous and isotropic point process, where the position of a given point is independent of the other point locations. This process verifies the complete spatial randomness (CSR) hypothesis. The Poisson's distribution is often used as a reference in the study of spatial structure of forests [129]. It represents the ideal balance between clustered and dispersed distributions. It is shown that the number of points enclosed by a surface S is defined according to the Poisson distribution as:

$$P(N(S) = n) = \frac{(WS)^n}{n!} e^{WS}, \tag{3.28}$$

where W is the density, n the number of points and S the surface.

In order to avoid the scatterers overlapping, a mutual repulsion of the points is imposed for distances inferior to the radius of the scatterers. This 'hardcore' radius is set using the Gibbs process. It can be used to define clustering as well as repulsion from a pairwise potential function. In practice, the pairwise potential function can be estimated for a real forest and used in the numerical models to virtually reproduce the real forest structure. In the present work, the Gibbs pairwise potential function is only used to define a minimum repulsion distance equal to twice the radius of the scatterers in the following simulations. In other words, the Gibbs process is used as a correction (*i.e.* rearrangement of the misplaced scatterers) and should not cancel the CSR hypothesis.

Assessment of the realization: in order to confirm that each realization corresponds to a Poisson process that verifies the CSR, each scatterers area is assessed. Two functions are calculated for the assessment, the Ripley function $K(r)$ [130] and its extension, the Besag function $L(r)$ [131].

As a general tool, the Ripley $K(r)$ function can be used to test hypotheses about the point pattern, to estimate parameters, or to fit models. In this sense, $K(r)$ characterizes a given realization at many distances r. The Ripley function is written as

$$K(r) = \frac{1}{W}\frac{1}{N}\sum_{i=1}^{N}\sum_{j\neq i} k_{ij}, \tag{3.29}$$

where N is the total number of scatterers, and k_{ij} is equal to 1 if the distance between the points i and j is inferior to r, and zero otherwise. In some cases, the Ripley function appears to be difficult to interpret; therefore, it can be useful to look at its extension, the Besag function, which is written as:

$$L(r) = \sqrt{\frac{K(r)}{\pi}} - r. \tag{3.30}$$

Both Ripley $K(r)$ and Besag $L(r)$ functions give the same information. However, in cases such as shown in the next section, the Besag function can be easier to interpret.

Definition of the scatterers location for the TLM simulations

Each scatterers area defined for the TLM simulations is based on the Poisson process. This distribution is used as a reference and represents a balance between clustered and dispersed distributions. In order to realize the Poisson process, a given number of points, function of the density, are randomly selected in the x and y Cartesian coordinates following a discrete uniform distribution inside the scatterers area. Once each point has been placed, a repulsion condition for a minimum distance equal to the radius of the scatterers is imposed. This leads to the relocation of the points that overlap. These points are randomly relocated until the spatial location converges to a randomly spaced and non-overlapped scatterers area. In this case the Besag function is constrained in the confidence interval (CI) defined by equation (3.31). The complete procedure adopted for the definition of a scatterers area is depicted in figure 3.16.

Three density of scatterers are defined for the TLM simulations. For all simulations the scatterers radius are the same and set equal to $a = 0.10$ m; the surface is equal to $S_{\text{scat}} = 30.48$ m (100 ft) $\times$ 10.00 m $= 304.80$ m^2. Firstly, a reference scatterers area is defined with a density $W_{\text{ref}} = 0.10$ m^{-1}, which gives the reference factor $W_{\text{ref}}a = 10^{-2}$ m^{-1} (Equation (3.27)). Figure 3.17 shows the realization obtained from the point process and the corresponding Ripley function (Figure 3.17(b)) and Besag function (Figure 3.17(c)). The influence of the edge effect corrections can be observed comparing the red and blue curves. From the Ripley function, it can be seen that the presented realization is close to the ideal Poisson process (black line). Moreover, the value given by the Besag function are inside the confidence interval

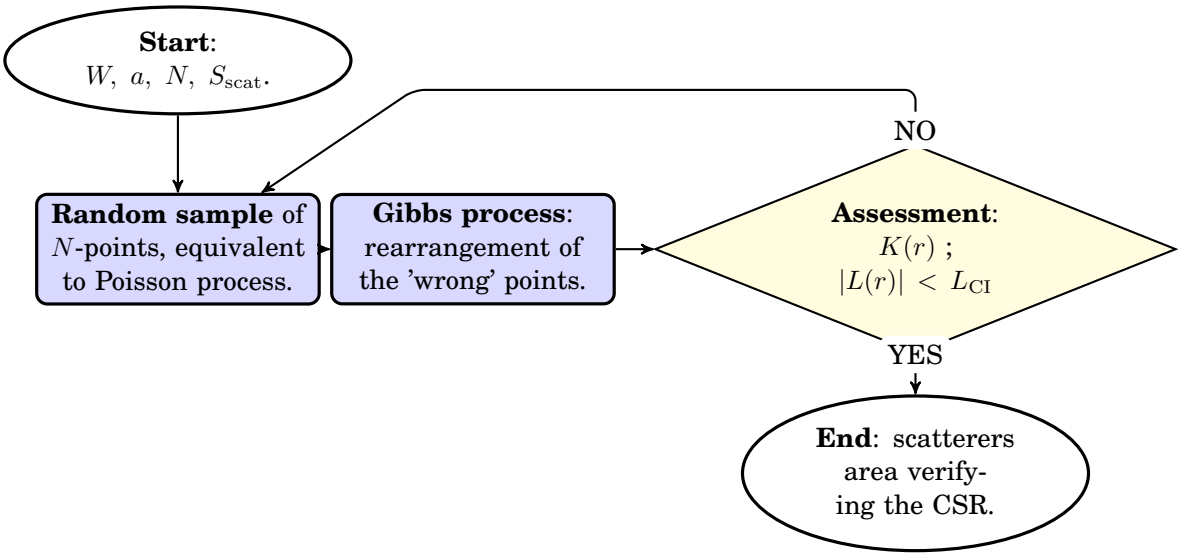

Figure 3.16: *Block diagram for the definition of a scatterers area.*

defined, for a rectangular area, by [130]:

$$L_{\text{CI}} = \pm 1.68 \frac{\sqrt{S_{\text{scat}}}}{N}, \tag{3.31}$$

In the case of figure 3.17, both Ripley and Besag functions show that the realization verifies the CSR hypothesis. In the present study, two scatterers density are chosen respectively equal to $W_1 = 0.20\ \text{m}^{-1}$ and $W_2 = 0.30\ \text{m}^{-1}$. Because, for each density, there is an infinity of realizations verifying the CSR, it is decided to pick up twelve realizations per density to be more representative. Thus, there is a total of 25 scatterers areas, *i.e.* 12 per density and 1 reference. Figure 3.18 shows an example for each density among the twelve realizations. For each scatterers area, the realization is assessed with the Ripley and Besag functions to verify that the distribution is in good agreement with the hypothesis of CSR.

Principle of the simulations

Simulations are carried out to compare the results obtained from the TLM calculations and those given by Embleton [71], and more recently verified by Heimann [72] with an FDTD model.

The quantity used in the following section is the acoustic pressure transmitted p_t from the line source to the receivers, after traveling through a given scatterers area. In other words, p_t can be seen as the addition of the incident pressure and the pressure scattered forward to the line of receivers. This pressure is compared to a reference transmitted pressure $p_{t,100ft}$, obtained with the reference scatterers area (Figure 3.17(a)). This reference can be used to compare the TLM calculations with the results obtained in [71,72]. The TLM calculations are carried out for 16 frequencies in the range [50 Hz - 800 Hz], *i.e.* every 50 Hz, using a sinusoid source. The

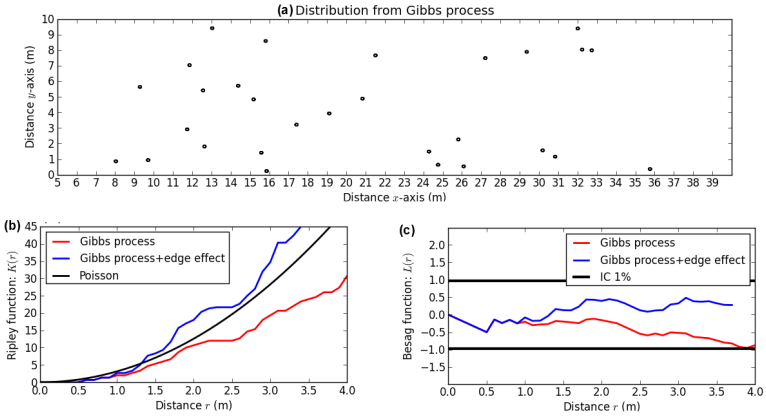

Figure 3.17: *Reference scatterers area with* $a = 0.10$ m *and* $W_{\text{ref}} = 0.10$ m^{-1} *(*$W_{\text{ref}}a = 10^{-2}$ m^{-1}*):* (a) *scatterers area;* (b) *Ripley function* $K(r)$*;* (c) *Besag function* $L(r)$*.*

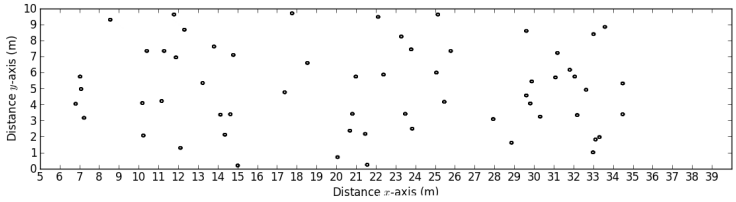

(a) Scatterers area n°1: $W_1 = 0.20$ m^{-1} ($W_1a = 2.10^{-2}$ m^{-1})

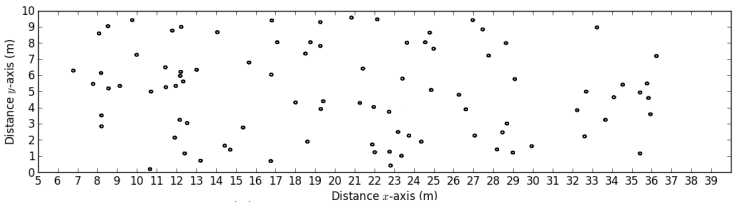

(b) Scatterers area n°2: $W_2 = 0.30$ m^{-1} ($W_2a = 3.10^{-2}$ m^{-1})

Figure 3.18: *Example of scatterers area with* $a = 0.10$ m *and:* (a) $W_1 = 0.20$ m^{-1} *(*$W_1a = 2.10^{-2}$ m^{-1}*);* (b) $W_2 = 0.30$ m^{-1} *(*$W_2a = 3.10^{-2}$ m^{-1}*).*

pressure is averaged over a line of 398 receivers. The root mean square pressure transmitted to the receivers through the scatterers area is calculated over four signal periods. This pressure is used to calculate the relative attenuation (Eq. (3.27)) at each frequency.

3.3.1.3 Comparison between the TLM calculations and the theory

Figure 3.19 compares the theoretical attenuation [71] for purely reflecting scatterers and the TLM simulations, for twelve scatterers realizations (12 runs) for each density (W_1, W_2), relative to the reference scatterers area depicted in figure 3.17. From both figure 3.19 (a) and (b), it can be seen that the attenuations obtained from the TLM simulations at low frequencies (*i.e.* $ka < 1$) are in correct agreement with the trends shown by the theoretical attenuations. For such values of ka the wave length is considered large compared to the scatterers diameter. For $ka > 1$, the fluctuations of the attenuations obtained from the TLM simulations are slightly more dispersed around the theoretical curves. Similar observations have been made in [72], where larger discrepancies between the simulations and the theory have been observed. Furthermore, compared to [72], several realizations have been studied for a given density, which gives more realistic trends for the attenuations. Overall, for each density, the average relative attenuation over the 12 runs (not plotted here) is quite close to the analytic curves.

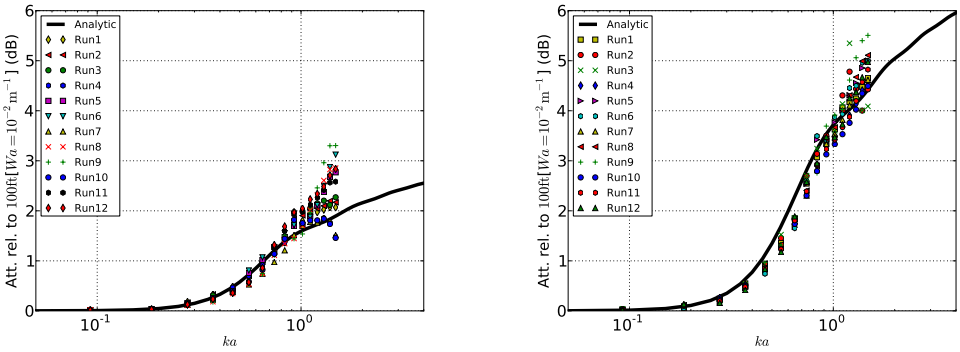

(a) $W_1 a = 2.10^{-2}\mathrm{m}^{-1}$ (b) $W_2 a = 3.10^{-2}\mathrm{m}^{-1}$

Figure 3.19: *Theoretical relative attenuation for perfectly reflecting scatterers [71] and the 12 TLM calculations, normalized with respect to the reference area ($W_{\mathrm{ref}} a = 10^{-2}$ m^{-1}) for:* (a) $W_1 a = 2.10^{-2}$ m^{-1}*;* (b) $W_2 a = 3.10^{-2}$ m^{-1}.

3.3.2 Multiple scattering above a ground (3D)

In this section, the scattering of spherical waves by an array of cylinders above a ground is studied. Since no analytic model has been found in the literature to study this geometry, the TLM simulations are compared to measurement data exclusively. The measurements are performed on 1:10 scale models for several configurations of cylinders and two types of ground.

3.3.2.1 Experimental setup and geometries

The measurement setup is similar to the one described in section 3.2.2.3. An example of the geometry is given in figure 3.20. The geometries of the scale models

(a) Staggered-row above a reflecting ground

(b) Randomly located above an impedance ground

Figure 3.20: *Experimental setup for the measurement of spherical waves scattered by reflecting cylinders:* (a) *in staggered-row above a reflecting ground;* (b) *randomly located above an impedance ground.*

are divided into two configurations of cylinders as shown in figure 3.21. For each configuration, the source height is set equal to $z_{s1} = 0.10$ m and $z_{s2} = 0.20$ m. The point R_{REF} is used as a reference in the following comparisons of the frequency responses. This point is located at the same height as the source and at the entrance of the scatterers areas. The points R_1 and R_2 are located respectively in the middle and at the end of each area, and at the same height as the source.

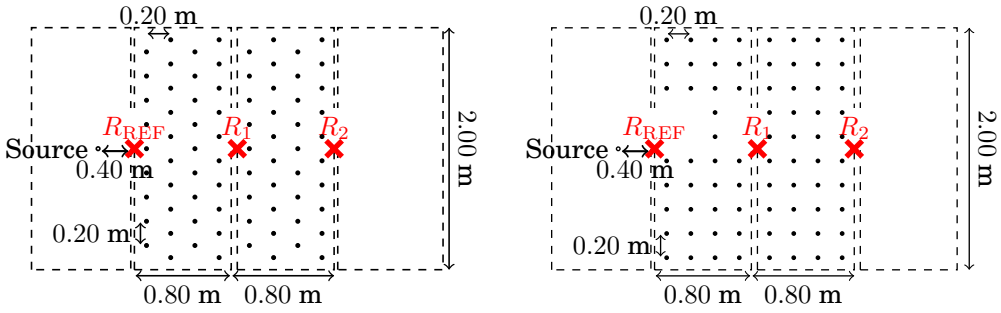

(a) Periodic in staggered-row

(b) Periodic aligned

Figure 3.21: *Top view of the 1:10 scale models for periodical distributions of the cylinders:* (a) *staggered-row;* (b) *aligned.*

In addition to these two geometries, measurements have also been performed on randomly located cylinders (Figure 3.20(b)). In this case, the point processes and the assessment functions described in section 3.3.1.2 have been used to define the cylinders locations on several plates of wood. Each geometry has first been measured above a smooth varnished plate of wood (*i.e.* reflecting ground), and then, above a felt covered ground (*i.e.* impedance ground). However, due to lack of time and numerical problems with the impedance implementation in the Python/OpenCL-TLM code, only the periodic distribution above a reflecting ground have been used in this study.

3.3.2.2 TLM simulations setup

The simulation setup is a reproduction of the two scale models depicted in figure 3.21 but at full scale. Therefore, there is a factor 10 in the dimensions and the frequency band between the simulations and the scale models. The simulations are carried out using the Python/OpenCL-TLM code (Section 2.1.3). A pulse signal, whose frequency components range from 100 Hz to 1000 Hz (FS), is used to calculate the frequency responses at points R_1 and R_2 relative to R_{REF} (Figure 3.21).

3.3.2.3 Results

The comparison between the TLM simulations and the measurements presented in figures 3.22 and 3.23 are in correct agreement. The resonance and anti-resonance peaks are tolerably well predicted in both staggered-row and aligned configurations. Looking at frequencies above 350 Hz, the simulations slightly overestimate the relative level compared to the measurements. This can be caused by the non exact perpendicularity of tubes with the ground during the measurements, which could alter the scattered field. Moreover, at frequency $f = 430$ Hz, the value of ka is close to 1. Around this frequency, the scattered field is dominant and highly fluctuating. Furthermore, there are also uncertainties on the placement of the source and receivers during the measurements. In addition, the lack of omnidirectivity of the source (Figure 3.10) impacts the results. All these measurement uncertainties could partly explain the discrepancies between the TLM simulations and the measurements observed around this frequency.

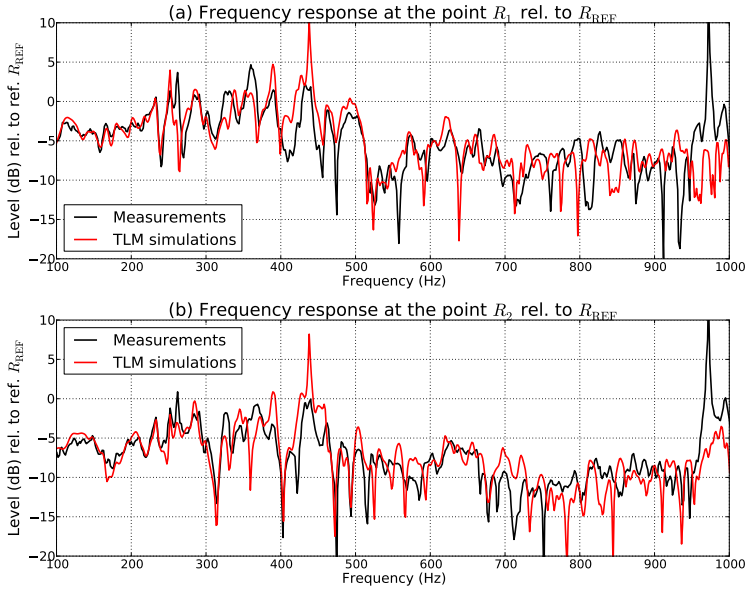

Figure 3.22: *Comparison of the frequency responses obtained from the measurements on the periodic in staggered-row setup and the TLM simulations for a reflecting ground at the points:* (a) R_1*;* (b) R_2*, relative to the point* R_{REF}.

In order to observe the relative amount of the ground effects compared to multiple scattering on the frequency response, the two acoustical phenomena are studied separately.

Firstly, the ground effects are observed with the same source and receivers locations, removing the cylinders. This case is equivalent to wave propagation above a perfectly reflecting ground. Figure 3.24 shows a comparison between the TLM simulations and both analytical solutions and measurement results. In a first observation, it can be seen that the anti-resonance peak centered around $f = 350$ Hz would induce a positive offset in addition to the multiple scattering interference spectrum.

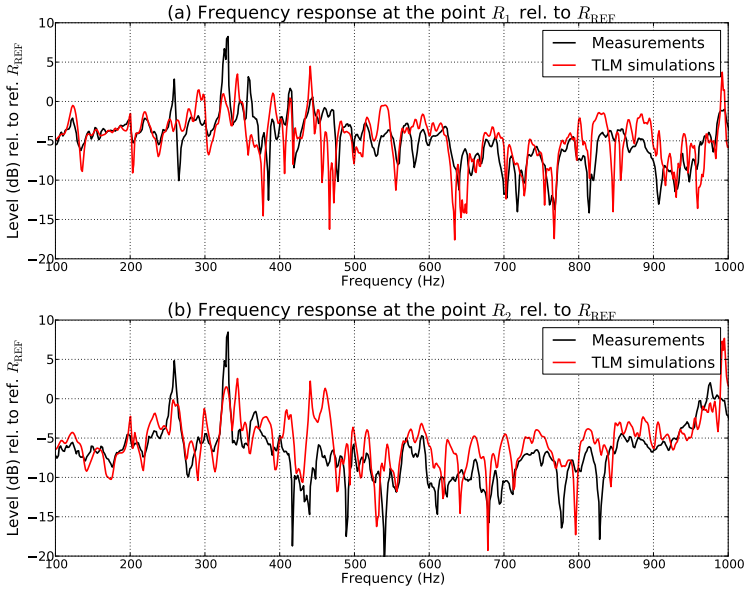

Figure 3.23: *Comparison of the frequency responses obtained from the measurements on the periodic aligned setup and the TLM simulations for a reflecting ground at the points:* (a) R_1*;* (b) R_2*, relative to the point* R_{REF}.

Secondly, the multiple scattering contribution caused by the periodic distributions (Figure 3.21) is simulated using a TLM numerical domain where the ground is replaced by an absorbing layer as depicted in figure 3.25. Figures 3.26 and 3.27 show the comparison between the simulated frequency responses obtained with and without a perfectly reflecting ground for the periodic distributions. As expected, it can be seen that the ground effect induces a positive offset at low frequency and a negative offset at high frequency. This can be related to the results observed in figure 3.24 for wave propagation above a perfectly reflecting ground.

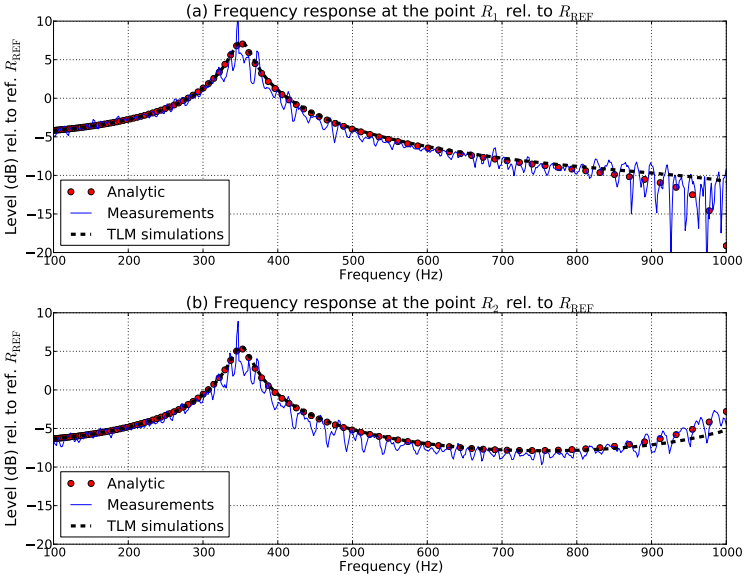

Figure 3.24: *Frequency responses obtained from the analytic solutions, the measurements and the TLM simulations for a wave propagation above a perfectly reflecting ground at the points:* (a) R_1 *;* (b) R_2*, relative to the point* R_{REF}.

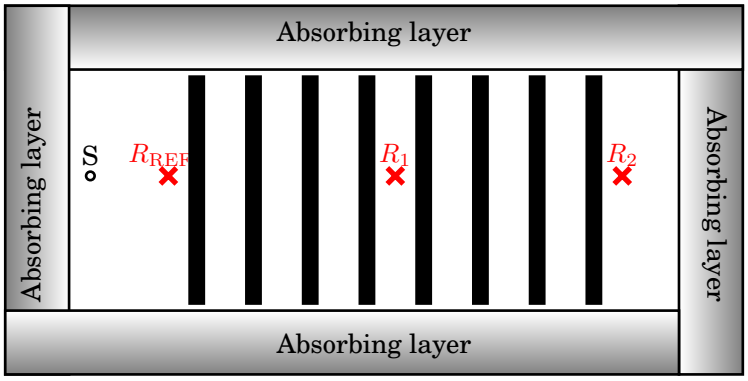

Figure 3.25: *Side view of the numerical domain with the height row of cylinders for the study of multiple scattering without ground effects.*

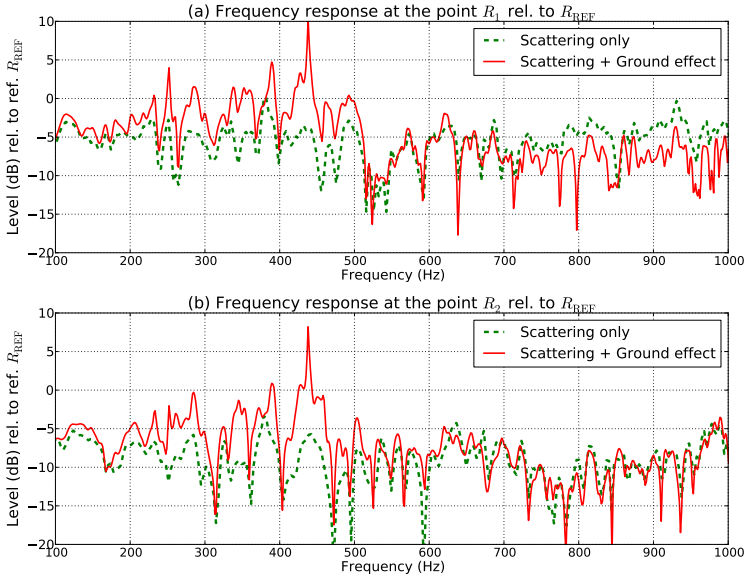

Figure 3.26: *Comparison between TLM simulated frequency responses with and without a perfectly reflecting ground using the periodic in staggered-row distribution at the points:* (a) R_1 *;* (b) R_2*, relative to the point* R_{REF}.

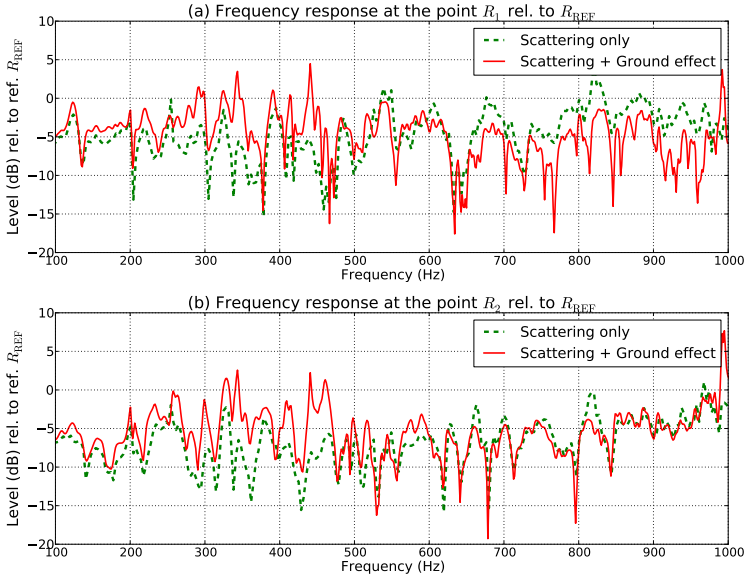

Figure 3.27: *Comparison between the TLM simulated frequency responses with and without a perfectly reflecting ground using the periodic aligned distribution at the points:* (a) R_1 *;* (b) R_2*, relative to the point* R_{REF}.

3.4 Conclusion

Single scattering of an acoustic plane wave has first been investigated using 2D TLM simulations compared to the corresponding analytic model. Good agreements are found between the theory and the TLM method for the estimation of the scattered field. The study of the single scattering coupled to ground effects has been performed comparing 3D TLM simulation and a semi-analytic model. In addition, measurements on scale models have been performed and compared to both numerical simulations and the semi-analytic model, here again with a good agreement. Although, in this case, the scattered contribution is quite low compared to ground effect, the TLM frequency responses show similar trend to the analytic solutions. This study shows the ability of the TLM method for the simulation of acoustic wave propagation above a ground and subject to single scattering.

Investigation of multiple scattering has been carried out using both an analytic model and scale model measurements. Multiple scattering has been first studied using 2D computational domains. The distribution of the scatterers inside the computational domain have been set and assessed using point processes and mathematical tools that are commonly used in the study of forest spatial structure analysis. It is important to note that these statistical tools are used for the first time in the framework of acoustic publications. Therefore, this original application of Ripley and Besag functions to acoustic problems can be seen here as an interesting way to characterize the distribution of scatterers inside a given area. Once the scatterers distributions have been defined, the TLM simulations have shown good agreements with the theory. Lastly, the 3D cases of multiple scattering of acoustic wave propagating above a perfectly reflecting ground has been experimentally studied using scale models. For the two tested geometrical configurations, the TLM simulations are in correct agreement with the experimental results. In addition, comparisons between TLM simulations where the ground has been replaced by an absorbing layer (*i.e.* cylinders in free field) and TLM simulations with a perfectly reflecting ground shows that the ground effect induces an offset of the scattering interference patterns. Unfortunately, due to numerical problems on the implementation of impedance condition for the ground, the felt-covered configurations have not been compared in this document.

In conclusion, this chapter confirms the ability of the TLM method for the simulation of both single and multiple scattering coupled to ground effect. This results represent an encouraging step for the simulation of sound propagation inside forest, as performed in the following chapter.

Chapter 4

SOUND PROPAGATION IN A SIMPLIFIED FOREST

4.1 Introduction

With the development of numerical methods, the propagation of sound in forests can be modeled by including most of the acoustic phenomena detailed in chapter 1. For example, the reader can refer to the works presented in [40, 72, 76, 87]. Among these studies, two of them use the finite-difference time-domain (FDTD) method to predict multiple scattering in forests. Firstly, Heimann [72] presented FDTD simulations using a line source that emits acoustic waves on various arrays of cylinders where the tree trunks (*i.e.* perfectly reflecting cylinders) are randomly located. The density and the diameter of the cylinders are the two parameters used in this study of multiple scattering. It is shown that the attenuation by trunks increases almost linearly with increasing trunk diameter. Furthermore, the attenuations obtained are in good agreement with the theory until reaching the value $ka = 1$. This trend has been further discussed in section 3.3.1.3. In addition, it is found that the impact of the wind field is relatively small compared to the multiple scattering contribution when the receiver is near the ground right after the stand of trunks. Secondly, in the paper proposed by Van Renterghem *et al.* [76], the distributions of cylinders used for the multiple scattering analysis are exclusively periodic. It is shown that from a tree spacing of 3 m and a stem diameter equal to 0.1 m, the studied forest area begins to have a positive impact on the insertion loss. Although these two models include additional acoustic phenomena, such as wind speed vertical gradients in [72] or absorption by tree barks, scattering by stems and ground absorption in [76], no parametric study investigated the comparison between different realistic distributions encountered in forests (random, periodic, clustered...).

Multiple scattering coupled to ground effect has been validated in chapter 3 with the TLM method. Therefore, this method can be used as a reference numerical method in order to investigate the influence of multiple scattering and ground effect on sound pressure levels using realistic forest parameters. Firstly, the TLM simulations are designed to investigate the impact of the trunks distribution and density.

These two parameters are linked to forest using Ripley and Besag functions introduced in chapter 3. Secondly, ground effects on the attenuation of acoustic waves inside forest are studied, comparing results obtained with several ground absorption coefficients. Thus, in the present study, the three main factors of interest are the cylinder distribution, the density of cylinders and the ground reflection coefficient. Due to the computational cost of 3D TLM calculations, some of the numerical parameters are voluntarily simplified. For instance, in this study the height and the length of the forest are limited, and the surface impedance is replaced by a reflection coefficient for the ground effect. In the article written by Reethof *et al.* [65], the measurements on tree barks give an absorption coefficient inferior to 0.08 for most of the samples. The cylinders are considered here, in a first approach, as perfectly reflecting. The other parameters of interest not studied in this chapter are the meteorological effects, the trunks diameter and absorption, and the foliage.

4.2 Design of the numerical simulations

4.2.1 Geometry

The 3D computational domain is depicted in figure 4.1. From the top view (Figure 4.1(a)), the domain is made of two absorbing layers on the left and right sides, and two reflecting planes on the lateral sides. Looking at the side view (Figure 4.1(b)), the upper boundary of the domain is made of an absorbing layer and the lower boundary is the ground that can either be perfectly reflecting or absorbing. The volume containing the cylinders is located at the center of the domain. The various volumes that contain the cylinders are named as arrangements of cylinders or simply arrangements, and are detailed in the following paragraph. The reference line of receivers R_{REF} is placed nearby the source at the entrance of the arrangement. A second line of receivers R_0 is placed at the exit of the array. A line of receivers is made of 50 point receivers, and both lines R_{REF} and R_0 are placed 2 m above the ground. In this first approach, the line source is placed at 2 m height in oder to investigate the ground effect. Although this height does not correspond to any realistic line source height, this academic configuration might emphasize the impact of the ground in order to distinguish it from multiple scattering. The cylinders have the same diameter $d = 0.2$ m and height $h_{\mathrm{cyl}} = 5$ m and their surfaces are perfectly reflecting. The upper absorbing layer begins at the limit of the cylinders top in order to simulate infinitely long cylinders. Any additional downward diffractions from the top of the cylinders toward the ground are avoided. Therefore, these simulations correspond to the propagation inside a forest (*i.e.* below the canopy), where no additional twigs have been modeled. From the top view, this propagation domain can be seen as a large corridor, where the reflecting planes are used to model periodic extensions of both the line source and the arrangement of cylinders.

The seven arrangements of cylinders and the additional empty areas A0 and B0 are described in table 4.1 and figure 4.2. Two lengths are considered: $l_{\mathrm{A}} = 30$ m and $l_{\mathrm{B}} = 40$ m. Two densities (number of cylinders per square meter) are studied: $W_1 = 0.2$ and $W_2 = 0.4$. Four different distributions are defined: complete spatial randomness (CSR), periodic aligned, periodic in staggered row and clustered.

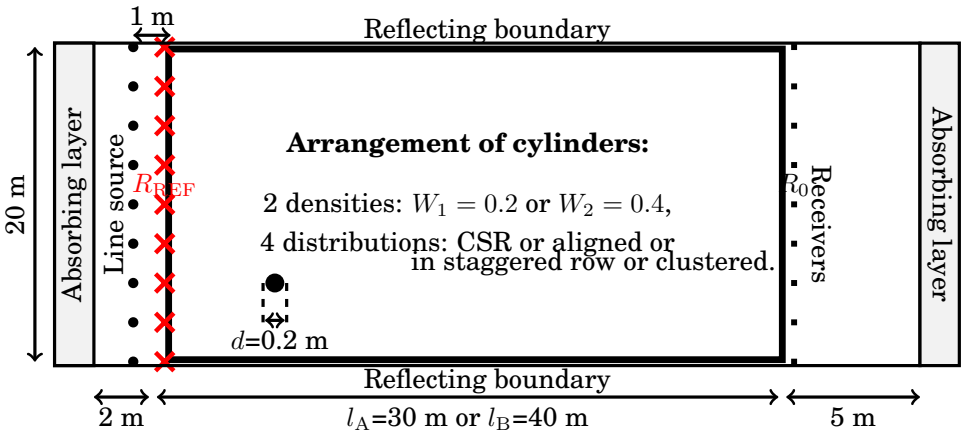

(a) Top view

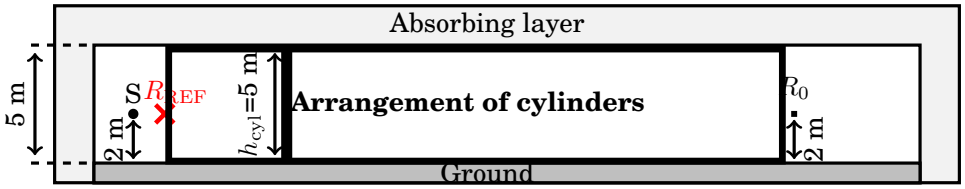

(b) Side view

Figure 4.1: *Computational domain of the TLM simulations for the study of seven arrangements of cylinders:* (a) *top view,* (b) *side view.*

Name of the arrangement	A1	A2	A3	A4	A5	B1	B2	A0	B0
Length (m)	$l_A = 30$ m					$l_B = 40$ m		$l_{A0} = 30$ m	$l_{B0} = 40$ m
Density (nb. of cyl./m^2)	$W_1 = 0.2$	$W_2 = 0.4$	W_2	W_2	W_2	W_1	W_2	$W_0 = 0$	
Distribution	CSR	CSR	Aligned	Stag. row	Clust.	CSR	CSR	No cylinder	

Table 4.1: *Properties of the 7 arrangements of cylinders and of the empty reference areas.*

The five arrangements of cylinders defined using the length $l_A = 30$ m are depicted in figure 4.2. The arrangements A1 and A2 verify the CSR hypothesis for the two densities. This is confirmed by the corresponding Ripley and Besag functions (Section 3.3.1.2), as shown in figure 4.3. The arrangements A3 and A4 are periodic distributions of cylinders respectively aligned and in staggered row. The arrangement A5 is defined using the Gibbs point process, where the attraction and repulsion of the cylinders is set to form a clustered pattern. In this case, the cylinders are regularly aggregated to form small groups that delimit several surfaces of high density inside the area. Figure 4.4 shows the corresponding Ripley and Besag functions, where the Besag function presents positive values out of the confidence

interval for the distances 0.5 m to 3.0 m. This means that, inside this distance interval, the cylinders are found to be attracted to each other, which results in the clustering patterns shown in figure 4.2(e).

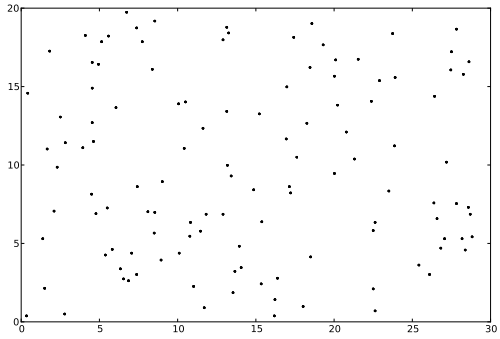

(a) A1: $W_1 = 0.2$, CSR

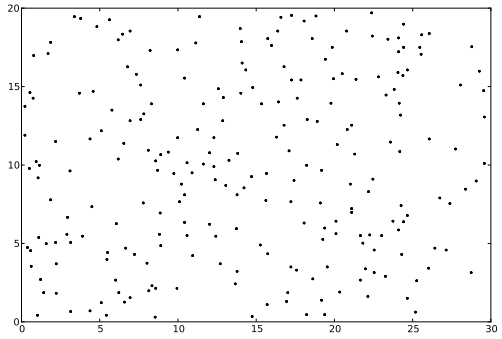

(b) A2: $W_2 = 0.4$, CSR

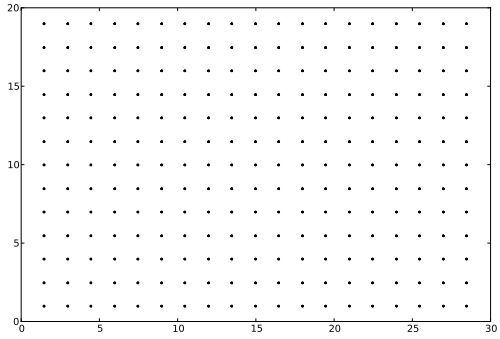

(c) A3: $W_2 = 0.4$, Aligned

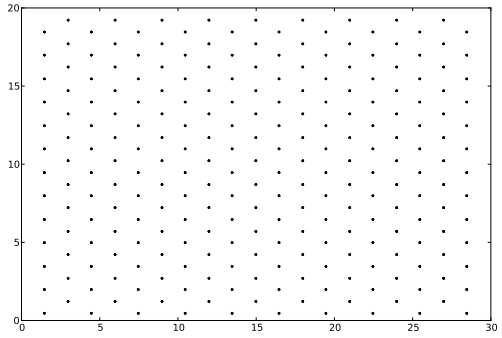

(d) A4: $W_2 = 0.4$, Stag. row

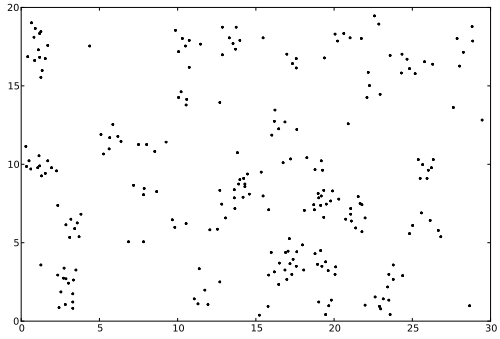

(e) A5: $W_2 = 0.4$, Clustered

Figure 4.2: *Schematics of the five arrangements of cylinders with* $l_\mathrm{A} = 30$ m*:* (a) A1*:* $W_2 = 0.4$*, CSR;* (b) A2*:* $W_2 = 0.4$*, CSR;* (c) A3*:* $W_2 = 0.4$*, Aligned;* (d) A4*:* $W_2 = 0.4$*, in staggered row;* (e) A5*:* $W_2 = 0.4$*, Clustered.*

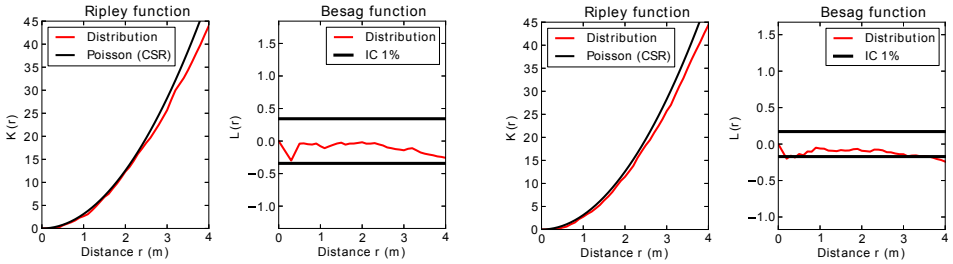

(a) A1: $W_1 = 0.2$, CSR (b) A2: $W_2 = 0.4$, CSR

Figure 4.3: *Ripley function and Besag function for the two arrangements of cylinders* A1 *($W_1 = 0.2$, CSR) and* A2 *($W_2 = 0.4$, CSR).*

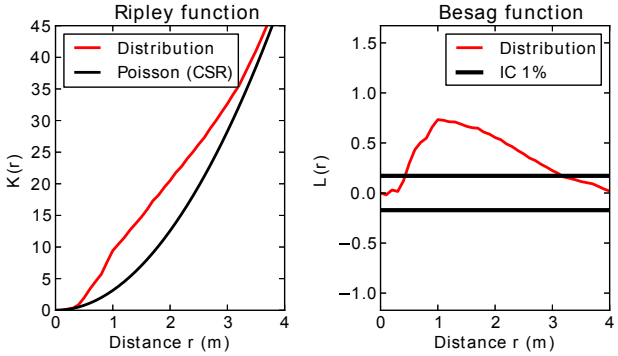

Figure 4.4: *Ripley function and Besag function for the arrangement of cylinders* A5 *($W_2 = 0.4$, clustered).*

4.2.2 TLM simulations parameters

The TLM simulations are performed using the Python/OpenCL-TLM code (Section 2.1.3). The computational domain depicted in figure 4.1 is discretized using a spatial step $\delta l = 0.04$ m. This spatial step corresponds to a sampling frequency equivalent to $\lambda/10$ for the frequency 850 Hz. This corresponds to a time step approximately equal to $\delta t = 6.8\ 10^{-5}$ s. The ground is assumed to be perfectly reflecting for the first sets of simulations, then a ground absorption coefficient is defined. The

absorbing layers are based on the one-way approach (Section 2.2.2.2). A pulse signal is emitted by the line source, consisting in regularly spaced point sources along an axis. The space between two consecutive point sources is set equal to δl. All point sources emit the same Gaussian pulse in phase, which is equivalent to a coherent line source. The pulse propagates through the arrangement of cylinders until reaching the receivers R_0. The simulation duration is set equal to 5.10^{-1} s that is equivalent to twice the propagation distance between the source and the receivers R_0 for the largest domains (*i.e.* arrangements B1 and B2).

The TLM simulations consist in a comparison of the sound pressure levels in decibel, relative to the reference (A0 and B0). The influence of the distribution of cylinders can be studied by comparing the arrangements A2 to A5. The influence of the density can be observed, by comparing either the arrangements A1 and A2, or B1 and B2. Finally, the influence of the length of the arrangement can be investigated looking at the levels obtained for a given density and distribution between the set of arrangement A and B. The duration for these TLM calculations ranges approximately from 5 hours for the smallest domain (*i.e.* A1) to 10 hours for the largest domain (*i.e* B2) using the Python/OpenCL-TLM code on the HPC cluster with 2 NVIDIA Tesla K20 GPU (5 Go GDDR5).

4.3 Results and discussion

In order to compare the results obtained for each arrangement, it is chosen to first look at the time-domain responses at a given node of the TLM network for the set of arrangements A1 to A5. Secondly, the study of the frequency responses obtained for each arrangement is another complementary representation for the analysis of the results.

4.3.1 Time signals

As shown in section 1.3.3.4, reverberant fields in forests is a consequence of multiple scattering caused by tree trunks. This section presents a first investigation on time-domain response of the forest.

The acoustic pressure resulting of the TLM calculations is directly obtained by considering the pressure at a given node. In this study, the pressure generated by the line source is picked up at the central node of the line of receivers R_0. In this configuration, the pulse reaches the receiver after traveling through the arrangement of cylinders. In this sense, the pressure at this node can be seen as the time-domain response resulting from the excitation of an arrangement by the coherent pulse emitted by the line source.

Figures 4.5 shows the linear regressions calculated for the reverberation time RT30 and the early decay time (EDT). These estimations have been made following the international standard ISO 3382-2. The envelope of the impulse response is calculated by means of the Hilbert transform. The energy curves are then filtered using a low pass filter in order to limit the fluctuations. The decay curve is averaged using Schroeder's integrated impulse method [132]. The results are summarized in table 4.2. Although the dispersion is relatively low over all the arrangements, it can

be said that the periodic arrangements present both the lowest RT30 and the lowest EDT values. As a general observation, the differences between the RT30 and the EDT are relatively small for all arrangements.

Name of the arrangement	A1	A2	A3	A4	A5
Reverberation time RT30 (ms)	584	539	485	504	526
Early Decay Time EDT (ms)	308	355	226	180	320

Table 4.2: *Reverberation times and early decay times for the arrangements of cylinders A1 to A5.*

In addition, figures 4.6 and 4.7 show the wavefront propagation inside respectively the arrangement A2 (*i.e.* CSR distribution) and A3 (*i.e.* periodic aligned distribution). The top view is an horizontal slice taken at 2 m high above the ground; the side view corresponds to a snapshot of the instantaneous pressure taken in the middle of the domain along the vertical axis. Each view is taken at the iteration 728 that corresponds to the time $t_{\mathrm{it}-728} = 4.94\ 10^{-2}$ s. At this time, the initial wavefront is still inside the arrangement of cylinders, about 17 m from the line source. The pulse emitted by the line source is traveling through the arrangements of cylinders showing distinct scattering patterns between the random and periodic distributions. It can be seen from the top views that the random distribution presents a superposition of concentric circles of pressures centered around the cylinders, whereas the periodic aligned distribution presents symmetric line of pressure between the row of cylinders.

At this step, it is difficult to go further in the investigation of the reverberation produced by forests. Firstly, the literature (Section 1.3.3.4) does not give sufficient results that could be compared to the RT30 or EDT values obtained here. Secondly, it has not been possible to observe significantly different temporal behaviors from an arrangement to another. However, frequency analysis of reverberation (not presented here) could give more interesting results.

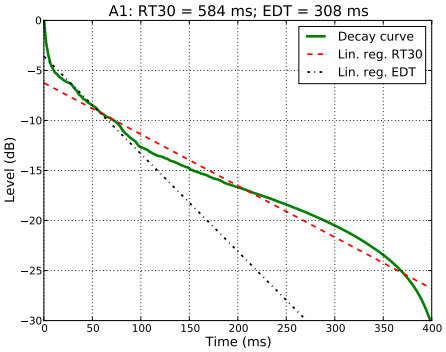

(a) A1: $W_1 = 0.2$, CSR

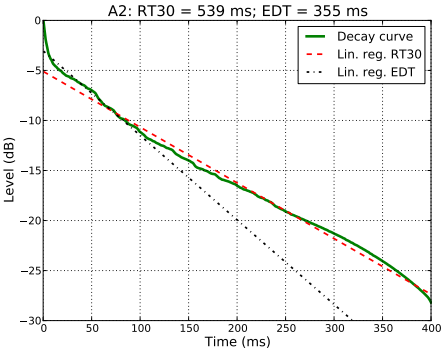

(b) A2: $W_2 = 0.4$, CSR

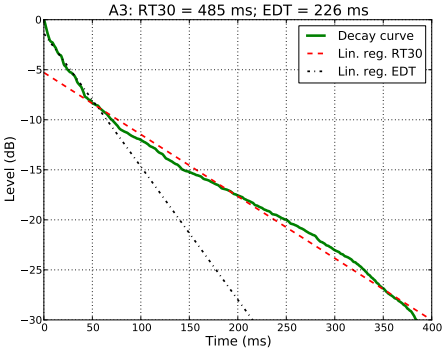

(a) A3: $W_2 = 0.4$, Aligned

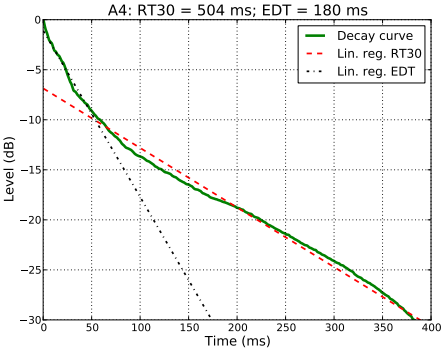

(b) A4: $W_2 = 0.4$, Stag. row

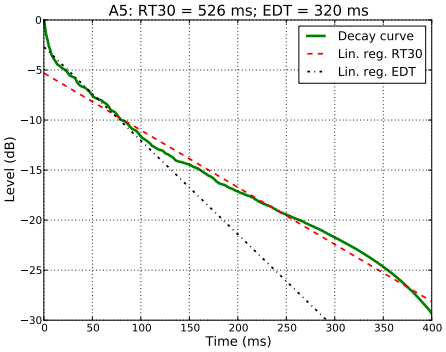

(a) A5: $W_2 = 0.4$, Clustered

Figure 4.5: *Linear regressions for the calculation of the RT30 and the EDT for the five arrangements of cylinders:* (a) A1 *($W_2 = 0.4$, CSR);* (b) A2 *($W_2 = 0.4$, CSR);* (c) A3 *($W_2 = 0.4$, aligned);* (d) A4 *($W_2 = 0.4$, in staggered-row);* (e) A5 *($W_2 = 0.4$, clustered).*

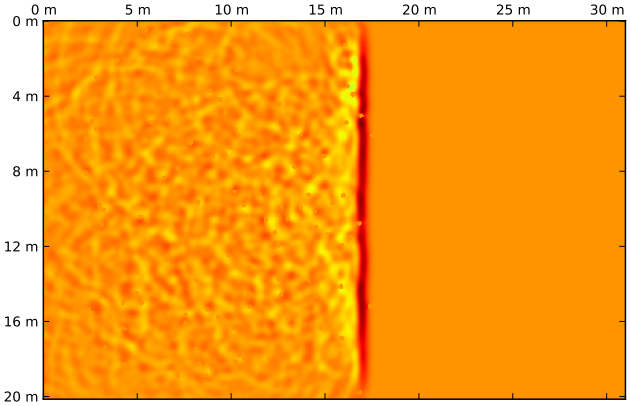

(a) Top view

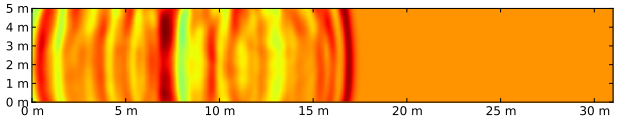

(b) Side view

Figure 4.6: *Wavefronts propagation (from the left to the right) at iteration 728 ($t_{\mathrm{it}-728} = 4.94\ 10^{-2}$ s) inside arrangement* A2 *($W_2 = 0.4$, CSR):* (a) *top view;* (b) *side view.*

4.3.2 Frequency responses

It is important to note that significant fluctuations of the sound pressure levels (not presented here) are observed along a given line of receivers such as R_0. Therefore, at each line of receivers, the pressure is averaged over the 50 point receivers that constitute the line. The levels presented in this section are relative to the reference line, *i.e.* it could be seen as the difference (*i.e.* an attenuation) between the level in front of an arrangement of cylinders (*i.e.* line R_{REF}) and the level after the pulse travels through the arrangement (*i.e.* line R_0).

4.3.2.1 Influence of the distribution

Figure 4.8 shows the frequency responses obtained with the four different distributions A2 to A5 (Figure 4.2). It can be seen that the periodic distributions represented by the arrangements A3 and A4 give spectra with stop and pass bands. This kind of frequency pattern reminds the phenomena that is well known in sonic crystal theory. However, it is important to note that the filling fractions [133] $F_{f-\mathrm{aligned}} = \pi a^2/d^2$ or $F_{f-\mathrm{stag.row}} = \pi(2a)^2/2\sqrt{3}d^2$, where a is the radius of the cylinder and d the minimum distance between two consecutive cylinders, are about $F_{f-\mathrm{aligned}} = 0.014$ and $F_{f-\mathrm{stag.row}} = 0.016$, whereas, for typical sonic crystals, abso-

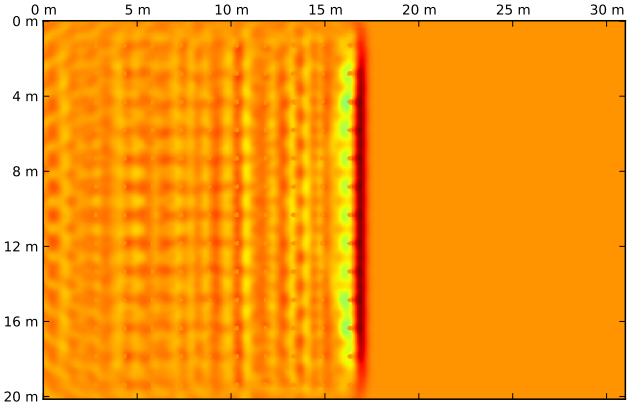

(a) Top view

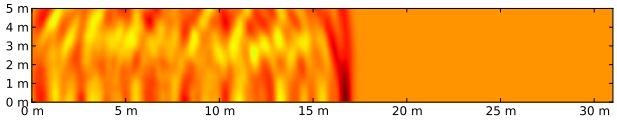

(b) Side view

Figure 4.7: *Wavefronts propagation (from the left to the right) at iteration 728* ($t_{\mathrm{it}-728} = 4.94\ 10^{-2}$ s*) inside arrangement* A3 *(*$W_2 = 0.4$*, periodic aligned:* (a) *top view;* (b) *side view.*

lute band gaps are observed for $0.4 < F_f < 0.6$ [133]. Apparently, pseudo-band gaps can still be observed for such low value of filling fractions, as shown in figure 4.8, with the arrangements A3 and A4. The random (CSR) distribution and the clustered distribution (A2 and A5) are almost equivalent and present an attenuation spectrum that steadily decreases with increasing frequency.

The global attenuations presented in figure 4.8(b) are calculated from the pulse pressure at each line on the frequency range 100 Hz to 1000 Hz. Regarding the global attenuations, it can be noticed that, for this frequency range, the empty array A0 presents an attenuation almost equal to the arrangement A4, around -9 dB. In this case, multiple scattering from A4 could be considered as less important in terms of attenuation.

As shown in this section for the same density and the same length, the CSR and the clustered distributions provide the largest attenuations. Although the clustered distribution might be not as easy to reproduce, the CSR distribution is accurately defined and assessed. With the aim of building an efficient arrangement of cylinders that provides the largest attenuation, it might be interesting to use randomly spaced arrangement of cylinders.

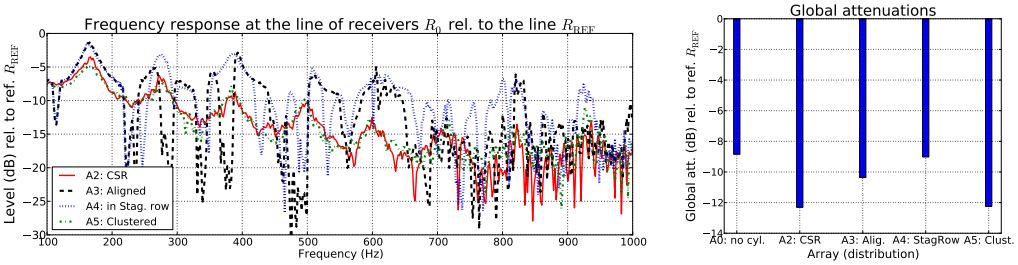

(a) (b)

Figure 4.8: *Influence of the distribution: comparison of (a) the frequency responses and (b) the global attenuations obtained at the line R_0 relative to the line R_{REF} for four different distributions:* A2 *(CSR),* A3 *(aligned),* A4 *(in staggered row),* A5 *(clustered).*

4.3.2.2 Influence of the density

Figure 4.9 shows the frequency responses obtained with the two densities $W_1 = 0.2$ and $W_2 = 0.4$ for $l_A = 30$ m and $l_B = 40$ m. Firstly, it can be seen that the spectrum corresponding to the highest density W_2 presents larger fluctuations, especially at high frequency. This is caused by multiple scattering that is more present for higher density of scatterers. The ground effect can be observed with the arrangement A0, where the dip at 700 Hz corresponds to the first destructive interference for the given distance and height of the source and receiver. At low frequency (100 Hz - 150 Hz), the sound attenuations are of the same level. From 200 Hz, the highest density W_2 shows higher attenuation. This difference tends to increase with increasing frequency. The global attenuation increase is slightly more important between the arrangements A1 and A2 (about -2.2 dB) than for the arrangements B1 and B2 (about -1.7 dB). This observation is confirmed and explained with more details in section 4.3.2.3, where the influence of the arrangement length is studied.

Even though only few densities are tested in this section, as expected, the largest attenuation are obtained using the highest density of cylinders.

4.3.2.3 Influence of the length

Figure 4.10 shows the global attenuations relative to the reference line R_{REF} as a function of the arrangements length $l_A = 30$ m (A1 and A2), and $l_B = 40$ m (B1 and B2). It is shown that the global attenuations for the empty array A0 and B0 are around the -9 dB for both lengths. Although for a given density W_1 or W_2, the attenuation increases with the length of the arrangements, it can be noticed that this increase is less marked for W_2, where $\Delta_{l_A - l_B} Att_{W_1} = -2.1$ dB compared to $\Delta_{l_A - l_B} Att_{W_2} = -1.5$ dB. This trend is confirmed when looking at the global attenuations relative to the ground (Figure 4.10(b)), where $\Delta_{l_A - l_B} Att_{W_1} = -2.5$ dB compared to $\Delta_{l_A - l_B} Att_{W_2} = -1.5$ dB. This could be caused by the important density W_2 (*i.e.* large number of scatters) that tends to reduce the relative attenuation between two lengths. This would mean that for higher densities, the attenuation difference

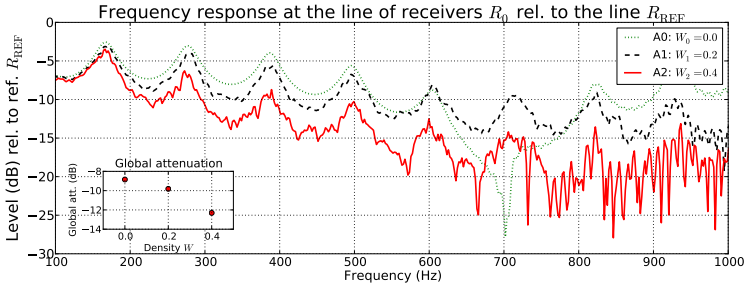

(a) A1 ($l_A = 30$ m, $W_1 = 0.2$, CSR) and A2 ($l_A = 30$ m, $W_2 = 0.4$, CSR)

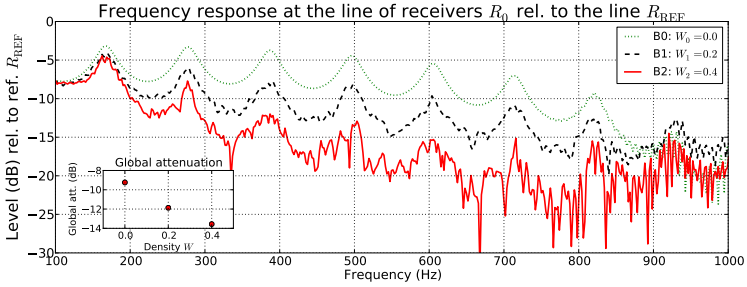

(b) B1 ($l_B = 40$ m, $W_1 = 0.2$, CSR) and B2 ($l_B = 40$ m, $W_2 = 0.4$, CSR)

Figure 4.9: *Influence of the density: comparison of the frequency responses obtained at the line R_0 relative to the line R_{REF} for 4 arrangements:* (a) *A1 and A2,* (b) *B1 and B2.*

between two arrangement lengths would tend to zero as most of the incident wave would be backscattered. This could be shown in more details by studying more densities and larger arrays. Comparing the global attenuation relative to ground effect obtained from the empty arrays A0 and B0, it is interesting to note that the same attenuation levels is achieved with the array A2 and B1, showing that increasing the density of the smaller arrangement would tend to increase the attenuation levels in a larger extent than increasing the length from $l_A = 30$ m to $l_B = 40$ m.

Although the largest attenuation is achieved with the arrangement B2 that corresponds to the largest length and highest density, it should be noticed that comparing the global attenuations between A2 and B1, the increase in the length (*i.e.* increase of 10 m here) is not as efficient as the doubling of the density in this case.

4.3.2.4 Influence of the ground absorption

Due to numerical problems using such large computational domains, it has not been possible to implement the ground effect using an impedance surface model. Therefore, a simple real reflection coefficient R^n is used to simulate the absorption of the ground. This reflection coefficient is implemented through a TLM connexion law as:

$$ {}_{t+\delta t}I^n_{(i,j)} = R^n \times {}_tS^n_{(i-1,j)}, \tag{4.1} $$

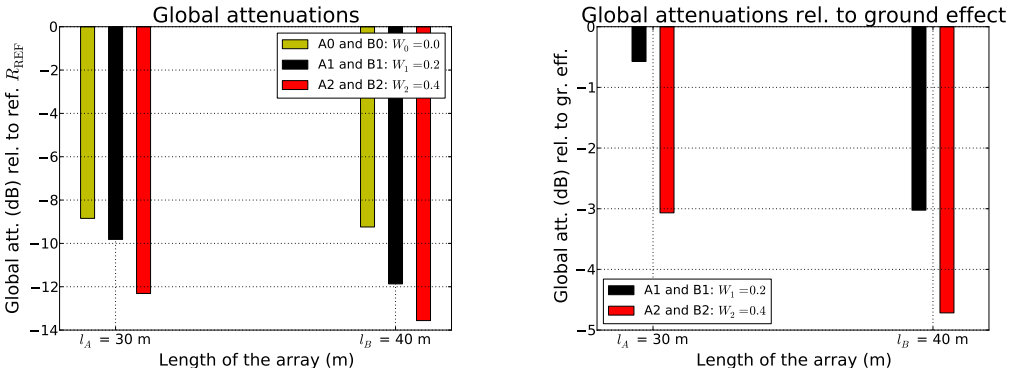

Figure 4.10: *Global attenuations relative to the reference* R_{REF} *as a function of the length of the arrangements* $l_A = 30$ m *for A1 and A2, and* $l_B = 40$ m *for B1 and B2:* (a) *comparison between the densities* $W_0(nocylinder)$, W_1, W_2*;* (b) *attenuation caused by the scattering relative to the ground effect.*

where the index n corresponds to the TLM branch that is normal to the boundary. In this case, the same branch is used for both the incident and scattered pressure, which leads to very low computational cost using this boundary condition compared to the surface impedance condition proposed by Guillaume *et al.* [60].

This section aims to show the influence of ground absorption on the frequency responses and the global attenuations, using four values of reflection coefficients $\mathrm{R} = [1.0,\ 0.7,\ 0.5,\ 0.3]$. Here, the ground reflection coefficient does not depend on the incident angles. In this case $\mathrm{R} = 1$ corresponds to a perfectly reflecting ground, and $\mathrm{R} = 0.3$ represents the most absorbent ground in this study. For the need of this study, measurements above grassland and forest ground have been carried out using the same procedure as the one described by Hess *et al.* [134]. Figure 4.11 shows the variations of the reflection coefficient for three angles. The measured forest ground reflection coefficient ranges from 0.9 to 0.5 in the frequency range 100 Hz to 1000 Hz. Although the reflection coefficients used for the present parametric study are constant along the frequency, the values $\mathrm{R} = 0.5$ to 1.0 selected for the TLM simulations are in relation with those measured inside a forest.

Two arrangements of cylinders are chosen to perform the TLM simulations: A2 ($W_2 = 0.4$ and a CSR distribution) and A3 ($W_2 = 0.4$ and a periodic aligned distribution). Figure 4.12 shows the four frequency responses that correspond to the four reflection coefficients for the arrangements A2 and A3. Generally speaking, it can be seen that the global attenuation levels increase when the reflection coefficient value decreases. This increase in attenuation is more pronounced at low frequency, whereas from 800 Hz to 1000 Hz, the four curves are almost overlapping. The constant reflection coefficients used in the TLM simulations leads to a ground effect that is more marked at low frequency (negative offset). At higher frequency, the ground effect is less present and multiple scattering remains the most present

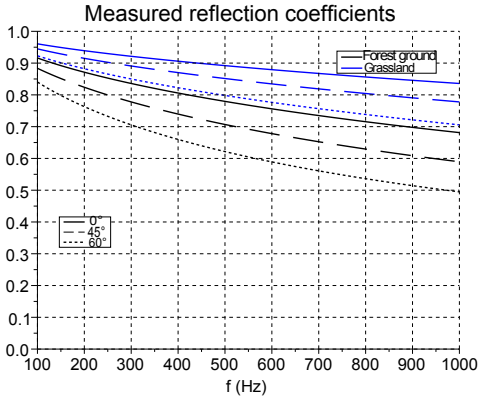

Figure 4.11: *Measured grassland and forest ground reflection coefficients as a function of the frequency for three different incident angles.*

phenomena. Compared to the measured reflection coefficient along frequency (Figure 4.11), it can be said that the constant value for the absorption tends to overestimate the attenuation at low frequency. Therefore, the ground effect is here overestimated. However, it can be observed that the reflection coefficient value does not affect the interference pattern caused by multiple scattering. Figure 4.13 shows a comparison of the global attenuation levels for the four ground reflection coefficient values. It is shown that the difference between the two arrangements is of the same order for each reflection coefficient value, *i.e.* around -1.7 dB.

As expected, the higher ground absorption gives the largest attenuation. However, the parameter that influences the most significantly the global attenuation levels in this study remains the cylinder distribution for this frequency range.

4.3.2.5 Influence of the position of the receiver line inside the arrangement of cylinders

This section aims to look at the global attenuation levels inside a given arrangement of cylinders. Eight lines of receivers are placed each 5 m inside the arrangements B2 and B0. Figure 4.14 shows the global attenuations as a function of the distance inside the arrangement from 5 m to 40 m. In the empty array B0, the ground effect is the only effect, whereas for B2 both ground effect and multiple scattering influence the global attenuations. It can be seen that the global attenuations increase with the distance, except for B0 at 15 m and 20 m, where constructive interferences from the ground effect can be responsible for this reinforcement of the levels. This phenomenon is not observed with the arrangement B2, where the multiple scattering, added to ground effect, tends to gradually increase the global attenuation along the distance. Looking at the multiple scattering contribution relative to the ground effect (Figure 4.14(b)), it can be seen that multiple scattering is preponderant at the distance of 20 m. For each distance, the multiple scattering contribution is 50% to 80% lower than the ground effect contribution.

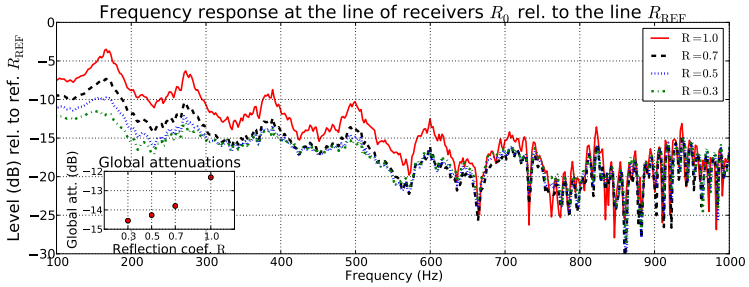

(a) A2: $W_2 = 0.4$, CSR

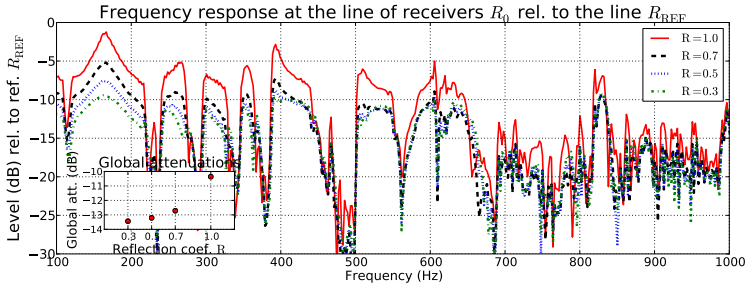

(b) A3: $W_2 = 0.4$, Aligned

Figure 4.12: *Influence of the ground reflection coefficient* R*: comparison of the frequency responses obtained at the line* R_0 *relative to the line* R_{REF} *for four values of* $\mathrm{R} = [1.0,\ 0.7,\ 0.5,\ 0.3]$*:* (a) ***A2*** *(*$W_2 = 0.4$***, CSR)*** *and* (b) ***A3*** *(*$W_2 = 0.4$***, Aligned).***

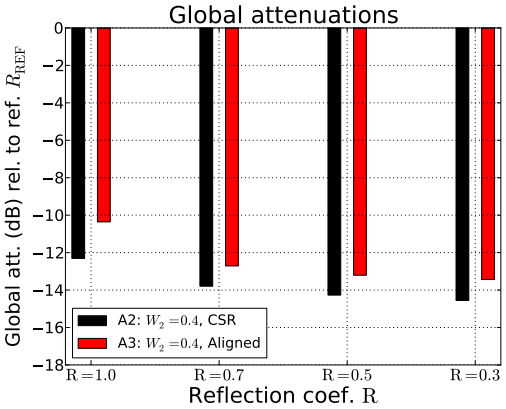

Figure 4.13: *Comparison between the arrangements A2 (*W_2*, CSR) and A3 (*W_2*, Aligned) of the global attenuation levels at the line* R_0 *relative to the line* R_{REF}*, for four ground reflection coefficient values* $\mathrm{R} = [1.0,\ 0.7,\ 0.5,\ 0.3]$.

As expected the largest attenuation is obtained at larger distance. However, it can be noticed that, in the present configuration, the ground effect plays a major

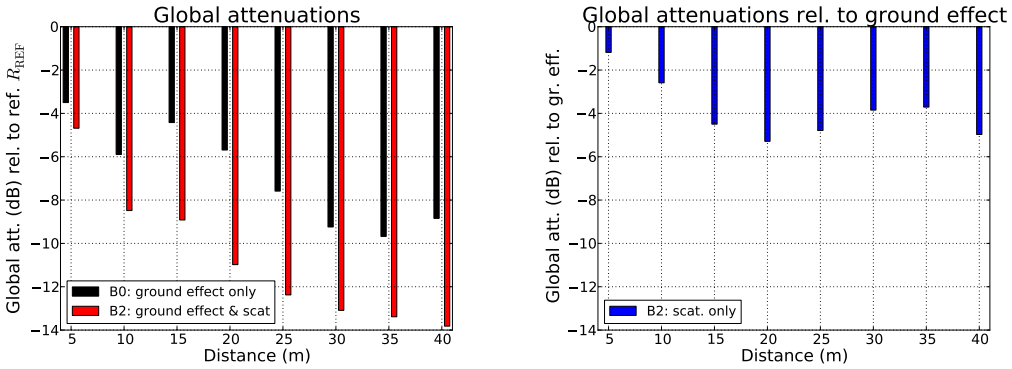

Figure 4.14: *Global attenuations relative to the reference R_{REF} as a function of the distance between the reference line R_{REF} and the line of receivers inside the arrangement:* (a) *comparison between the ground effect only and the ground effect with scattering,* (b) *attenuation caused by multiple scattering relative to ground effect.*

role. Thus, regarding the source and receiver position, the attenuation can be optimized when the first destructive interference (*i.e.* ground dip) is inside the frequency range of interest.

4.4 Conclusion

In the present chapter, the TLM method has been used to investigate the impact of a simplified forest on sound propagation. This simplified forest is made of perfectly reflecting cylinders placed normal to the ground. The distribution, the density, the length of the arrangement of cylinders and the receiver line position inside the arrangement are the parameters of interest in this study.

The numerical results have shown that, even if the density is low compared to sonic crystals cases, pseudo-band gaps can still be observed in the frequency range 100 Hz - 1000 Hz. Therefore, the two periodic arrangements show frequency responses where the gap are pronounced, whereas the CSR and clustered distribution have a reduced dynamic range. In terms of global attenuation levels, the periodic arrangements present lower attenuation than the two CSR and clustered distributions.

As expected, it has been observed that the increase in density induces an increase in attenuation. Similarly the increase in length of the arrangement induces an increase in attenuation. However, for the two lengths and the two densities considered in this study, it is shown that the attenuation levels are more sensible to the density than the length. Further investigations are needed to confirmed on a larger range of lengths and densities.

The influence of the ground reflection coefficient is mostly observed at low frequency where the attenuation levels are larger when the reflection coefficient is reduced. However, comparing the attenuation levels between a random and periodic distributions, for four different ground reflection coefficients, suggests that distribution remains slightly more important, in this configuration (*i.e.* for these source and receiver positions), in the view to achieve high attenuation levels.

As expected, changing the position of the receiver line inside a given arrangement has shown that the attenuation increases with the distance. Inside an empty area the attenuation levels can be slightly modified by the presence of the ground dip. The contribution of multiple scattering by reflecting cylinders on the attenuation levels is relatively low compared to ground effect, especially at large distances.

In conclusion, an efficient arrangement of cylinders (*i.e.* *"a forest barrier"*) in terms of attenuation, can be defined by a narrow length if the density of scatterers is large and if the scatterers are randomly located. The ground effect can be used as an additional mean to reinforce the attenuation.

As an interesting outline, the sensitivity of each parameter studied in this chapter could be investigated by simulating more arrangements. Furthermore, it would be interesting to model the ground using a surface impedance model that would result in a more realistic ground effect. In practice, comparing the insertion loss between a pasture field and a forest, would give rise to more absorption from the ground, since forest ground generally present lower mean flow resistivity that a pasture ground. A comparison between this two cases (*i.e.* pasture field/forest) would give more insight on the impact of forest on noise level attenuation.

CONCLUSION

This document studied sound propagation inside forested areas using the TLM method. More generally, the present work aimed at giving more insight on the impact of forest on noise levels. As reminded in the general introduction, one of the initial purposes of this work was to develop a numerical method that can predict the excess attenuation of forests and determine whether forests can be used as an efficient protection from road traffic noise. Furthermore, accurate noise level prediction could contribute to both the identification of quiet areas and the protection of biodiversity inside forests. Through the literature review presented in chapter 1, it has been shown that ground, multiple scattering and meteorological effects constituted the three main parameters that can influence the sound propagation in such areas. Although the TLM method has been used in the past for the simulation of outdoor sound propagation, the forest remains a complex propagation medium that requires the investigation of acoustical phenomena such as multiple scattering. In this sense, the choice of the TLM method can also be justified by the fact that it naturally takes into account scattering phenomena due to the definition of the TLM-network properties (*i.e.* the scattering matrix). From previous works on outdoor acoustic simulation using the TLM method, it has been noticed that the only way to limit the simulation domain is to use large empirically-defined absorbing layers. The large size of this absorbing layers constitutes a burden that required extensive computational resources. Thus, the need of theory-based efficient absorbing layers constituted also an important objective beforehand coping with large propagation domain including a forest.

The work on the absorbing layers adapted to the TLM method, which has been proposed in chapter 2, has given rise to an absorbing matched layer (AML) formulation that relies on the lossy wave equation. The design of the numerical simulations and the representation of the results as a function of space can be seen as interesting features for future studies on absorbing layers efficiency. Compared to the existing absorbing layer based on empirical formulation of the TLM connexion laws, the proposed AML relies on the scattering matrix. Although the proposed AML formulation is not an exact perfectly matched layer (PML) formulation, it is shown that, after optimization, the proposed AML presented better performances than the existing layer for a wide range of incident angles. In the present study, the main link between acoustics theory and the TLM method starts from the wave

equation. An exact adaptation of the PML theory to the TLM method would have been rigorously possible if the method could be written using the momentum and mass conservation equations. Thus, the need of straightforward relations between the TLM method and the momentum and mass conservation equations remains of prime importance for future developments of this numerical method.

In order to study the sound propagation inside a forest using the TLM method, it has first been necessary to evaluate the ability of the numerical model to simulate single and multiple scattering of acoustic waves by perfectly reflecting cylinders. At first, 2D simulations were compared to analytical solutions proposed in the literature. Then, for 3D multiple scattering above a ground, as observed in forests, as no analytical solutions have been found yet, the TLM results were compared to measurement on scale models. All comparisons between the TLM simulations, the analytical solutions and/or the measurements data have shown a good agreement for both 2D and 3D cases. In order to link the acoustic simulations to forest spatial structure analysis, two point processes have been used for the placement of the scatterers. These mathematical tools have been used to define random distributions but can also be used to reproduce more complicated forest structures (*e.g.* clustered or dispersed distributions). The validation of multiple scattering above a large surface of impedance ground however still needs some improvements of the impedance condition in the numerical code. Nevertheless, this study of single and multiple scattering have shown that the TLM method is well suited for the prediction of such phenomena.

In order to give an overview of the impact of a forest on acoustic levels, it has been chosen to use the TLM method as a numerical tool for the prediction of sound attenuation caused by ground effect and multiple scattering. Thus, chapter 4 has presented a parametric study of sound propagation through forests, where forested areas were modeled by arrangements of cylinders placed normal to the ground. Although the trees were modeled by cylinders, the TLM simulations have given the main trends on the influence of the scatterers distribution, density of scatterers, length of the forest area and ground absorption. For example, it has been observed that the arrangement where the cylinders were randomly located with a high density (0.4 cylinders per square meter) and a relatively large ground absorption coefficient (ground reflection coefficient between 0.5 and 0.7) give the highest global attenuation. Furthermore, the attenuations that have been obtained with the random and clustered distributions have shown similarities. In a first approach, the use of simple random distributions for future acoustic simulations could be seen as an interesting alternative to the definition of more complicated clustered or dispersed forest distributions. The last chapter can be seen as the beginning of the TLM application to forests. Interesting perspectives can be extracted from this first step, such as the significant parameters for the design of an efficient forest strip in term of attenuation levels. A deeper investigation on the sensitivity of each parameter would give more insight. From this understanding, simplified laws linked to forest properties can be developed in order to be included within engineering prediction methods, such as the french standard method (NMPB), the CNOSSOS-EU

approach, or the ISO 5613-2 standard.

The present work can be seen as a starting point for further developments of the TLM method for the prediction of sound propagation in forests. For instance, the impedance of tree trunk could be taken into account. Experimental study could be carried out using impedance tube for the measurement of the bark mean flow resistivity. Then the estimated surface impedance of tree trunk could be used in the TLM simulations. An equivalent intermediate medium placed on top of the trunks could be used to simulate the canopy. This medium would aim at simulating the additional scattering from the branches and the leaves. Another perspective consists in the implementation of meteorological effects specific to the presence of forests. Previous work has been carried on wind and temperature profiles in the TLM method [48] that could be used for the application of the TLM in forests.

Noise mapping constitutes an interesting way for the identification of quiet areas [28]. In the long term, accurate noise predictions in presence of forests would enhance the accuracy of current noise mapping in urban and interurban forested areas. This would contribute to the protection of quiet areas.

Finally, the use of the TLM method for the prediction of sound propagation inside forests could provide deeper understanding on forest species communication process. Furthermore, accurate noise level prediction in forests can be seen as an interesting tool for the management of noise exposure for forest species. In a certain extent, this could contribute to the preservation of biodiversity in forested areas.

Appendix

Appendix A

TLM DESCRIPTION FOR ALL SPATIAL DIMENSIONS

In the main part of this document the TLM method has been described for two-dimensional (2D) propagation cases. The aim of this appendix is to generalize the TLM description to any n_d-dimensional cases through the parameter n_d.

A.1 Notations for a generalized TLM description

The parameter n_d denotes the spatial dimension of the TLM model. The discrete coordinate notation can be condensed using the index $\mathbf{r}$, which corresponds to:

$$\mathbf{r} = \begin{cases} (i,j) & \text{for 2D,} \\ (i,j,k) & \text{for 3D.} \end{cases}$$

The introduction of this notations (n_d and $\mathbf{r}$) extend the scope of the TLM description proposed in section 2.1.

A.2 Generalized TLM description for heterogeneous and dissipative medium

A.2.1 Scattering process

Equation (2.4) which describe the scattering process can be rewritten using the index $\mathbf{r}$:

$${}_t\mathbf{S}_\mathbf{r} = {}_t\mathbf{D}_\mathbf{r}\ {}_t\mathbf{I}_\mathbf{r}, \tag{A.1}$$

where the scattering matrix ${}_t\mathbf{D}_\mathbf{r}$ that can be derived using the definition of the reflection and transmission coefficient expressed for each branch. Firstly, for the main branches (*i.e.* branch 1 to 4 for 2D TLM-network), the reflection and transmission coefficients are:

$${}_tR^n_\mathbf{r} = -\frac{-\eta_\mathbf{r} + \zeta_\mathbf{r} + 2(n_d - 1)}{\eta_\mathbf{r} + \zeta_\mathbf{r} + 2n_d}, \tag{A.2a}$$

$$ {}_tT_{\mathbf{r}}^{n} = \frac{2}{\eta_{\mathbf{r}} + \zeta_{\mathbf{r}} + 2n_d}. \tag{A.2b} $$

Secondly, if the branch corresponds to the heterogeneity branch (*i.e.* branch 5 for 2D TLM-network), the reflection and transmission coefficients are:

$$ {}_tR_{\mathbf{r}}^{N} = -\frac{-\eta_{\mathbf{r}} + \zeta_{\mathbf{r}} + 2n_d}{\eta_{\mathbf{r}} + \zeta_{\mathbf{r}} + 2n_d}, \tag{A.3a} $$

$$ {}_tT_{\mathbf{r}}^{N} = \frac{2\eta_{\mathbf{r}}}{\eta_{\mathbf{r}} + \zeta_{\mathbf{r}} + 2n_d}. \tag{A.3b} $$

Finally, if the branch is the artificial absorption branch (*i.e.* branch 6 for 2D TLM-network), the reflection and transmission coefficients are equal to zero:

$$ {}_tR_{\mathbf{r}}^{N+1} =_t T_{\mathbf{r}}^{N+1} = 0. \tag{A.4} $$

Therefore, the scattering matrix for wave propagation in an heterogeneous and dissipative n_d-dimensional TLM-network is given by:

$$ {}_t\mathbf{D}_{\mathbf{r}} = \frac{2}{\eta_{\mathbf{r}} + \zeta_{\mathbf{r}} + 2n_d} \, {}_t \begin{bmatrix} a & 1 & . & 1 & \eta \\ 1 & a & . & 1 & \eta \\ . & . & . & . & . \\ 1 & 1 & . & a & \eta \\ 1 & 1 & . & 1 & b \end{bmatrix}_{\mathbf{r}}, \tag{A.5} $$

with

$$ a_{\mathbf{r}} = -\frac{\eta_{\mathbf{r}}}{2} - \frac{\zeta_{\mathbf{r}}}{2} - (n_d - 1), \tag{A.6a} $$

$$ b_{\mathbf{r}} = \frac{\eta_{\mathbf{r}}}{2} - \left(\frac{\zeta_{\mathbf{r}} - 2n_d}{2} \right). \tag{A.6b} $$

Relations (A.1) and (A.5) give scattered pulses in relation to incident pulses at a node position $\mathbf{r}$ as follows:

$$ \sum_{m=1}^{4} {}_tS_{\mathbf{r}}^{m} + {}_tS_{\mathbf{r}}^{5} = \frac{\eta_{\mathbf{r}} - \zeta_{\mathbf{r}} + 2n_d}{\eta_{\mathbf{r}} + \zeta_{\mathbf{r}} + 2n_d} \left[\sum_{n=1}^{2n_d} {}_tI_{\mathbf{r}}^{n} + \eta_{\mathbf{r}} \, {}_tI_{\mathbf{r}}^{N} \right], \tag{A.7} $$

where N denotes the heterogeneity branch number: $N = 2n_d + 1$.

A.2.2 Acoustic pressure

The superposition principle gives the pressure at a given node position as follows:

$$ {}_tp_{\mathbf{r}} = \frac{2}{\eta_{\mathbf{r}} + \zeta_{\mathbf{r}} + 2n_d} \left[\sum_{n=1}^{2n_d} {}_tI_{\mathbf{r}}^{n} + \eta_{\mathbf{r}} \, {}_tI_{\mathbf{r}}^{N} \right]. \tag{A.8} $$

Equation (A.7) is rewritten using equations (A.1) and (A.8):

$$ {}_tS_{\mathbf{r}}^{n} = {}_tp_{\mathbf{r}} - {}_tI_{\mathbf{r}}^{n}, \tag{A.9} $$

A scattered pulse from branch n is expressed as a function of the acoustic pressure at corresponding node $\mathbf{r}$ and of the incident pulse in the same branch.

A.2.3 Connexion laws

At a given node position $\mathbf{r}$, each scattered pulse ${}_tS^m$ cover the discretized distance δl during the time δt and becomes an incident pulse ${}_{t+\delta t}I^n$ at an adjacent node. For the node position $\mathbf{r}$ this is written as:

$$ {}_{t+\delta t}I^n_{\mathbf{r}} = {}_tS^m_{\mathbf{r}^{\pm}_n}, \tag{A.10a} $$

$$ {}_{t+\delta t}I^N_{\mathbf{r}} = {}_t\, S^N_{\mathbf{r}}, \tag{A.10b} $$

with

$$ \left\{ \begin{array}{c} n \\ \mathbf{r}^{\pm}_n \end{array} \right\} = \left\{ \begin{array}{l} \left\{ \begin{array}{c} m-1 \\ \mathbf{r}^{+} \end{array} \right\} \text{if } m \text{ is even number}, \\ \\ \left\{ \begin{array}{c} m+1 \\ \mathbf{r}^{-} \end{array} \right\} \text{if } m \text{ is odd number}, \end{array} \right. $$

and

$$ \mathbf{r}^{\pm}_n = \left\{ \begin{array}{l} (i \pm 1, j, k), \text{for } n = 1 \text{ or } 2, \\ (i, j \pm 1, k), \text{for } n = 3 \text{ or } 4, \\ (i, j, k \pm 1), \text{for } n = 5 \text{ or } 6. \end{array} \right. $$

A.2.4 TLM celerity

The TLM celerity for heterogeneous and dissipative medium simulation can be generalized as follows:

$$ c_{\text{TLM}} = \sqrt{\frac{2}{\eta_{\mathbf{r}} + 2n_d}}\, c, \tag{A.11} $$

where $c = \delta l / \delta t$ and $\eta_{\mathbf{r}}$ is the heterogeneity term. For propagation in homogeneous media, *i.e.* $\eta_{\mathbf{r}} = 0$, the TLM celerity is given by:

$$ c_{\text{TLM}} = \frac{c}{\sqrt{n_d}}, \tag{A.12} $$

where c_{TLM} is set equal to the celerity of an acoustic wave in homogeneous media (c_0). This gives a general equation for c:

$$ c = \sqrt{n_d} c_0. \tag{A.13} $$

Equation (A.13) can be related to the Courant-Friedrich-Levy (CFL) stability criterion as shown in section 2.1.2.5, which is a necessary condition for the model stability.

BIBLIOGRAPHY

[1] World Health Organization, "Environmental health inqualities in Europe," tech. rep., WHO European Centre for Environment and Health, 2012.

[2] B. Berglund, T. Lindvall, and D. H. Schwela, "Guidelines for community noise," in *World Health Organization*, 1999.

[3] G. Martin-Houssart and C. Rizk, "Mesurer la qualité de vie dans les grandes agglomérations," *INSEE Première*, vol. 868, pp. 1–4, 2002.

[4] World Health Organization, "Burden of disease from environmental noise," tech. rep., WHO European center for Environment and Health, 2011.

[5] W. Babisch, "Cardiovascular effect of noise," *Noise Health*, vol. 13, pp. 201–204, 2011.

[6] G. Dubois, J. Cesbron, H. Yin, and F. Anfosso-Lédée, "Numerical evaluation of tyre/road contact pressures using multi-asperity approach," *Int. J. Mech. Sciences*, vol. 54, pp. 84–94, 2012.

[7] D. J. Thompson and C. J. C. Jones, "A review of the modelling of wheel/rail noise generation," *J. Sound Vib.*, vol. 231, pp. 519–536, 2000.

[8] U. J. Kurze, "Noise reduction by barriers," *J. Acoust. Soc. Am.*, vol. 55, pp. 504–518, 1974.

[9] D. Aylor, "Sound transmission through vegetation in relation to leaf area density, leaf width, and leaf breadth of canopy," *J. Acoust. Soc. Am.*, vol. 51, pp. 411–414, 1972.

[10] D. Aylor, "Noise reduction by vegetation and ground," *J. Acoust. Soc. Am.*, vol. 51, pp. 197–205, 1972.

[11] K. V. Horoshenkov, A. Khan, and H. Benkreira, "Acoustic properties of low growing plants," *J. Acoust. Soc. Am.*, vol. 133, pp. 2554–2565, 2013.

[12] L. Ding, T. Van Renterghem, D. Botteldooren, K. Horoshenkov, and A. Khan, "Sound absorption of porous substrates covered by foliage: Experimental results and numerical predictions," *J. Acoust. Soc. Am.*, vol. 134, pp. 4599–4609, 2013.

[13] T. Van Renterghem, E. Salomons, and D. Botteldooren, "Parameter study of sound propagation between city canyons with a coupled fdtd-pe model," *Appl. Acoust.*, vol. 67, pp. 487–510, 2006.

[14] M. Hornikx and J. Forssén, "Noise abatement schemes for shielded canyons," *Appl. Acoust.*, vol. 70, pp. 267–283, 2009.

[15] T. Van Renterghem and D. Botteldooren, "Reducing the acoustical façade load from road traffic with green roofs," *Building and Environment*, vol. 44, pp. 1081–1087, 2009.

[16] T. Van Renterghem and D. Botteldooren, "In-situ measurements of sound propagating over extensive green roofs," *Building and Environment*, vol. 46, pp. 729–738, 2011.

[17] M. Connelly and M. Hogdson, "Experimental investigation of the sound transmission of vegetated roofs," *Appl. Acoust.*, vol. 74, pp. 1136–1143, 2013.

[18] N. H. Wong, A. Y. K. Tan, P. Y. Tan, K. Chiang, and N. C. Wong, "Acoustics evaluation of vertical greenery systems for building walls," *Building and Environment*, vol. 45, pp. 411–420, 2010.

[19] T. Van Renterghem, K. Attenborough, M. Maennel, J. Defrance, K. Horoshenkov, J. Kang, I. Bashir, S. Taherzadeh, B. Altreuther, A. Khan, Y. Smyrnova, and H. S. Yang, "Measured light vehicle noise reduction by hedges," *Appl. Acoust.*, vol. 78, pp. 19–27, 2014.

[20] K. B. Rasmussen, "Model experiments related to outdoor propagation over an earth berm," *J. Acoust. Soc. Am.*, vol. 96, pp. 3617–3620, 1994.

[21] T. Van Renterghem, D. Botteldooren, W. M. Cornelis, and D. Gabriels, "Reducing screen-induced refraction of noise barriers in wind by vegetative screens," *Acta Acustica*, vol. 88, pp. 231–238, 2002.

[22] G. Guillaume, B. Gauvreau, and P. L'Hermite, "Estimation expérimentale des propriétés acoustiques de surfaces végétalisées : influences de la variabilité spatiale et de la configuration de mesure," in *Congrès Français d'Acoustique*, 2014.

[23] J. Eaton and Z. Eckstein, "Cities and growth: theory and evidence from france and japan," *Regional Science and Urban Economics*, vol. 27, pp. 443–474, 1997.

[24] A. Lee and M. F. Slak, "Les paysages français changent entre 1992 et 2002 : artificialisation et fermeture des paysages aux dépens du mitage ou de la déprise des zones agricoles," tech. rep., ENITA de Bordeaux, Agreste cahiers, 2007.

[25] J. Bouillie, "Bilan patrimonial des forêts domaniales," tech. rep., ONF, 2006.

[26] "Directive 2002/49/EC of the European Parliament and of the Council of 25 June 2002 relating to the assessment and management of environmental noise," Official Journal of the European Communities, L 189/12, 2002.

[27] P. Delaitre, C. Lavandier, C. Cance, and J. Pruvost, "What is the Definition for the French Word calme in the European Directive Related to Quiet Areas? A Lexicographic Study from the 16th Century Until Today," *Acta Acustica*, vol. 98, pp. 734–740, 2012.

[28] European Environment Agency, "Good practice guide on quiet areas," tech. rep., EEA, 2014.

[29] C. K. Catchpole and P. J. B. Slater, *Bird Song: Biological Themes and Variations*. Cambridge University Press, 2008.

[30] J. R. Barber, K. R. Crooks, and K. M. Fristrup, "The cost of chronic noise exposure for terrestrial organisms," *Trends in ecology and evolution*, vol. 25, pp. 180–189, 2009.

[31] ISO 9613-2, "Attenuation of sound during propagation outdoors - part 2," in *Geneva : International Organization for Standardization*, 2006.

[32] Nord2000, "Nordic environmental noise prediction method," in *General Nordic Sound Propagation Model And Applications In Source-related Prediction Methods*, 2002.

[33] Harmonoise WP3, "Engineering method for road traffic and railway noise after validation and fine-tuning," in *Technical Report HAR32TR-040922-DGMR20*, 2005.

[34] A. Tarero, M. Martin, J. Gonzalez, M. Machimbarrena, and F. Jacobsen, "Sound propagation in forests: a comparison of experimental results and values predicted by the nord 2000 model," *Appl. Acoust.*, vol. 69, pp. 662–671, 2008.

[35] W. H. T. Huisman, *Sound propagation over vegetation-covered ground*. PhD thesis, Radboud Universiteit Nijmegen, 1990.

[36] W. H. T. Huisman, "Microclimate influence on sound propagation in vegetations," in *Internoise München, 453-456*, 1985.

[37] N. Barrière, *Etude théorique et expérimentale de la propagation du bruit de trafic en forêt*. PhD thesis, Centre scientifique et technique du bâtiment, 1999.

[38] M. White and M. Swearingen, "Sound propagation through a forest: a predictive model," tech. rep., US army corps of engineers., 2004.

[39] M. E. Swearingen and J. White, "Influence of scattering, atmospheric refraction, and ground effect on sound propagation through a pine forest," *J. Acoust. Soc. Am.*, vol. 122, pp. 113–119, 2007.

[40] A. Tunick, "Calculating the micrometeorological influences on the speed of sound through the atmosphere in forests," *J. Acoust. Soc. Am.*, vol. 114, pp. 1796–1806, 2003.

[41] E. Johansson, "The sound amplifying forest, with emphasis on sounds from wind turbines," Master's thesis, Chalmers University of Technology, 2010.

[42] D. Heimann, "Numerical simulation of wind and sound propagation through an idealised stand of trees," *Acta Acustica*, vol. 89, pp. 779–788, 2003.

[43] U. Kristiansen and K. Jezzine, "TLM propagation model for sound propagation above ground," in *Internoise*, 2000.

[44] Y. Kagawa, T. Hara, and T. Tsuji, "Discrete huygens' modelling simulation of sound wave propagation in velocity varying environments," *J. Sound Vib.*, vol. 246, pp. 419–439, 2001.

[45] J. Hofmann and K. Heutschi, "Simulation of outdoor sound propagation with a transmission line matrix method," *Appl. Acoust.*, vol. 68, pp. 158–172, 2007.

[46] G. Guillaume, P. Aumond, B. Gauvreau, and G. Dutilleux, "Application of the transmission line matrix method for outdoor sound propagation modelling part 1: Model presentation and evaluation," *Appl. Acoust.*, vol. 76, pp. 113–118, 2014.

[47] G. Guillaume, *Application de la méthode TLM à la modélisation de la propagation acoustique en milieu urbain*. PhD thesis, Université du Maine, 2009.

[48] P. Aumond, *Modélisation numérique pour l'acoustique environnementale : simulation de champs météorologiques et intégration dans un modèle de propagation*. PhD thesis, Université du Maine, 2011.

[49] K. Attenborough, K. M. Li, and K. Horoshenkov, *Predicting outdoor sound*. Taylor & Francis, 2007.

[50] R. Talaske, "The acoustic impedance of layered forest floor," Master's thesis, Pennsylvania State University, 1980.

[51] K. Attenborough, "Acoustical impedance models for outdoor ground surfaces," *J. Sound Vib.*, vol. 99(4), pp. 521–544, 1985.

[52] K. Attenborough, "Ground parameter information for propagation modeling," *J. Acoust. Soc. Am.*, vol. 92(1), pp. 418–427, 1992.

[53] M. Price, "Sound attenuation through trees: measurements and models," *J. Acoust. Soc. Am.*, vol. 84, pp. 1836 – 1844, 1988.

[54] K. Attenborough, I. Bashir, and S. Taherzadeh, "Outdoor ground impedance models," *J. Acoust. Soc. Am.*, vol. 129, pp. 2806–2819, 2011.

[55] D. K. Wilson, S. L. Collier, V. E. Ostashev, D. F. Aldrige, N. P. Symons, and D. H. Marlin, "Time-domain modeling of the acoustic impedance of porous surfaces," *Acta Acustica*, vol. 92, pp. 965–975, 2006.

[56] G. Heisler, O. McDaniel, and M. Dahl, "Measurements of normal-incidence impedance of six forest floors by the tube method," in *LRSP 2.2, New Orleans, LA USA*, 1984.

[57] T. F. W. Embleton, "Sound propagation in homogeneous deciduous and evergreen woods," *J. Acoust. Soc. Am.*, vol. 35, pp. 1119–1125, 1963.

[58] J. Kragh, "Road traffic noise attenuation by belts of trees and bushes," tech. rep., Danish acoustic laboratory, report 31, 1982.

[59] M. Martens, L.A.M. Van der Heijden, H. Walthaus, and W.J.J.M. Van Rems, "Classification of soils based on acoustic impedance, air flow resistivity, and other physical soil parameters," *J. Acoust. Soc. Am.*, vol. 78, pp. 970–980, 1985.

[60] G. Guillaume, J. Picaut, G. Dutilleux, and B. Gauvreau, "Time-domain impedance formulation for transmission line matrix modelling of outdoor sound propagation," *J. Sound Vib.*, vol. 330, pp. 6467–6481, 2011.

[61] M. Bruneau, *Manuel d'acoustique fondamentale*. Hermès, 1998.

[62] M. E. Swearingen and D. C. Swanson, "A numerical model for point source scattering from an impedance cylinder placed normal to an impedance plane," *Acta Acustica*, vol. 98, pp. 523–533, 2012.

[63] X. Di and K. E. Gilbert, "An exact Laplace transform formulation for a point source above a ground surface," *J. Acoust. Soc. Am.*, vol. 93(2), 1993.

[64] T. Li and M. Ueda, "Sound scattering of a spherical wave incident on a cylinder," *J. Acoust. Soc. Am.*, vol. 87, pp. 1871–1879, 1990.

[65] G. Reethof, L. D. Frank, and O. H. McDaniel, "Absorption of sound by tree bark," *USDA Service Research*, vol. NE-341, pp. 1–6, 1976.

[66] V. Twersky, "Multiple scattering of radiation by an arbitrary configuration of parallel cylinders," *J. Acoust. Soc. Am.*, vol. 24, pp. 42–46, 1952.

[67] V. Twersky, "On scattering of waves by random distributions. I. Free space scatterer formalism," *J. Math. Phys.*, vol. 3, pp. 700–715, 1962.

[68] C. M. Linton and P. A. Martin, "Multiple scattering by random configurations of circular cylinders: second-order corrections for the effective wavenumber," *J. Acoust. Soc. Am.*, vol. 117, pp. 3413–3423, 2005.

[69] D. Felbacq, G. Tayeb, and D. Maystre, "Scattering by random set of parallel cylinders," *J. Optical Soc. Am.*, vol. 11(9), pp. 2526–2538, 1994.

[70] R. Bullen and F. Fricke, "Sound propagation through vegetation," *J. Sound Vib.*, vol. 80, pp. 11–23, 1982.

[71] T. Embleton, "Scattering by an array of cylinders as a function of surface impedance," *J. Acoust. Soc. Am.*, vol. 40, pp. 667–670, 1966.

[72] D. Heimann, "Numerical simulation of wind and sound propagation through an idealised stand of trees," *Acta Acustica*, vol. 89, pp. 779–788, 2003.

[73] C. Lagarrigue, J. P. Groby, and V. Tournat, "Sustainable sonic crystal made of resonating bamboo rods," *J. Acoust. Soc. Am.*, vol. 133(1), pp. 247–254, 2013.

[74] O. Umnova, C. M. Linton, and K. Attenborough, "Multiple scattering by arrays of large cylinders," in *The 3rd International congress and exposition on noise control and engineering. Inter-noise*, 2004.

[75] R. Martinez-Sala, C. Rubio, L. M. Garcia-Raffi, J. V. Sanchez-Perez, E. A. Sanchez-Perez, and J. Llinares, "Control of noise by trees arranged like sonic crystals," *J. Sound Vib.*, vol. 291, pp. 100–106, 2006.

[76] T. Van Renterghem, D. Botteldooren, and K. Verheyen, "Road traffic noise shielding by vegetation belts of limited depth," *J. Sound Vib.*, vol. 331, pp. 2404–2425, 2012.

[77] S. Taherzadeh, I. Bashir, and K. Attenborough, "Aperiodicity effects on sound transmission through arrays of identical cylinders perpendicular to the ground," *J. Acoust. Soc. Am.*, vol. 132(4), p. Express letter, 2012.

[78] Y. Fan, B. Zhiyi, Z. Zhujun, and L. Jiani, "The investigation of noise attenuation by plants and the corresponding noise-reducing spectrum," *J. Env. Health*, vol. 72, pp. 8–15, 2010.

[79] M. Martens, "Foliage as a low-pass filter: experiments with model forests in an anechoic chamber," *J. Acoust. Soc. Am.*, vol. 67, pp. 66–72, 1980.

[80] H. S. Yang, J. Kang, C. Cheal, T. Van Renterghem, and D. Botteldooren, "Quantifying scattered sound energy from a single tree by means of reverberation time," *J. Acoust. Soc. Am.*, vol. 134, pp. 264–274, 2013.

[81] S. H. Burns, "The absorption of sound by pine trees," *J. Acoust. Soc. Am.*, vol. 65, pp. 658–661, 1979.

[82] O. Fégeant, "Wind-induced vegetation noise. Part I: a prediction model," *Acta Acustica*, vol. 85, pp. 228–240, 1999.

[83] K. Bolin, "Prediction method for wind-induced vegetation noise," *Acta Acustica*, vol. 95, pp. 607–619, 2009.

[84] W. H. T. Huisman and K. Attenborough, "Reverberation and attenuation in a pine forest," *J. Acoust. Soc. Am.*, vol. 90, pp. 2664–2677, 1991.

[85] M. Padgham, "Reverberation and frequency attenuation in forest - implications for acoustic communication in animals," *J. Acoust. Soc. Am.*, vol. 115, pp. 402–410, 2003.

[86] K. Marten and P. Marler, "Sound transmission and its significance for animal vocalization," *Behav. Ecol. Sociobiol.*, vol. 2, pp. 271–290, 1977.

[87] M. E. Swearingen, M. J. White, P. J. Guertin, D. G. Albert, and A. Tunick, "Influence of a forest edge on acoustical propagation: experimental results," *J. Acoust. Soc. Am.*, vol. 133, pp. 2566–2575, 2013.

[88] E. Morton, "Ecological sources of selection on avian sounds," *Amer. Natur.*, vol. 108, pp. 17–34, 1975.

[89] T. Watanabe and S. Yamada, "Sound attenuation through absorption by vegetation," *J. Acoust. Soc. Jpn.*, vol. 17, pp. 175–182, 1996.

[90] F. Fricke, "Sound attenuation in forests," *J. Sound Vib.*, vol. 92, pp. 149–158, 1984.

[91] T. F. W. Embleton, "Tutorial on sound propagation outdoors," *J. Acoust. Soc. Am.*, vol. 100, pp. 31–48, 1996.

[92] S. Dupont and Y. Brunet, "Influence of foliar density profile on canopy flow: a large-eddy simulation study," *Agricultural and Forest Meteorology*, vol. 148, pp. 976–990, 2008.

[93] V. Masson and Y. Seity, "Including atmospheric layers in vegetation and urban offline surface schemes," *J. Appl. Meteor. Climatol.*, vol. 48(7), pp. 1377–1397, 2009.

[94] S. Y. Hui and A. Crockford, "Wind profiles and forests," Master's thesis, Technical University of Denmark, 2007.

[95] S. Dupont and Y. Brunet, "Coherent structures in canopy edge flow: a large-eddy simulation study," *J. Fluid Mech.*, vol. 630, pp. 93–128, 2009.

[96] J. B. Fisher, T. A. DeBiase, Y. Qi, M. Xu, and A. H. Goldstein, "Evapotranspiration models compared on a Sierra Nevada forest ecosystem," *J. Env. Mod. Soft.*, vol. 20, pp. 783–796, 2005.

[97] S. Dupont and E. G. Patton, "Influence of stability and seasonal canopy changes on micrometeorology within and above an orchard canopy: The chats experiment," *Agricultural and Forest Meteorology*, vol. 157, pp. 11–29, 2012.

[98] C. F. Eyring, "Jungle acoustics," *J. Acoust. Soc. Am.*, vol. 18, pp. 257–270, 1946.

[99] E. M. Salomons, *Computational atmospheric acoustics*. Kluwer academic publishers, 2001.

[100] M. E. Swearingen and D. C. Swanson, "A numerical model for point source scattering from an impedance cylinder placed normal to an impedance plane," *Acta Acustica*, vol. 98, pp. 523–533, 2012.

[101] A. Tunick and M. E. Swearingen, "Numerical model to calculate microphysical influences on sound wave propagation in forests," *Appl. Acoust.*, vol. 70, pp. 857–867, 2009.

[102] Y. Kagawa, T. Tsuchiya, B. Fuji, and K. Fujioka, "Discrete huygen's model approach to sound wave propagation," *J. Sound Vib.*, vol. 218, pp. 419–444, 1998.

[103] P. B. Johns and R. L. Beurle, "Numerical solution of 2-dimensional scattering problems using a transmission-line matrix," *Proc. IEE*, vol. 118, pp. 1203–1208, 1971.

[104] P. B. Johns, "Application of the transmission-line matrix method to homogeneous waveguides of arbitrary cross-section," *Proc. IEE*, vol. 119, pp. 1086–1091, 1972.

[105] P. B. Johns, "On the relationship between TLM and finite-difference methods for maxwell's equations," *IEEE Transactions on Microwave Theory and Techniques*, vol. 35, pp. 60–61, 1987.

[106] P. B. Johns, "A symmetrical condensed node for the TLM method," *IEEE Transactions on Microwave Theory and Techniques*, vol. 35, pp. 370–377, 1987.

[107] A. Saleh and P. Blanchfield, "Analysis of acoustic radiation patterns of array transducers using the tlm method," *Int. J. Numer. Model.*, vol. 3, pp. 39–56, 1990.

[108] S. El-Masri, X. Pelorson, P. Saguet, and P. Badin, "Vocal tract acoustics using the transmission line matrix (TLM) method," *International conférence on speech and language processing (ICSLP)*, vol. 2, pp. 953–956, 1996.

[109] R.C. Booton, *Computational Methods for Electromagnetics and Microwaves*. Wiley, 1992, pp. 59-73.

[110] D. de Cogan, W. J. O'Connor, and S. Pulko, *Transmission Line Matrix in Computational Mechanics*. Taylor & Francis, 2006.

[111] J. P. Bérenger, "A perfectly matched layer for the absorption of electromagnetic waves," *J. Comp. Physics*, vol. 114, pp. 185–200, 1994.

[112] P. Saguet, *Analyse des milieux guidés - la méthode MTLM (Guided medium analysis: MTLM method)*. PhD thesis, Thèse d'État, 1985.

[113] G. Guillaume and J. Picaut, "A simple absorbing layer implementation for the transmission line matrix modeling," *J. Sound Vib.*, vol. 332, pp. 4560–4571, 2013.

[114] R. Higdon, "Absorbing boundary conditions for difference approximations to the multi-dimensional wave equation," *Mathematics of computation*, vol. 47, pp. 437–459, 1986.

[115] J. Schneider and O. Ramahi, "The complementary operators method applied to acoustic finite-difference time-domain simulations," *J. Acoust. Soc. Am.*, vol. 104, pp. 686–693, 1998.

[116] J. A. Porti and J. A. Morente, "TLM methods and acoustics," *Int. J. Numer. Model.*, vol. 14, pp. 171–183, 2001.

[117] X. Yuan, D. Borup, W. Wiskin, M. Berggren, R. Eidens, and S. A. Johnson, "Formulation and validation of Berenger's PML absorbing boundary for the FDTD simulation of acoustic scattering," *IEEE. T. Ultrason. Ferr. Freq. Cont.*, vol. 44, pp. 816–822, 1997.

[118] S. G. Johnson, "Notes on perfectly matched layers (PMLs)." Notes for the courses 18.369 and 18.336 at MIT, 2008.

[119] W. Chew and W. Weedon, "A 3D perfectly matched medium from modified Maxwell's equations with stretched coordinates," *Microwave and optical technology letters*, vol. 7, pp. 599–604, 1994.

[120] P. Morse and H. Feshbach, *Methods of Theoretical Physics*. New-York: McGraw-Hill book compagny inc., 1953.

[121] Y. L. Sheu and P. C. Li, "Simulations fo photoacoustic wave propagation using a finite-difference time-domain method with brenger's perfectly matched layers," *J. Acoust. Soc. Am.*, vol. 124, pp. 3471–3480, 2008.

[122] G. Dutilleux, J. Defrance, D. Ecotière, B. Gauvreau, M. Bérengier, F. Besnard, and E. Le Duc, "NMPB-Routes-2008: The Revision of the French Method for Road Traffic Noise Prediction," *Acta Acustica*, vol. 96, pp. 452–462, 2010.

[123] J. Faran, "Sound scattering by solid cylinders and spheres," *J. Acoust. Soc. Am.*, vol. 23, pp. 405–418, 1951.

[124] P. Morris, "The scattering of sound from a spatially distributed axisymmetric cylindrical source by a circular cylinder," *J. Acoust. Soc. Am.*, vol. 97, pp. 2651–2656, 1995.

[125] J. G. Tolan and J. B. Schneider, "Locally conformal method for acoustic finite-difference time-domain modeling of rigid surfaces," *J. Acoust. Soc. Am.*, vol. 114, pp. 2575–2581, 2003.

[126] S. Wang, "Finite-difference time-domain approach to underwater acoustic scattering problems," *J. Acoust. Soc. Am.*, vol. 99(4), pp. 1924–1931, 1996.

[127] Y. Miki, "Acoustical properties of fibrous absorbent materials - Modification of Delany-Bazley models," *J. Acoust. Soc. Jpn.*, vol. 19-24, p. 11, 1990.

[128] V. Twersky, "Multiple scattering of radiation by an arbitrary configuration of parallel cylinders," *J. Acoust. Soc. Am.*, vol. 24, pp. 42–46, 1952.

[129] F. Goreaud, *Apport de l'analyse de la structure spatiale en forêt tempérée à l'étude et à la modélisation des peuplements complexes.* PhD thesis, ENGREF, 2000.

[130] B. Ripley, "The second order analysis of stationary point process," *Journal of Applied Probability*, vol. 13, pp. 255–266, 1976.

[131] J. Besag, "Contribution to the discussion of Dr Ripley's paper," *Journal of the Royal Satistical Society*, vol. 39, pp. 193–195, 1977.

[132] W. T. Chu, "Comparison of reverberation measurements using schroeder's impulse method and decay-curve averagingm method," *J. Acoust. Soc. Am.*, vol. 63, pp. 1444–1450, 1978.

[133] T. Miyashita, "Sonic crystals and sonic wave-guides," *Measurement Science and Technology*, vol. 16, p. 47, 2005.

[134] H. M. Hess, K. Attenborough, and N. W. Heap, "Ground characterization by short-range propagation measurements," *J. Acoust. Soc. Am.*, vol. 87, pp. 1975–1986, 1990.

Modeling of sound propagation in forests using the transmission line matrix method

Study of multiple scattering and ground effects related to forests

Pierre Chobeau

Doctoral thesis in Acoustics,

Ifsttar/LAE, France - Université du Maine, Le Mans, France

The prediction of sound propagation in presence of forest remains a major challenge for the outdoor sound propagation community. The investigation of forest as sound propagation medium is motivated by the propensity of a forest to mitigate noise, the protection of existing "green" quite area (Environmental Noise Directive 2002/49/EC) and the preservation of biodiversity. Absorption from forest ground at low frequencies, multiple scattering caused by tree trunks and the modification of temperature and wind gradients are the three main phenomena that directly impact sound propagation in significant forested areas. Reference numerical models such as the Transmission Line Matrix (TLM) method can be developed in order to accurately predict each acoustical phenomenon that takes place inside forest. This time domain method has already been used to model long range sound propagation and is well suited for the prediction of transient phenomena.

The first need for the TLM method is an efficient theory-based absorbing layer formulation that enables the truncation of the numerical domain. This aims at lowering the computational cost of the method. The two proposed absorbing layer formulations are based on the approximation of the perfectly matched layer theory. The most efficient proposed formulation is shown to be equivalent to wave propagation in a lossy media, which, in the TLM method formulation, is introduced using an additional dissipation term. In comparison to the existing empirical one-way approach, the proposed absorbing matched layer, after optimization, presents lower reflection errors for large angle span.

The ability of the TLM method for the simulation of scattering is studied comparing the numerical results to both analytical solutions and measurements on scale models. It is shown that both single and multiple scattering predicted with the TLM method are in good agreement with the theory. Moreover, the measurements of scattering above either reflecting or impedance grounds show that the TLM method predictions are in correct agreement with the measured data.

Lastly, the attenuation of acoustic levels by a simplified forest is numerically studied using several arrangements of cylinders placed normal to either reflecting or absorbing ground. It is observed that randomly spaced arrangements are more inclined to attenuate acoustic waves than periodic arrangements. Moreover, the sensitivity to the density, the length of the array and the ground absorption is tested. The main trend shows that the density and the distribution are two important parameters for the attenuation. In future work, it can be interesting to look at the sensitivity of each parameter. This study could then be used to relate the morphology (*i.e.* distribution, density, length) of a forest to the acoustical properties of the forest.